Functionalization of graphene-based gas sensors with nanoparticles for ethylene sensing

Ruben Vos (5268966)

Delft University of Technology

TU Delft

Abstract

Ethylene (C2H4) is an important volatile organic compound (VOC) with applications in agriculture, environmental monitoring, and industrial processes. In this work, graphene was investigated as a material for gas sensing applications. To improve the selectivity of graphene toward ethylene, the graphene surface was functionalized using nanoparticles. Graphene-based sensor devices were successfully fabricated and subsequently characterized using Raman spectroscopy, Scanning Electron Microscopy (SEM), and electrical measurements. The characterization results confirmed the successful fabrication of graphene devices and demonstrated that the nanoparticle functionalization process caused limited damage to the graphene. Gas sensing measurements further showed that both pristine and nanoparticle-functionalized graphene devices were capable of detecting ethylene gas. However, within the conditions investigated in this work, the selected nanoparticle functionalizations did not result in an improvement in ethylene sensitivity compared to non-functionalized graphene. Future work could focus on investigating alternative nanoparticle material or operating the sensors at elevated temperatures.

Acknowledgements

First, I would like to sincerely thank my supervisors, Mudassir and Sten, for their guidance and support throughout this project. I am very grateful for the answers to my countless questions.

I would also like to thank everyone from the team Nano group for their help with the trainings of all the equipment and their advice, as well as the EKL staff for their technical support and assistance in the cleanroom.

A special thanks goes to my office mates at the end of the hallway for making the long thesis days much more enjoyable. The interesting conversations and shared lunches always helped restore energy and motivation. I know that one day we will put a stroopwafel into the lithography machine.

I am also very grateful to my friends and roommates for bringing joy and balance outside of thesis work and for always being there during both stressful and enjoyable moments.

To my family, thank you for your continuous encouragement and support throughout my studies. Being in the study shed fully taken care of gave me some much needed energy.

And of course, my deepest thanks and love go to Fenne, for the happiness, support, and positivity you bring in my life.

List of Figures

List of Tables

Contents

1 Introduction

Ethylene (C2H4) is a simple hydrocarbon gas that plays an important role in both natural and industrial environments. In nature, ethylene functions as a plant hormone that regulates various physiological processes, including fruit ripening and plant growth [1]. Because of these properties, monitoring ethylene concentrations is highly relevant in agriculture, food storage, and environmental monitoring [2].

Despite its importance, reliable ethylene sensing remains difficult [3]. Ethylene belongs to the group of volatile organic compounds (VOCs), which are characterized by their high volatility and chemical reactivity. VOCs are commonly present in mixtures of their group, making selective detection difficult as they interfere with sensing [4]. Therefore, the development of sensitive and selective gas sensors for VOC detection is an important research topic.

There are currently methods of selectively sensing ethylene such as using gas chromatography and Raman spectroscopy. Although these techniques can provide accurate measurements, they require bulky and expensive instrumentation in addition to their high power consumption [3]. These limitations result in those methods being unpractical for fruit and plant monitoring.

In recent years, graphene-based gas sensors have attracted considerable attention because of graphene's exceptional electrical, mechanical, and chemical properties [5]. Graphene possesses a large surface-to-volume ratio and high carrier mobility, which make it highly sensitive to adsorbed gas molecules [6]. These characteristics provide significant potential for the development of low-power and highly sensitive gas sensors operating at room temperature.

1.1. Motivation and Problem Formulation

Graphene-based gas sensors are considered promising candidates for next-generation sensing technologies. However, one of the main limitations of pristine graphene is its poor selectivity [7]. Since many gas molecules interact with graphene similarly, distinguishing between different gases in a complex environment remains difficult.

One approach to improve the sensing performance of graphene is functionalization with nanoparticles [8]. Nanoparticles can modify the surface properties of graphene, introduce catalytic effects, and enhance charge transfer between gas molecules and the sensing layer [9]. As a result, both the sensitivity and selectivity of graphene sensors can be significantly improved [8]. However, the choice of suitable nanoparticles and their influence on ethylene sensing are not yet fully understood.

Another challenge arises from the typically low concentration of ethylene in practical applications. Ethylene is often present in the parts-per-million (ppm) or even parts-per-billion (ppb) range, requiring sensors with extremely high sensitivity and low detection limits [2]. Developing a graphene-based sensor capable of selectively detecting ethylene at such low concentrations therefore remains an important scientific and technological challenge. This forms the central research question of this work. Can functionalization of a graphene gas sensor with nanoparticles improve selectivity towards ethylene?

1.2. Objectives

To determine if the functionalization of graphene with nanoparticles can improve selectivity the following goals are presented:

- Search for suitable nanoparticles for the functionalization of graphene gas sensors.
- Fabricate and functionalize a graphene gas sensor.
- Characterize the graphene gas sensor.
- Determine the increase in selectivity of the functionalization.

1.3. Outline

This thesis is divided into four main parts. First, Chapter 2 introduces the theoretical background relevant to graphene, nanoparticles, and gas sensing mechanisms. Second, Chapter 3 describes the experimental methods and fabrication procedures used in this work. Third, Chapter 4 presents and discusses the material characterization of the graphene and nanoparticle-functionalized samples. Finally, Chapter 5 presents and analyses the gas sensing measurements, followed by a discussion of the results and the overall conclusions in Chapter 6.

2

Literature Study

In this chapter, the background information relevant to this work is presented and discussed. It begins with an overview of the properties and physics of graphene, including its various synthesis methods. Next, gas sensors are introduced followed by how their performance are measured. This is followed by a discussion of the sensing mechanisms of graphene-based gas sensors, with particular emphasis on how nanoparticles (np's) and their properties can enhance performance. Finally, ethylene is examined and previous work on its detection is reviewed.

2.1. Graphene

Graphene is a two-dimensional material consisting only of carbon atoms arranged in a hexagonal lattice as shown in Figure 2.1 [10]. Each carbon atom is bonded to three neighbouring carbon atoms within the same plane. These bonds are formed through the overlap of three sp^2 hybridized orbitals, creating covalent σ-bonds that form the rigid honeycomb lattice [11]. The remaining p-orbital forms π-bonds that extend above and below the graphene plane, producing a delocalized electron system responsible for graphene's excellent electrical conductivity [11].

When multiple graphene layers are stacked, they are held together by weak van der Waals forces, forming materials such as graphite [10]. When graphene is only 1 layer it is called "Single Layer Graphene"(SLG) at fewer than 10 layers it is "Few Layer Graphene"(FLG). At more than 10 layers it is called "Multi Layer Graphene"(MLG) [13].

Graphene's electronic structure features a zero band gap [11], making it behave as a semimetal. It also exhibits very high electron mobility, reaching values up to 15000 $\frac{cm^2}{V \cdot s}$ at room temperature which results in it having a low intrinsic noise [5]. Because graphene is a two-dimensional material, it has an extremely high surface-to-volume ratio, meaning all atoms are exposed at the surface [6]. Additionally, graphene is mechanically and thermally very stable [14].

2.1.1. Synthesis methods

Several methods have been developed to produce graphene, each with its own advantages and limitations. The most commonly used approaches include mechanical exfoliation, liquid phase exfoliation, and chemical vapor deposition (CVD). These methods differ in terms of graphene quality and scalability [10, 11].

Mechanical Exfoliation

Mechanical exfoliation was the first method used to isolate graphene [5]. In this technique, adhesive tape is used to peel layers from bulk graphite. By repeatedly peeling the material, the graphite flakes become progressively thinner until single-layer graphene can be obtained. The resulting graphene flakes are then transferred onto a substrate for characterization or device fabrication.

This method produces graphene with very high crystalline quality and extremely low defect density compared to most other fabrication techniques [10]. As a result, mechanically exfoliated graphene is

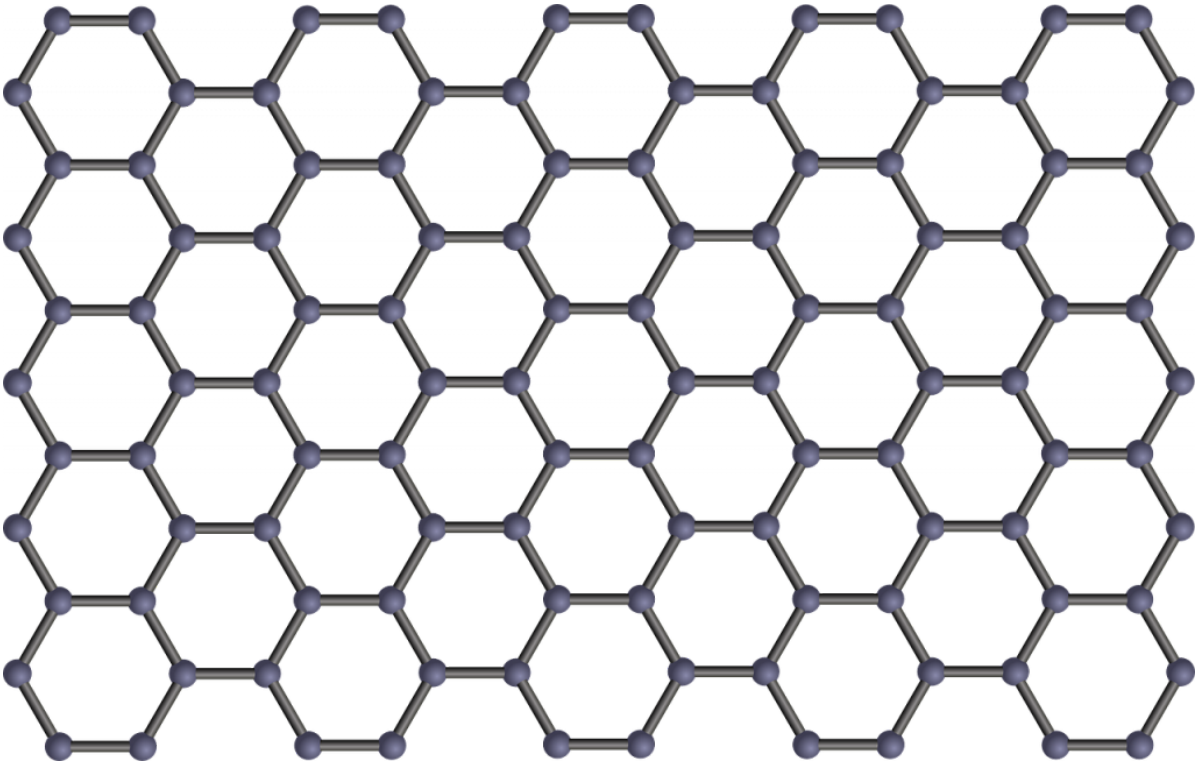

Figure 2.1: Graphene Lattice[12]

frequently used in academics. However, the major drawback of this method is that it is not scalable, since the process produces only small flakes and cannot be easily controlled for large-scale production [15]. Therefore, mechanical exfoliation is not suitable for commercial manufacturing.

Liquid Phase Exfoliation

Liquid phase exfoliation (LPE) is a scalable method for producing graphene by dispersing graphite in a liquid solvent. In this technique, graphite is mixed with a solvent whose surface energy closely matches that of graphene, which helps stabilize exfoliated graphene layers in suspension [16]. Mechanical energy, typically applied through ultrasonification or shear mixing, separates the graphite into thinner flakes.

The number of graphene layers obtained depends on processing parameters and post-treatment steps such as centrifugation [16]. Although LPE enables large-scale production of graphene dispersions, the resulting flakes are usually smaller and contain more defects compared to mechanically exfoliated graphene [17].

Chemical Vapor Deposition

Chemical vapor deposition (CVD) can be used for producing large-area graphene films. In this method, a hydrocarbon gas such as methane is decomposed at high temperature in the presence of a catalytic metal substrate, typically copper or nickel. Carbon atoms released from the gas then nucleate and grow into a graphene layer on the metal surface [18].

CVD allows the synthesis of continuous graphene films over large areas, making it suitable for industrial applications and electronic device fabrication. However, graphene grown on metal substrates often needs to be transferred onto an insulating substrate before device integration, which can introduce defects or contamination [18].

Transfer-free approaches have also been explored. For example, graphene can be grown on molybdenum substrates where metal electrodes are attached before the molybdenum is chemically etched away, leaving a functional device structure if the underlying layer is insulating [19]. A schematic overview can be seen in Figure 2.2.

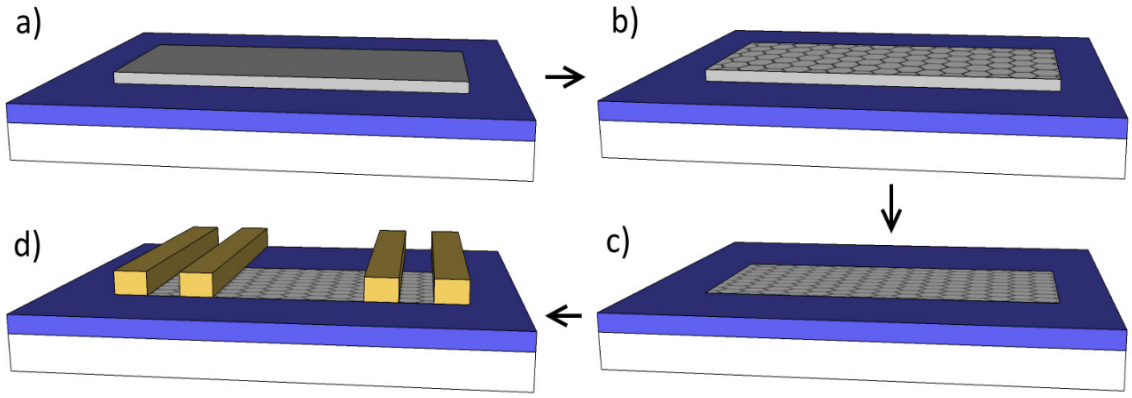

Figure 2.2: Schematic overview of the fabrication process: a) deposition and patterning of the Mo layer on Si substrate with SiO 2; b) CVD deposition of graphene on Mo; c) wet etching of the Mo layer; d) deposition of Cr/Au electrodes using a lift-off process[19]

2.2. Gas Sensors

A gas sensor is used to transform a concentration of a gas (or gasses) into a response that can be measured. For an effective gas sensor it is important that the sensor is only sensitive to the target gas, which is defined as its selectivity. It is also necessary for the gas sensor to be sensitive enough that it can detect a target gas at low concentrations. In addition, it is needed for the gas sensor to be able to measure a change in concentrations quickly. Finally, the response of a gas sensor must be stable and repeatable.

Multiple gas sensors can also be used in an array and by combining their data it is possible to detect a target gas when interfering gasses are present. With this method it is possible to use gas sensors with poor selectivity if the sensors in the array have sufficient differing selectivities.

2.2.1. Graphene Gas Sensors

Graphene is considered a promising material for gas sensing applications due to its two-dimensional structure. Because graphene consists of a single atomic layer, it has an extremely high surface-to-volume ratio, meaning all atoms are exposed to the environment. As a result, interactions occurring at the surface can significantly influence the electrical properties of the material [6].

Additionally, due to its high electron mobility graphene exhibits relatively low Johnson noise, 1/f noise and high carrier mobility, allowing small changes in electrical resistance to be detected with high sensitivity [11]. The π-electron system extending above and below the graphene lattice enables strong interactions with adsorbed gas molecules. When gas molecules attach to the graphene surface by Van der Waal forces (physisorbtion), they can either donate electrons to the graphene or withdraw electrons from it. These gases are therefore commonly classified as electron-donating (reducing) or electron-accepting (oxidizing) gasses [6, 20]. Such charge transfer processes alter the carrier concentration in graphene, which can be detected as a measurable change in resistance.

2.2.2. Performance metrics

For this study the metrics that are used to define the performance of the devices are defined as followed.

Response

Response is defined as normalized difference between the resistance before gas turns on and when the gas is turned off. The following equation describes it accurately.

$$Response = \frac{R_{Response} - R_{Baseline}}{R_{Baseline}} = \frac{\Delta R}{R_0} \tag{2.1}$$

Where $R_{Respone}$ is the resistance after the gas has been turned on for some time and $R_{Baselines}$ is the resistance in steady state when no reacting gas is present. The different resistances are visualized in Figure 2.3.

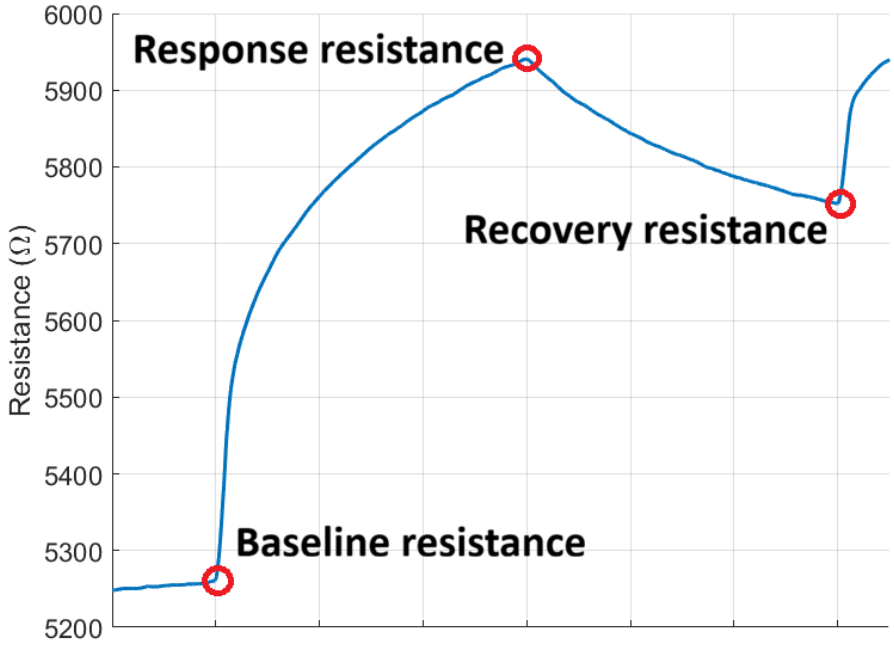

Figure 2.3: Reference response

The strength of the response is typically decreased with more cycles, since the device typically does not recover fully or very slowly when no additional heat or UV is applied. To compare responses between devices and measurements the first response is taken as a primary response since if the device would recover completely that will be the response.

Recovery
The recovery starts after the sensor had a response from a gas and the sensed gas is no longer flown onto the sample. The resistance will go towards the baseline resistance again. However, the recovery of the sensor might not reach the baseline as some of the gas might stick to the sensor or there is no oxygen to replenish the atoms lost [21]. The recovery is then defined as the percentage of how far the resistance is returned to the baseline as can be seen in the following equation.

$$Recovery = \frac{R_{Response} - R_{Recovery}}{R_{Response} - R_{Baseline}} \tag{2.2}$$

$R_{Recovery}$ is the resistance after some time the gas has been turned off and is visualized in Figure 2.3.

Sensitivity
Sensitivity is defined as the strength of the response compared to the concentration of the gas.

$$Sensitivity_{gas} = S_{Gas} = \frac{Response_{gas}}{Concentration_{gas}} \tag{2.3}$$

Selectivity
Selectivity is the difference sensitivity relative to the reaction of other gasses. Increasing selectivity to one gas means that it will give a stronger response tot that one gas or a weaker response to other gasses. This is defined in the following equation.

$$Selectivity_{Gas1-Gas2} = \frac{Sensetivity_{Gas1}}{Sensetivity_{Gas2}} \tag{2.4}$$

Where Gas1 is the sensed gas and Gas2 the interfering gas.

Response and recovery time
The response time is defined as the time for the signal to reach 90% of the response after the gas is introduced.

The recovery time is defined as the time for the signal to reach 90% of the recovery after the gas is removed.

Limit of detection
Limit of detection (LOD) is the lowest amount of concentration that the sensor is able to measure. This is dependent on both the sensitivity of the sensor and how much noise it has. An estimation of the LOD is the following formula [7].

$$LOD_{Gas} = \frac{3\sigma}{S_{Gas}} \tag{2.5}$$

Where σ is the standard deviation of the changes in resistance while in a steady state and S_{Gas} is the sensitivity of the sensor to a gas.

2.3. Sensing Mechanism

Graphene is considered a zero band-gap semimetal, however when exposed to ambient conditions it typically behaves as a weak *p-type* semiconductor. This is due to the adsorption of oxygen and water molecules from the surrounding environment, which act as electron acceptors and withdraw electrons from the graphene [6, 22]. As a result, the Fermi level shifts below the Dirac point, leaving holes as the dominant charge carriers.

The sensing mechanism of graphene-based gas sensors relies on the change in electrical resistance caused by charge transfer between adsorbed molecules and the graphene sheet. When gas molecules adsorb onto the graphene surface, they can either donate electrons to the graphene or withdraw electrons from it. Electron-donating gases reduce the hole concentration in p-type graphene, thereby increasing the resistance, whereas electron-withdrawing gases increase the hole concentration and thus decrease the resistance [7]. By continuously monitoring the resistance of the graphene layer, information about gas in the environment can be obtained.

In many graphene gas sensors, oxygen plays a crucial role in the sensing process. Oxygen molecules can adsorb onto the graphene surface and take electrons from the graphene, forming negatively charged oxygen species such as O_2^- or O^- [23]. These oxygen ions modify the local charge carrier concentration and contribute to the baseline resistance of the device. When a target gas is introduced, they can react with these oxygen species in redox reactions. For reducing gases, such as NH_3, the gas molecules react with the oxygen ions and remove them from the surface, giving electrons back into the graphene. This reduces the hole concentration and increases the resistance of the graphene. In contrast, oxidizing gases such as NO_2 can directly take electrons from graphene, leading to an increase in hole concentration and a decrease in resistance.

2.4. Nanoparticles

Nanoparticles (np's) are as their name suggest particles with a size in the nm, ranging from around 1 to 100 nanometers. Because of their size, the ratio of surface area to volume is large compared to their macroscopic counterparts. This large surface area makes them good candidates for all kinds of catalytic activity. In gas sensing they are used to both increase the sensitivity and selectivity to different gasses.

2.4.1. Synthesis methods

There are multiple methods to create nanoparticles such as Spark ablation which is used in this work. Thermal evaporation, and chemical methods.

In spark ablation two electrodes are placed at a close distance to each other and by putting a voltage on it a spark can be generated between them. When sparking the electrodes lose some material that form nanoparticles. One main advantage of this method is its flexibility with the nanoparticle material, since a different material only requires changing the electrodes and adjusting the spark parameters.

Moreover, spark ablation has a relatively low environmental impact, as it does not rely on chemicals. In addition, the generated nanoparticles can be transported by a carrier gas directly to a deposition or printing system, allowing for deposition on areas of a substrate. This reduces the need for a lithography step. However, a drawback currently is the production rate of nano-particles currently is not enough to be commercially viable [24]. Further discussion on spark ablation can be found in Section 3.2.

Thermal ablation uses a bulk material that is vaporized at high temperatures and subsequently condensed into nanoscale particles [25]. By having the material being exposed to an intense heat source such as a laser or electron beam it generates a vapor plume of atoms, where cooling induces nucleation and particle growth [26]. Parameters such as temperature, pressure, and surrounding medium strongly influence particle size and morphology [25]. Just like with spark ablation another material is easily used, however most materials require heating up above 700 ℃ to thermally ablate making them cost a lot of energy [24].

There are multiple methods of making nanoparticles using chemical methods. As an example in the work of Jin et al. [27] Pd nanoparticles of few nanometers in diameter where directly synthesized unto the substrate. This was done putting the target substrate into a solution of palladium chloride and then adding drops of sodium borohydride until the solution becomes black because of the Pd^{2+} ion being reduced to its metal form and forming nanoparticles. The main advantage of chemical synthesis methods is the control over particle size and composition, allowing for the production of nanoparticles to specific requirements. However, these methods also have notable drawbacks. First, each type of nanoparticle typically requires a dedicated synthesis recipe, making the approach relatively inflexible, particularly in exploratory studies that rely on trial-and-error. Second, nanoparticles are formed in a solution that often contains surfactants, which leads to surface contamination. To access the nanoparticle surface a cleaning step is needed to remove these residues [24]. Due to this lack of flexibility and the presence of surface contamination, chemical synthesis methods are impractical for this work.

2.4.2. Nanoparticle Functionalization

Pristine graphene gas sensors can be limited by weak adsorption energies and poor selectivity for specific gas molecules. Meaning many gasses can be weakly bound to it. To overcome these limitations, graphene can be functionalized with metal or metal-oxide nanoparticles. This functionalization can enhance the sensitivity, selectivity, and response speed of graphene-based gas sensors [7, 23]. The effect of functionalization can be split into two categories, chemical and electronic.

In chemical functionalization nanoparticles deposited on the graphene surface act as catalytic active sites that promote the adsorption and dissociation of gas molecules. Compared to pristine graphene, these nanoparticles provide a higher binding affinity for many gas species, which increases the probability of gas adsorption and thereby the strength of the response. Nano-particles can also facilitate the adsorption of oxygen molecules, thereby increasing the density of reactive oxygen species on the surface [9].

The other effect of nanoparticle functionalization is the electronic interaction between the nanoparticles and the graphene layer. When metal nanoparticles are deposited onto graphene, charge transfer occurs due to the different work functions between the two materials. This charge transfer locally modifies the carrier concentration in graphene and can form potential barriers at the nanoparticle graphene interface [28]. These local junctions amplify the resistance changes that occur when gas molecules interact with the nanoparticles, thereby improving the sensor signal.

Different types of nanoparticles can be used depending on the target gas species. Noble metal nanoparticles such as gold (Au), platinum (Pt), and palladium (Pd) are commonly used because of their strong catalytic activity and chemical stability. For example gold is known to work well for nitrogen dioxide (NO2) [8].

Metal oxide nanoparticles such as tin oxide (SnO2) can also be used for graphene functionalization. The metal oxide nanoparticles can provide strong gas adsorption and surface reactions, while the graphene layer serves as a highly conductive channel that efficiently transduces the resulting charge transfer into an electrical signal [9].

The size and amount of nanoparticles strongly influence the sensing performance. In the work of Lee et al. [29] it was shown that the area coverage of the nano-particles has an optimum point. More or

less nanoparticles can result in significantly less sensitivity. In the work of Abideen et al. [30] a model was proposed to determine the total contribution of the nanoparticle to the gas sensors sensitivity using both the electronic and chemical effects. From this model the following conclusion were made. First the optimization of the area coverage of np's is required to have the sensor show the best sensing performance. Second, by decreasing the size of the np's the area coverage required to obtain the maximum sensitivity must increase. Finally, for larger sized np's, the width of the optimum area coverage becomes narrower compared to the case of smaller-sized np's. This suggests that more fine-tuning for the amount of np's is necessary when larger-sized np's are functionalized.

2.4.3. Ethylene

Ethylene (C_2H_4) is a small unsaturated hydrocarbon that acts as an important plant hormone. It plays a crucial role in regulating plant growth, fruit ripening, senescence, and stress responses. Many fruits such as bananas, tomatoes, and mangos produce ethylene during the ripening process, which in turn accelerates further ripening [1]. Because of this autocatalytic behaviour, monitoring ethylene concentration is important in agriculture, food storage, and transportation to control the ripening process and reduce post-harvest losses.

Ethylene can react with oxygen to produce acetaldehyde using the following reaction as can be seen in Figure 2.4. Since the reaction requires oxygen atoms, a gas sensor with oxygen on its surface will have it removed which induces a response. The reaction temperature with palladium chlorine as catalyst can be as low as 110°C [31]. This is the main method of producing acetaldehyde in industry today. However, the chlorine is likely unusable in the case for a graphene gas sensor as it would stick to the graphene at the defects sites which are also used for to bind to the target gas decreasing sensitivity [32]. In addition, chlorine can be corrosive in humid environments which is the case in gas sensing.

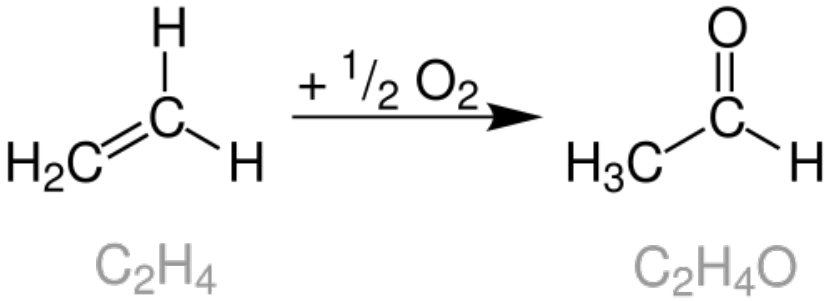

Figure 2.4: Wacker oxidation of ethylene to acetaldehyde

This is not the only way ethylene can react with oxygen, as it can also undergo complete or partial oxidation. In complete oxidation, ethylene is converted into carbon dioxide and water, while in partial oxidation it can form carbon monoxide and water [31]. In addition to oxidation reactions, ethylene can participate in other reaction pathways, leading to the formation of gasses such as ethane, acetylene, and propene [33].

Ethylene Gas Sensing

Ethylene consist of a carbon–carbon double bond which makes it sensitive to oxidation of the bond. It has a non-polar nature and relatively low chemical reactivity compared to more oxidizing gases such as NO_2, making detecting ethylene at low concentrations challenging. In many practical applications, ethylene concentrations will be needed to be detected in the range of a few parts-per-billion (ppb) to parts-per-million (ppm) [2]. This requirement makes highly sensitive gas sensing technologies necessary.

Due to ethylene being prone to oxidizing to acetaldehyde, the oxygen species on graphene can be used to detect it. When it takes an oxygen away from the graphene charge transfer occurs and the change in resistance is measurable. Since it is known that Palladium can act as a catalyst for the Wacker oxidation [31] it is theorized that it would be a good candidate for functionalization of a graphene gas sensor.

2.5. Current works

There have been many ethylene gas sensors that have currently been made, and the methods include gas chromatography, Infrared, Raman spectroscopy and metal oxides.

Gas chromatography is a technique to identify different gas molecules. They can be separated and identified via built-in gas chromatography columns due to the different specific retention times of each gas compound. A major advantage of gas chromatography is its high selectivity and accuracy, allowing reliable identification and quantification of complex gas mixtures. However, it typically requires physically large instruments, and relatively long analysis times, making it less suitable for real-time or portable sensing applications [3].

The infrared method is another widely used technique for gas detection by analysing the vibrational or rotational spectra of gas molecules. Gas molecules can absorb the light radiation and generate a band of signature absorption lines centred around a specific wavelength. The unique absorption peaks and corresponding absorption intensity can be used for the measurement of gas molecules. IR spectroscopy offers quick, non-destructive measurements and is well suited for continuous monitoring. Additionally, it can be implemented in compact sensor systems. However, its main limitation is its weak selectivity due to interference from overlapping absorption bands, especially in complex mixtures [3].

In another approach, Raman spectroscopy was equipped with hollow-core photonic crystal fibers to simultaneously quantify several gases, including ethylene (Raman shift located at 1342 cm-1), CO2, and O2 in one single test. Using signal processing to measure the ethylene peak allows very selective sensing. However, Raman spectroscopy requires expensive instrumentation, such as high-power lasers and sensitive detectors [3].

The works of A. M. Akhir et al. [34] and Jin et al. [27] are of special interest. As in those works ethylene gas sensors were fabricated using both SnO and ZnO as a substrate. It was found that the samples with palladium nanoparticles on them had higher sensitivity, a lower operating temperature and faster response times. Below is a summative table of their performances.

Table 2.1: Table comparing and summarizing the results of previous work

Substrate	Doping	LOD	Operating Temperature
ZnO [27]	n-type	10 ppb	300°C
SnO [34]	p-type	50 ppb	350°C

2.5.1. Limitations

Current VOC gas sensors are limited by selectivity, since most gas sensors are cross-sensitive to multiple gasses. In other cases the sensors are not economically viable for large volumes as is the case with gas chromatography or with Raman spectroscopy as they are too big and expensive [3].

2.6. Heating and UV

The recovery time of graphene gas sensors is long even with nanoparticle functionalization and often is incomplete. To improve the recovery heat and ultraviolet (UV) illumination can be used [6, 35]. They can also be used to increase the sensor's performance in general [23, 35].

The slow recovery is primarily attributed to strong adsorption of gas molecules on the graphene surface or at defect sites and functionalization centers. In particular, charge transfer interactions between adsorbates and graphene can lead to long-lived states, which delay the return to equilibrium. By introducing thermal energy, the adsorption–desorption equilibrium can be shifted toward desorption, effectively reducing recovery times. Heating increases the kinetic energy of adsorbed molecules, thereby lowering the residence time on the surface and promoting faster sensor reset [6, 20].

In addition to improving recovery, elevated temperatures can enhance overall sensor performance. For graphene sensors functionalized with metallic or metal-oxide nanoparticles, catalytic activity often increases with temperature. This leads to improved sensitivity and selectivity, as reaction rates between target gas molecules and the catalytic sites are enhanced [23]. However, this must be balanced against increased noise levels and potential degradation of device stability at higher temperatures.

UV illumination provides an alternative or complementary mechanism to thermal activation. Exposure to UV light generates electron–hole pairs in graphene and in the functionalization materials. These photogenerated carriers can assist in breaking the bonds between adsorbed gas molecules and the sensor surface, facilitating desorption [35]. UV can also increase sensitivity by forcing the desorption of surface contaminants. This results in an increase of the number of active adsorption sites thereby increasing sensitivity [35].

2.7. Annealing

To improve the stability of nano-particles and their connection to graphene, an annealing step can be used after functionalization. Annealing involves heating the sample while under controlled conditions. In this work annealing is done in an Oven with inwards nitrogen flow. Since nitrogen is an inert gas it will not contaminate the gas sensor.

During annealing, several important processes can occur. First, contaminants bound to the graphene are removed, resulting in more space for reactive oxygen radicals. Second, thermal energy promotes the reorganization of surface atoms, allowing nanoparticles to adopt energetically favourable configurations, which enhances particle–substrate binding [36].

Annealing at a certain temperature also ensures that gas tests can be performed at and below that temperature. If a gas sensors wasn't annealed and performed a high-temperature test. During the test the nano-particles would be unstable and start sintering [37]. The results would be unusable as the differences in resistance could be dominated by the changing of the nanoparticles.

While annealing can improve electrical contact and reduce interface resistance, excessive annealing may lead to aggregation or clumping of nanoparticles [37], reducing their surface density and potentially degrading device performance. In addition, in this work the annealing temperature is limited by the gold interconnects. As demonstrated in Appendix A, annealing above a critical temperature leads to breakage of the gold interconnects, disrupting the electrical connection to the graphene.

3

Methodology

In this chapter, the experimental methods used in this work are presented. First, the fabrication process of the graphene gas sensor is described, followed by the functionalization process using nanoparticles. Subsequently, the characterization techniques employed to evaluate the structural quality and properties of the graphene are discussed. Finally, the gas sensing measurement setup is presented, and its operating principles are explained.

3.1. Graphene Sensor Production

To produce a graphene based gas sensor with the transfer free CVD graphene method as described in Chapter 2.1.1 a 600nm layer of SiO2 was grown on a p-type silicon wafer using wet thermal oxidation. Afterwards, a 50nm layer of molybdenum was sputter coated and the wafer was coated in positive photoresist. This photoresist was then patterned and developed. The molybdenum could then be plasma etched in the correct pattern.

To grow graphene on the molybdenum an Aixtron Black Magic was used. It is a commercial PECVD equipment specialized in producing graphene films and carbon nanotubes. In this work graphene was deposited using this equipment starting with a pre-anneal of 20 min at 915℃ to remove the surface oxide on the molybdenum. This is then followed by 20 min having methane gas flowed in at 915 ℃. The molybdenum acts as a catalyst for the methane where at this high temperature decomposes into carbon atoms that diffuse into the molybdenum. The carbon atoms then precipitate onto the surface forming graphene [38].

The wafer was then coated with negative photoresist and patterned. Afterwards, 20 nm chromium and 200nm gold was deposited using electron beam evaporation. Chromium was used as an adhesion layer between the gold and SiO and the gold was used because of its good electrical conductivity, contact resistance and for its chemically inertness. The excess chromium and gold on the photoresist was removed by lift-off. With this method gold was deposited on the ends the graphene for contact and to hold it down. Gold was also deposited to some contact pads from which the graphene sheet can be measured. Finally, the molybdenum under the graphene was etched away leaving the graphene only connected to the gold interconnect and the non-conductive SiO2 underneath. The etching of the molybdenum can be visually confirmed by the colour of the graphene as can be seen in Figures 3.1 and 3.2. An example of a sample that was created can be seen in Figure 3.3. A visual overview of the process can be seen in Figure 3.4 and the complete flowchart can be seen in Appendix C.

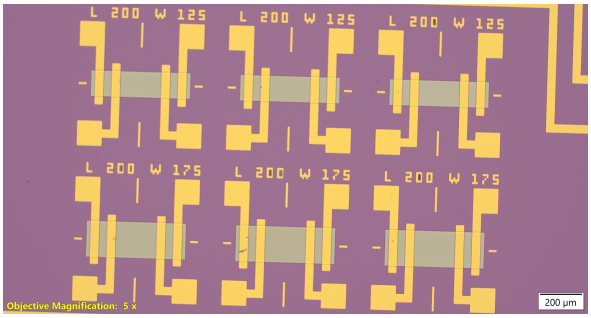

Figure 3.1: Graphene sheets before etching, as can be seen the colour of the graphene sheets is green

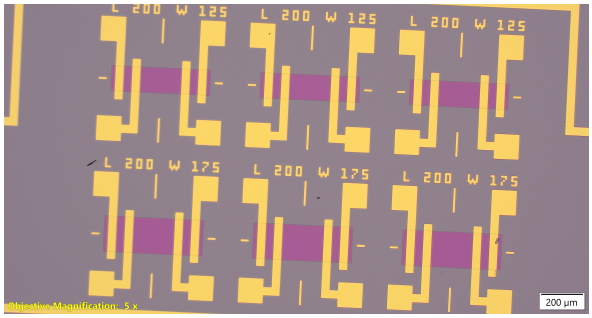

Figure 3.2: Graphene sheets after etching, as can be seen the colour of the graphene sheets is red

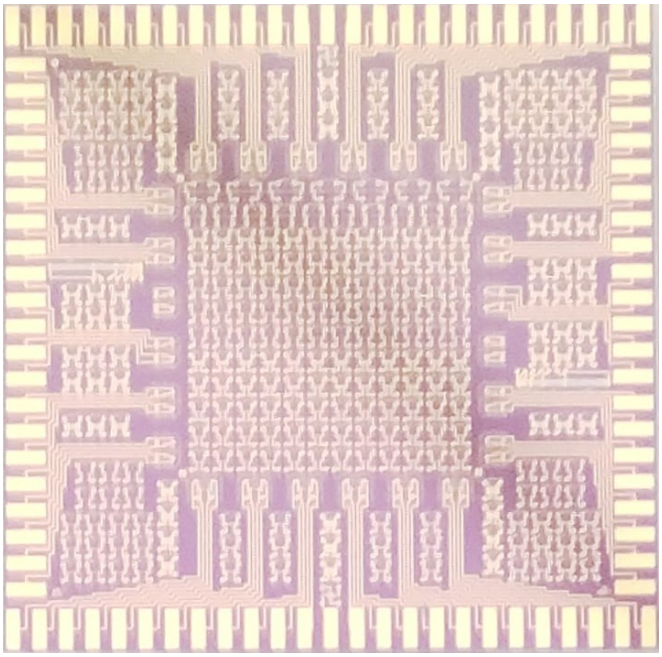

Figure 3.3: Image of a sample after the complete process

(a) Thermally growing a thick layer of SiO2

(b) Depositing a thin layer of Molybdenum

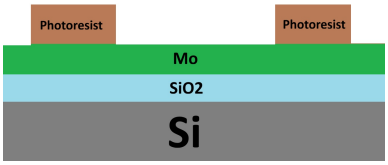

(c) Coating the wafer in Photoresist then patterning it with lithography and developing

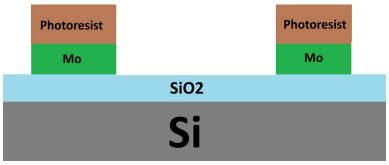

(d) Plasma etching the exposed Molybdenum

(e) Stripping the resist

(f) Growing Graphene on the Molybdenum

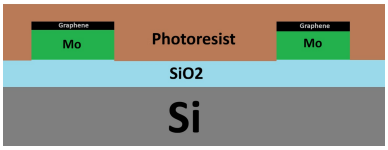

(g) Coating in photoresist

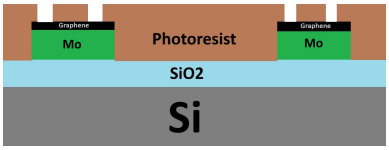

(h) Patterning and developing

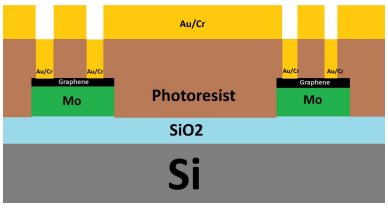

(i) Depositing a layer of Chromium and Gold

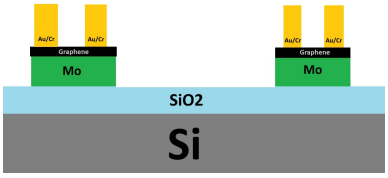

(j) Liftoff of the excess gold

(k) Etching the Molybdenum

Figure 3.4: Overview of the process that was used to fabricate the graphene sensors. Grey is silicon, light blue is silicon oxide, Brown is photoresist, Green is molybdenum, Black is graphene and Yellow is a Gold-Chrome mixture. Cleaning steps and dicing steps were skipped in this overview.

3.1.1. Graphenea graphene strips

Another sample used in this work was a commercial graphene sample supplied by Graphenea. Similar to the multilayer graphene that was produced in-house, this sample was fabricated using chemical vapor deposition (CVD). The graphene strips are connected via gold interconnects and are on a silicon oxide (SiO2) substrate. The exact fabrication details are not known as they are confidential.

This sample was used to improve the sensitivity of the device, as the detection of ethylene was difficult with the in-house samples.

3.2. Spark ablation

The method used in this work for nanoparticle production is spark ablation. Spark ablation uses two metal electrodes that are positioned at a small distance from each other. A short-duration electrical spark is generated between the electrodes, ionizing the carrier gas in the gap and causing material to be ablated from the electrode surfaces. The ablated material rapidly cools due to the flow of an incoming inert carrier gas, resulting in the formation of small nuclei. These nuclei can subsequently collide and agglomerate, forming larger fractal-like nanoparticles [24]. By repeatedly generating sparks at frequencies of several hundred hertz, a continuous and stable production of nanoparticles can be achieved. A schematic illustration of the spark ablation process is shown in Figure 3.5, while an example of the produced nanoparticles is presented in Figure 3.6.

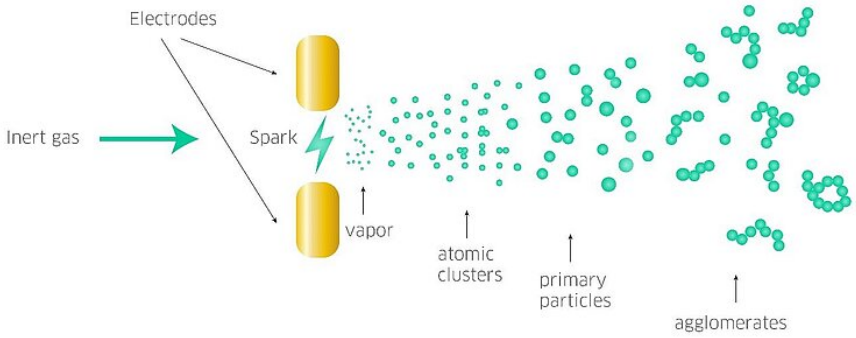

Figure 3.5: Visualization of the spark ablation process [39]

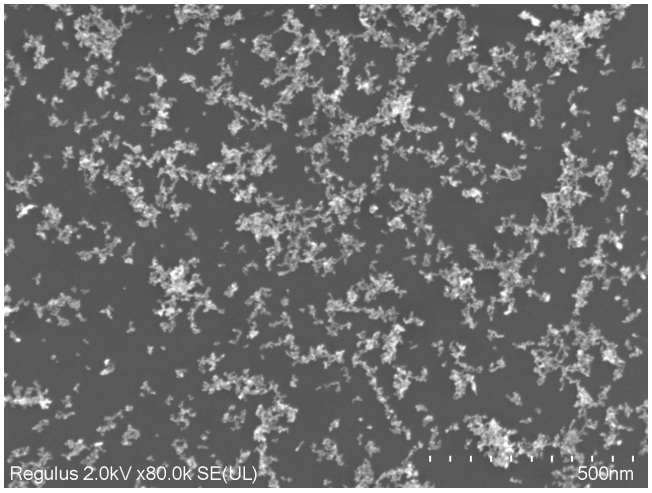

Figure 3.6: Palladium np's SEM image at 80k magnification

The VSParticle system, shown in Figure 3.7, is commercial equipment that combines spark ablation nanoparticle synthesis with an impaction printing chamber. The impaction printing chamber used in this work was a prototype of the VSP-P1 by VSParticle. The system includes a movable nozzle controlled through G-code for precise and automated nanoparticle printing onto target substrates.

During operation, the carrier gas transports the synthesized nanoparticles from the spark ablation source through the nozzle at high velocity, where they are impacted onto the substrate surface. The deposition characteristics can be controlled by adjusting several parameters. For example, the distance between the nozzle and the substrate influences the spread and spatial distribution of the deposited nanoparticles. Additionally, the movement speed of the nozzle and thereby the time above a specific area determine the local nanoparticle density, allowing both sparse and dense coatings to be produced.

The deposition chamber operates under vacuum conditions. To enable repeatable and accurate printing, the system is equipped with a camera mounted on the same mechanical arm as the deposition nozzle. The camera has a fixed offset in the x, y, and z directions relative to the nozzle position. By focusing the camera on a predefined reference point and calibrating the positional offset, reproducible nanoparticle printing can be achieved.

The properties of the generated nanoparticles are strongly influenced by the spark parameters. Increasing the spark voltage or current increases the energy delivered between the electrodes, resulting in a higher ablation rate and larger particles. Furthermore, the carrier gas flow rate affects the cooling dynamics and particle growth process, thereby influencing the average nanoparticle size. However, in practice, precise control over the nanoparticle size distribution using the VSParticle was difficult.

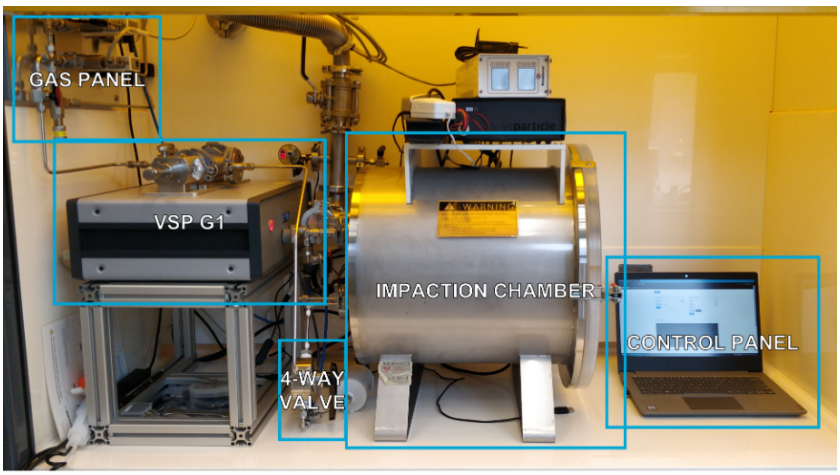

Figure 3.7: VSParticle nanoparticle generator setup. The VSP G1 generates the nano-particles that are impaction printed in the impaction chamber.

3.3. Electrical Measurements

To characterize the electrical properties of the graphene, multiple test devices were fabricated on a single sample. These devices have varying geometries and can be connected to a probe station for measurements such as sheet resistance and electrical conductivity. An example of such a device is shown in Figure 3.8.

In addition to the individual devices, larger contact pads are located along the edges of the sample. These pads are electrically connected to graphene strips, enabling four-point probe measurements without requiring precise probe needle positioning. These contacts pads are also used to read the resistance while in the gas sensing chamber.

The contact pads have two different device geometries that are connected to them. Device type A, shown in Figure 3.9, has a length of 200 μm and a width of 20 μm. Device type B, shown in Figure 3.10, has the same length of 200 μm but a larger width of 40 μm.

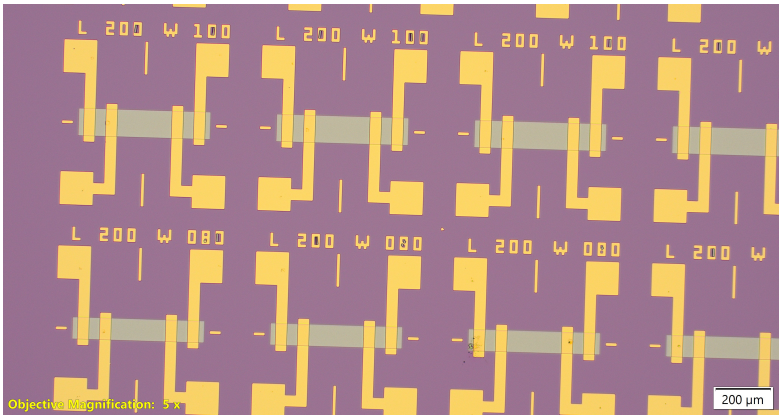

Figure 3.8: Structures to perform 4-point measurements

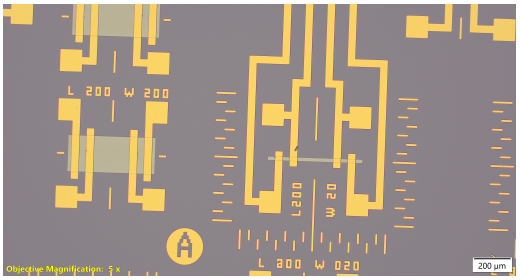

Figure 3.9: Resulting structure of type A

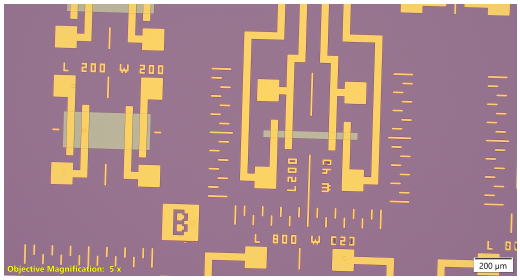

Figure 3.10: Resulting structure of type B

To perform the electrical measurements, a Cascade probe station was used, as shown in Figure 3.11. The probe station is equipped with six micromanipulator probes that can be positioned accurately onto the contact pads of the fabricated structures, such as the device shown in Figure 3.8. The probes are connected with a wire to a Keysight B1500A Semiconductor Device Analyzer where the voltage and currents are accurately read out and applied. This setup enables reliable four-point probe measurements of the graphene devices.

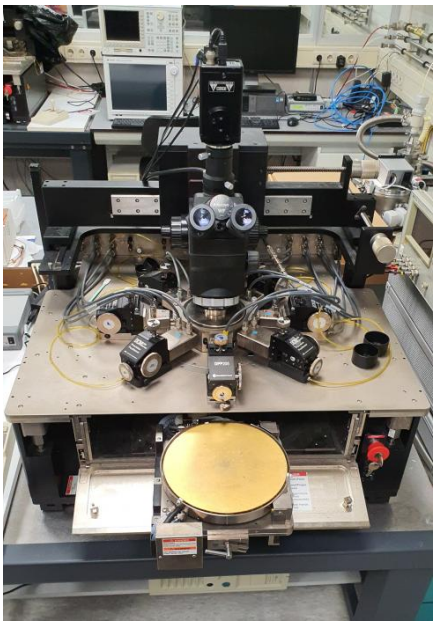

Figure 3.11: Cascade 33 probestation [40]

3.4. SEM

A scanning electron microscope (SEM) is a microscope capable of reaching a high level of magnification and resolution by using a focused beam of electrons in a vacuum instead of visible light. Because electrons have a much shorter wavelength than visible light, SEM systems can achieve resolutions down to the nanometer scale, far exceeding the diffraction limit of optical microscopes. In an SEM, electrons are emitted from a source, accelerated using an anode, and focused using electromagnetic lenses before being directed onto the surface of a specimen. A visualization of this process can be seen in Figure 3.12.

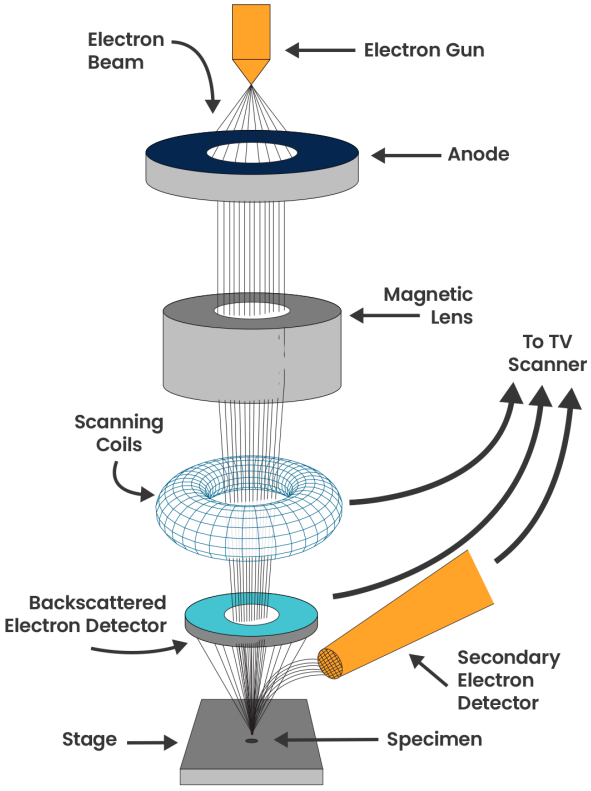

Figure 3.12: Working principles of a SEM[41]

When the electron beam interacts with the sample, a variety of signals are generated. These include secondary electrons (SE) and backscattered electrons (BSE). Secondary electrons are low-energy electrons emitted from close to the surface (typically within a few nanometers) and are primarily responsible for providing high-resolution information about surface morphology and topography. In contrast, backscattered electrons originate from deeper within the sample and are sensitive to the atomic number of the material, making them useful for compositional contrast imaging.

Creating an image in an SEM is achieved by scanning the electron beam across the sample surface in a raster pattern using scanning coils. At each point, the intensity of the detected signal is recorded and mapped to a corresponding pixel in the image. The resulting intensities across the raster produce a grayscale image that visualizes the surface structure.

In SEM charging effects occur when electrons accumulate on the surface of a specimen during imaging. This phenomenon is most common in non-conductive or poorly conductive materials, such as polymers, ceramics, biological samples, and oxides. Since these materials cannot efficiently dissipate the electron charge to ground. The accumulation of charge alters the trajectory of both the incoming primary electrons and the emitted secondary electrons. As a result, SEM images may exhibit artifacts such as excessive brightness or fluctuating contrast. In severe cases, charging can completely prevent stable imaging by causing rapid variations in signal intensity. The effect becomes more pronounced at high beam currents, long exposure times, or when imaging highly insulating materials.

An SEM can also decelerate the electron beam before it reaches the sample surface. This is achieved by applying a bias voltage to the sample, which creates an electric field that reduces the kinetic energy of the incoming electrons. As a result, the electrons strike the sample surface with a lower landing energy. Reducing the electron landing energy decreases the penetration depth of the electrons into the sample [42]. Consequently, the electron interactions become more surface-sensitive, improving the imaging contrast and resolution of thin surface structures. This is useful for observing materials such as graphene.

The SEM used in this work is the Hitachi Regulus 8230 and can be seen in Figure 3.13. For most of the visualisation and characterization of nano-particles and graphene the magnifications used are in the range of 40-80k. For nano-particles the acceleration voltage used was 2kV and only the SE detector was used. For graphene deacceleration was used to improve the surface detail with 1kV as the deacceleration voltage and both the SE and BSE detectors were used.

Figure 3.13: Hitachi Regulus 8230 [43]

3.5. Raman Spectoscopy

Raman spectroscopy is characterization technique used to gain information from the vibrational, rotational, and other low-frequency modes of molecules. It is based on the Raman effect which describes the inelastic scattering of photons when light interacts with molecular vibrations. When monochromatic light (typically from a laser) irradiates a sample, most photons are elastically scattered (Rayleigh scattering). A small fraction, however, undergoes inelastic scattering, resulting in a shift in energy corresponding to molecular vibrational transitions. These shifts, known as Raman shifts, are characteristic of specific chemical bonds and symmetry properties of molecules, allowing for molecular identification.

A Raman spectroscopy system consists of several key components. First, a laser is focused onto the sample surface, where the incident photons interact with the material. The Rayleigh scattered photons are filtered out using an optical filter, allowing only the inelastically scattered photons to pass through. The remaining photons, which contain the Raman spectral information, are directed onto a diffraction grating. The grating spatially separates the photons according to their wavelength, thereby dispersing the Raman signal into its spectral components. Finally, the dispersed photons are detected by a photodetector, typically a charge-coupled device (CCD), which records the intensity as a function of wavelength to produce the Raman spectrum. A schematic of this process can be seen in Figure 3.14.

3.5.1. Graphene Raman spectroscopy

To evaluate the quality of the graphene samples, Raman spectroscopy was used. Figure 3.15 shows representative Raman spectra for different types of graphene. The Raman spectrum of graphene contains

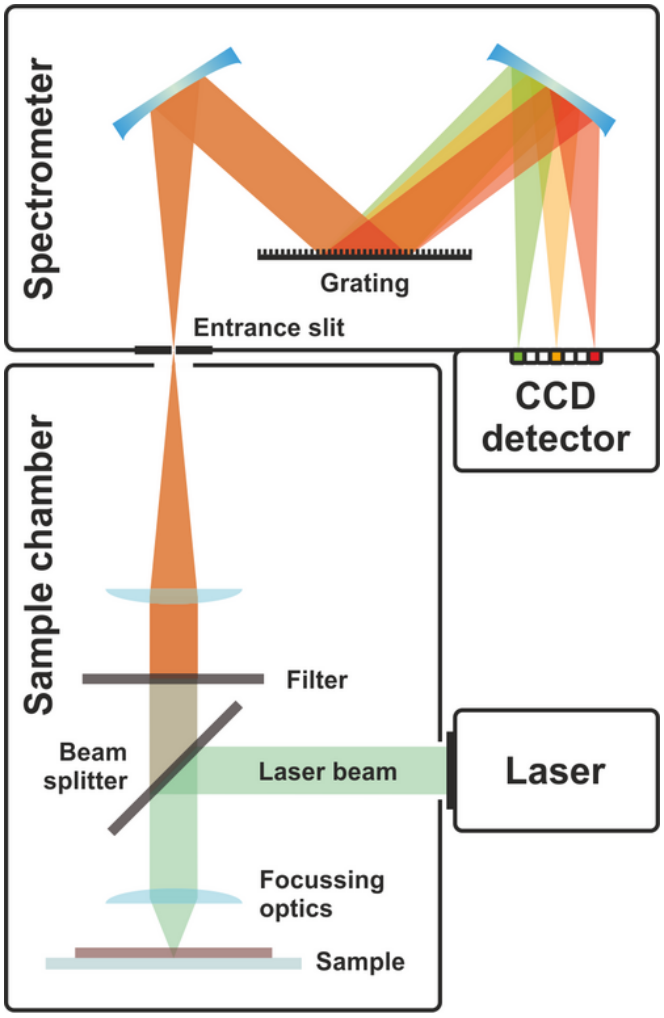

Figure 3.14: Schematic of a Raman Spectroscopy device [44]

three characteristic peaks that provide important information about the material quality, defect density, and number of layers.

The first characteristic feature is the D peak, located around 1350 cm^{-1}. The D peak is associated with defects in the graphene lattice and becomes stronger as the amount of defects increases. The G peak, located near 1580 cm^{-1}, originates from the in-plane vibration of sp^2-bonded carbon atoms and is present in all graphitic materials. The intensity ratio between the D peak and the G peak, I_D/I_G, can be used to estimate the level of defects present in the material. In addition to the intensity ratio, the full width at half maximum of the G and D peak, denoted as FWHM(G) and FWHM(D) respectively, provides further information on the defectiveness of the graphene [45].

The 2D peak, typically observed around 2700 cm^{-1}, can be used for information on the number of graphene layers. The intensity ratio I_{2D}/I_G can be specifically used for this purpose. When $I_{2D}/I_G < 1$, the material is generally classified as multilayer graphene (MLG). Ratios between 1 and 2 indicate few-layer graphene (FLG), while ratios of approximately 2 or higher are characteristic of single-layer graphene (SLG) [46].

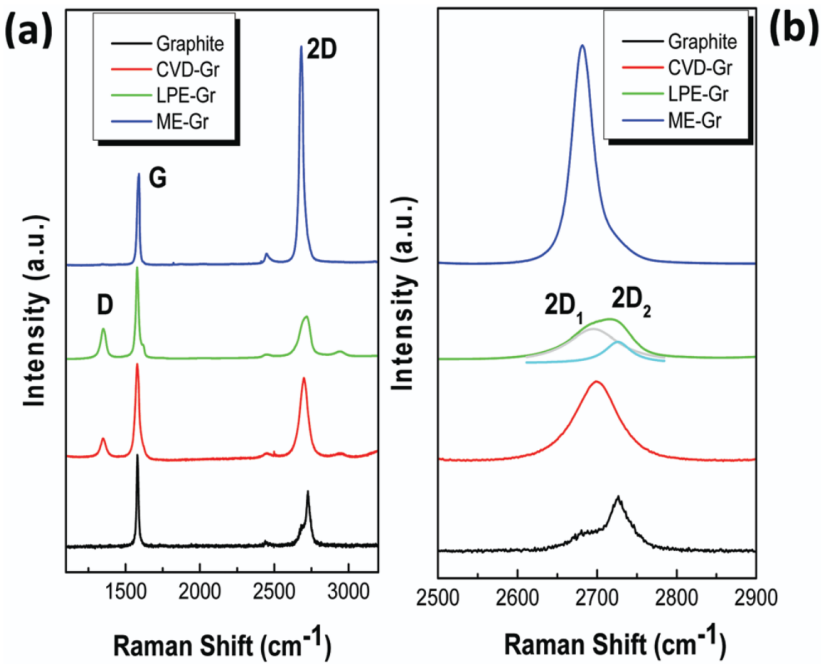

Figure 3.15: Example of different graphene Raman Spectra. (a) Spectrum containing the D,G and 2D peaks. (b) Spectrum zoomed in into the 2D peak [47]

Defects play an important role in the gas sensing performance of graphene-based materials. From a sensing perspective, a more defective morphology indicates the presence of high-energy binding sites, whereas a smoother and less defective structure primarily consists of low-energy binding sites [47].

For the Raman spectrum acquisition in this work, a Horiba AFM-Raman LabRAM Odyssey Nano system was used. Raman spectra were acquired using a green laser with a wavelength of 532 nm with a grating of 1800(500nnm). In addition, a 100× objective magnification was employed. The machine can be viewed in Figure 3.16

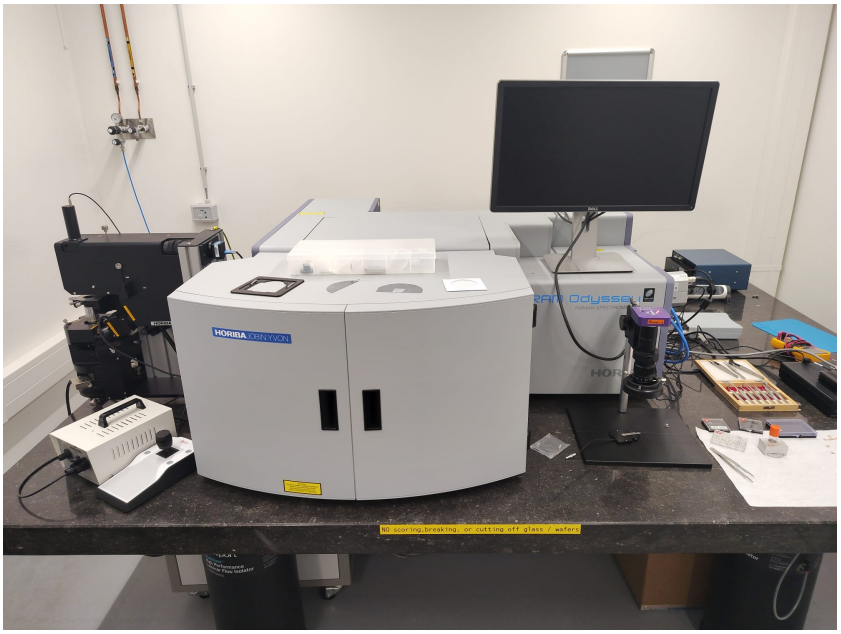

Figure 3.16: Horiba AFM-Raman LabRAM Odyssey Nano

3.6. Gas Measurements

To evaluate the performance of the gas sensors, controlled gas sensing measurements were performed. During these measurements, the sample is placed inside a sealed measurement chamber in which the environmental conditions can be carefully controlled. By exposing the sensor to different gas concentrations, the electrical response of the sample can be recorded.

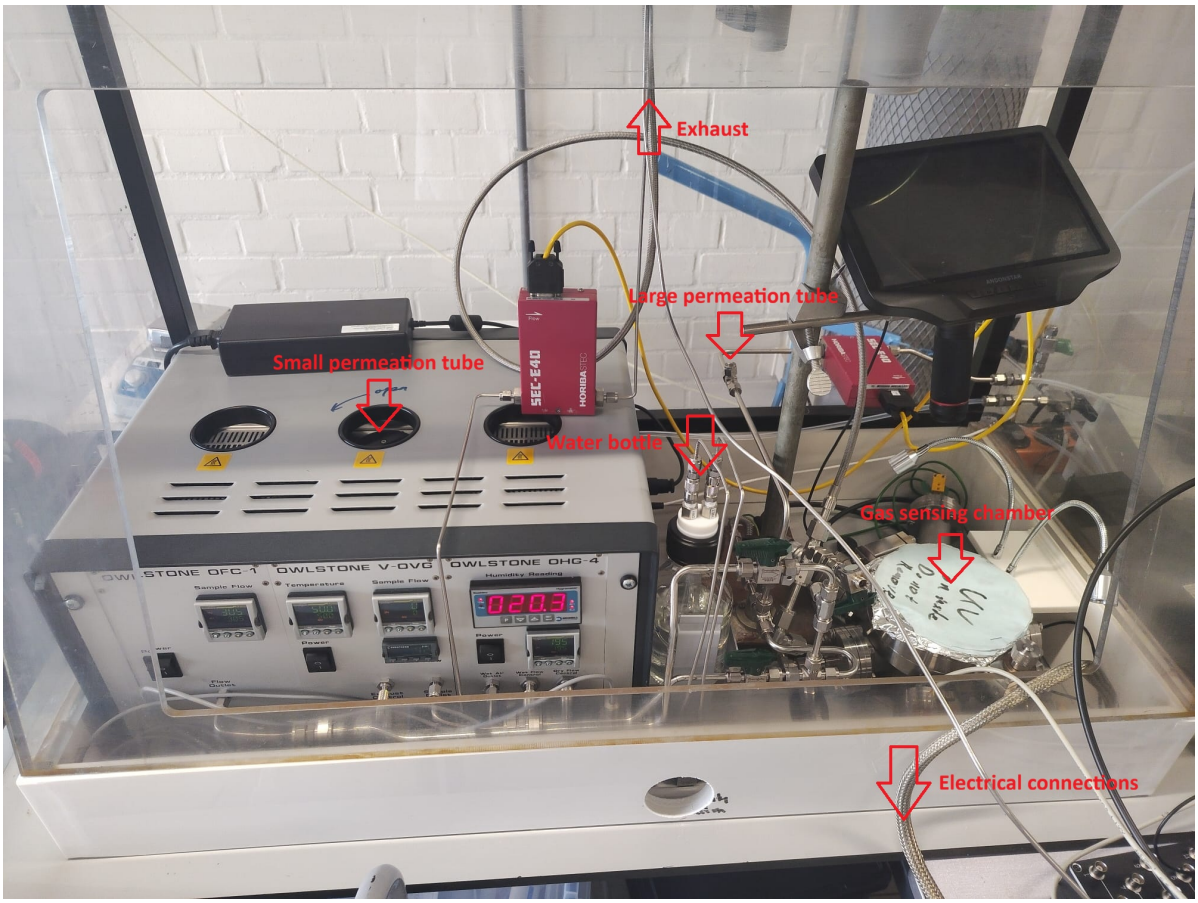

Figure 3.17: The gas measurement setup

In this work an Owlstone V-OVG system was used, and can be seen in Figure 3.17. Different gasses were available using permeation tubes, which could either be placed directly inside the V-OVG system or connected externally through a mass flow controller. A permeation tube is a device containing a target gas enclosed by a permeable membrane. The system also uses a carrier gas transport the target gas to the chamber and to dilute it to the right concentration. The carrier gas used in this work is nitrogen.

Two different permeation tube sizes were used in this study. Smaller permeation tubes could be inserted directly into the V-OVG chamber, while larger permeation tubes had to be connected externally through the gas piping system. Examples of these permeation tubes are shown in Figures 3.19 and 3.20. By adjusting the carrier gas flow through the V-OVG chamber containing a permeation tube, different target gas concentrations could be generated and delivered to the sensor device. The complete experimental setup is shown in Figure 3.17, while a schematic overview of the gas sensing system is presented in Figure 3.18.

Inside the gas sensing chamber, pins establish contact with the graphene sensor structures, enabling resistance measurements during gas exposure. These probes are connected through a pinout board to a voltage source and data acquisition system. Using a custom LabVIEW script, the resistance of the graphene devices could be recorded automatically while simultaneously controlling the gas flow conditions.

This setup enabled automated gas sensing measurements in which the gas concentration could be

varied systematically to observe the sensor response over time. For measurements using the smaller permeation tubes, the entire process was operated fully automatically. However, when using the larger permeation tubes, manual operation was required. Since these larger tubes continuously release gas and do not include a dedicated exhaust mechanism, residual gas could remain in the system and contaminate the measurement cycle during periods when the target gas was intended to be absent. To avoid this issue, the gas valves and flow paths had to be switched manually during measurements involving the larger permeation tubes.

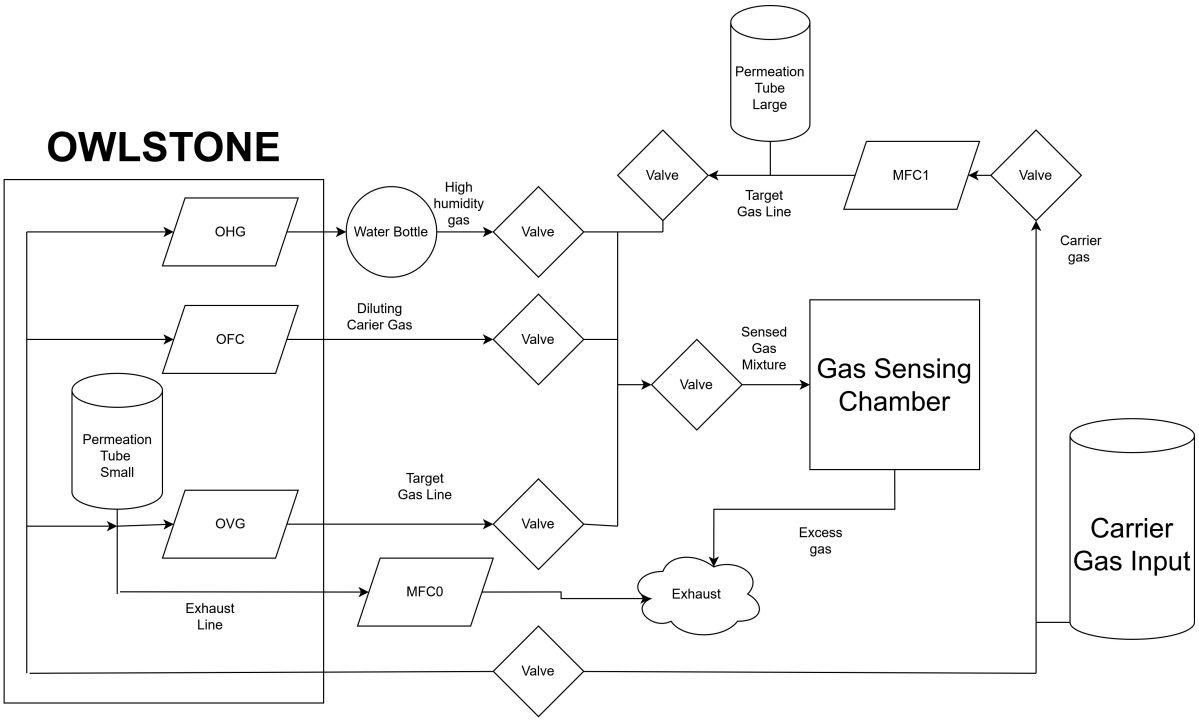

Figure 3.18: Schematic overview of the gas sensing setup

3.6.1. Concentration of gasses

Permeation tubes release a known amount of gas, typically specified in units such as ng/min or mol/min, at a calibrated temperature. The resulting gas concentration delivered to the sensing chamber depends on the permeation rate in combination with the applied carrier gas flow. Increasing the carrier gas flow lowers the gas concentration, as the released gas becomes distributed over a larger volume of carrier gas.

Additionally, the concentration can be reduced further by exhausting a portion of the gas flow before it reaches the sensing chamber. Afterward, the remaining flow can be diluted by mixing it with an additional clean carrier gas stream. The unit of the flows are Standard Cubic Centimeters per Minute (sccm). By accurately controlling and calculating these three flow components, the permeation tube flow (OVG or MFC 1), exhaust flow (MFC 0), and dilution flow (OFC), it is possible to create a desired gas concentration while maintaining a controlled total flow towards the sensing chamber.

At high target gas concentrations, the primary limitation is often the permeation rate of the permeation tube itself. Although reducing the carrier gas flow increases the concentration, the flow cannot be reduced excessively, as a minimum flow is required to transport the gas effectively to the sensor chamber. Lower concentrations are generally easier to achieve, since the setup allows for a large exhaust flow and dilution flow.

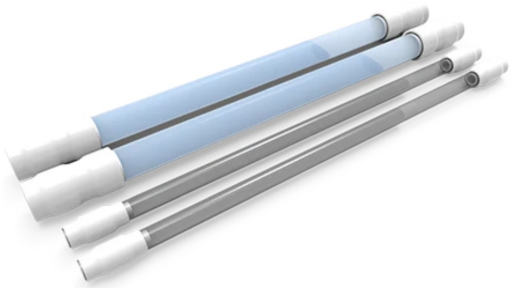

Figure 3.19: Small permeation tubes [48]

Figure 3.20: Large permeation tube [49]

The setup also includes humidity control. A portion of the clean carrier gas can be flown (OHG) through a water-filled bottle, where gas bubbles absorb water vapor before being mixed back into the main gas stream. In this way, the relative humidity of the gas delivered to the sensing chamber can be increased and controlled during measurements.

For large permeation tube measurements, no exhaust flow was used because the exhaust line was not connected in the setup, as shown in the top-right section of Figure 3.18. Consequently, during these measurements, the gas concentration and total flow rate were linearly coupled.

The small permeation tubes were housed inside a temperature-controlled chamber, allowing their operating temperature to be adjusted to match the calibration temperature specified by the manufacturer. In contrast, the large permeation tubes were operated at the ambient temperature of the lab without active temperature stabilization. Since the temperature sensor inside the V-OVG system indicated a room temperature of 19 ℃ during the morning measurements, this value was assumed as the worst-case operating temperature.

For the large ethylene permeation tube, the manufacturer calibration temperature was specified as 25 ℃. The resulting temperature difference of 6 ℃ is estimated to result in an approximately 8% reduction in permeation rate according to the data sheet [49]. For the purposes of this work, this variation was considered acceptable, since the objective was to evaluate the influence of nanoparticle functionalization. Because both pristine graphene and nanoparticle-functionalized graphene devices were measured under the same conditions, the temperature-induced concentration deviation affects both equally. However, for precise gas concentration calibration or comparison between separate experimental runs, this temperature dependence should be kept in mind.

4

Material Characterization

In this chapter, the material characterization results of the graphene gas sensors are presented and discussed. The chapter begins with the optimization of the nanoparticle area coverage, including the influence of the annealing process on the deposited nanoparticles. Subsequently, SEM images of the graphene samples are presented and discussed. This is followed by an analysis of the Raman spectra, which provide further insight into the quality of the graphene devices. Finally, sheet resistance measurements of the various graphene strips are presented and discussed.

4.1. Optimization of nanoparticle printing

To achieve the desired nanoparticle area coverage, the deposition parameters of the VSParticle system must be optimized. Several process parameters can be adjusted, including the carrier gas flow rate, printing speed, spark voltage, and spark current. Smaller nanoparticles are preferred due to their reduced sensitivity to fluctuations in area coverage as was found in the model of Abideen et al. [30]. To reduce the nanoparticle size a high carrier gas flow was used to promote rapid cooling and limit particle growth.

The printing speed is constrained by the mechanical limits of the system, with a maximum speed of 200 mm/min. Although the minimum programmable speed is 0.3 mm/min, this lower limit was not restrictive in practice because the same region can be printed multiple times to increase the deposited nanoparticle density. The spark voltage and current not only influence the nanoparticle production rate but also affect the resulting particle size distribution. To reduce the nanoparticle area density, either the printing speed can be increased or the spark energy can be lowered. In the work of Husain et al. [8] an optimal area coverage of 2% was found for detecting NO2 with silver nanoparticles while also using spark ablation. For that reason a target goal of 1% area coverage was set, since higher densities are more accessible.

To determine the relationship between printing speed and nanoparticle deposition density, a calibration procedure was performed. First, a series of lines with increasing printing speeds was deposited onto silicon test substrates, as shown in Figures 4.1 and 4.2. Subsequently, SEM images of the deposited nanoparticle patterns were acquired, an example of which is shown in Figure 4.3. Finally, an image analysis script was used to estimate the nanoparticle area coverage from the SEM images. The script used in this work is based on that of Rice [50] and can be found in Appendix D.

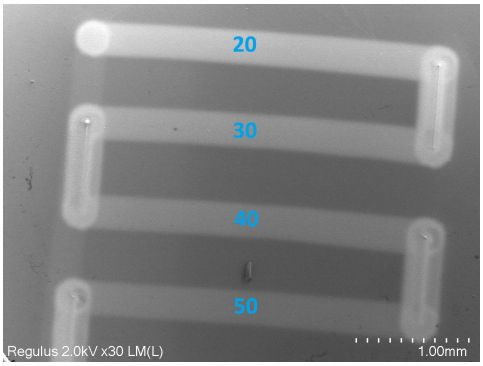

Figure 4.1: Palladium nanoparticles printed lines with a speed from 20 until 50. As can be seen lines with slower speed have a higher density of nanoparticles and are brighter

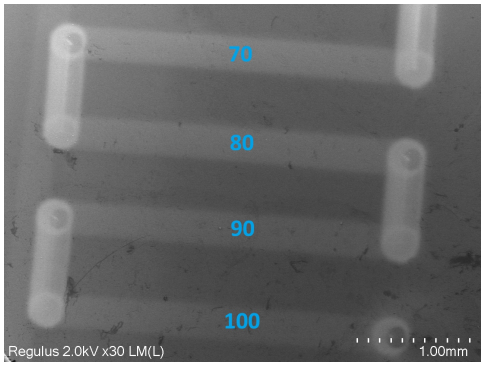

Figure 4.2: Palladium nanoparticles printed lines with a speed from 70 until 100. As can be seen lines with slower speed have a higher density of nanoparticles and are brighter

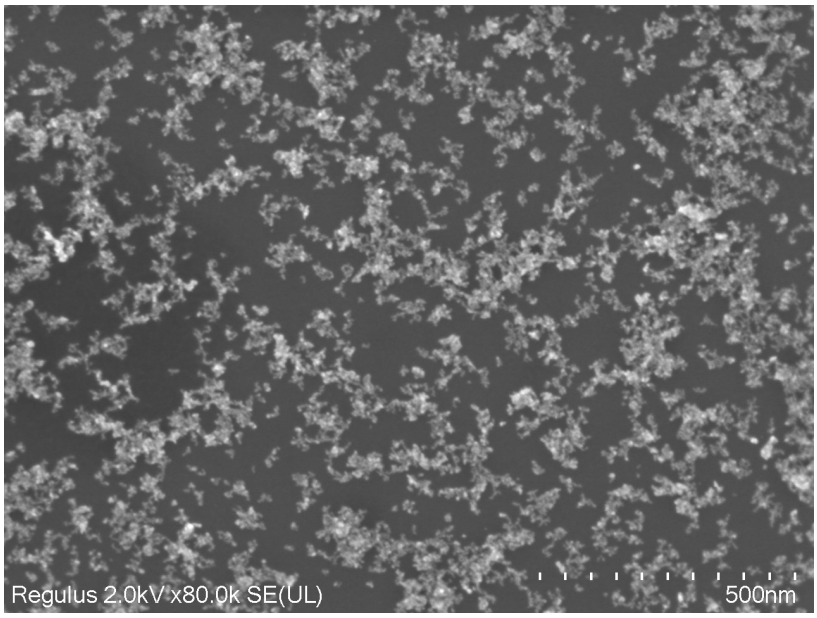

Figure 4.3: non-annealed Palladium particles printed with speed 80 at 1.5L 1kv 8mA

The image analysis script uses Otsu's thresholding method to distinguish nanoparticles from the silicon background. Pixels with intensities above the calculated threshold are classified as part of nanoparticles, while darker pixels are identified as the background. Although this approach provides an automatic method for estimating nanoparticle coverage, it has several limitations and sources of errors.

Firstly, non-uniform background illumination can lead to inaccuracies in the image analysis. Variations in illumination may cause certain regions of the substrate background to appear brighter than poorly illuminated nanoparticles, making reliable separation between nanoparticles and background more difficult. This is especially difficult on graphene, where white spots on the surface are often brighter than the nano-particles as can be seen in Figure 4.4. To still get an accurate area estimation the bright spots are manually removed as is shown in Figure 4.5.

Secondly, noise can shift the background intensity closer to the intensity of the nanoparticles, reducing the contrast between the two. To minimize this effect, long SEM exposure times are required in order to improve the signal-to-noise ratio. Finally, image resolution also significantly influences the accuracy of the area coverage estimation. At lower resolutions, such as 640×480 pixels, fine nanoparticle features become blurred together with the background, resulting in less accurate thresholding and coverage calculations.

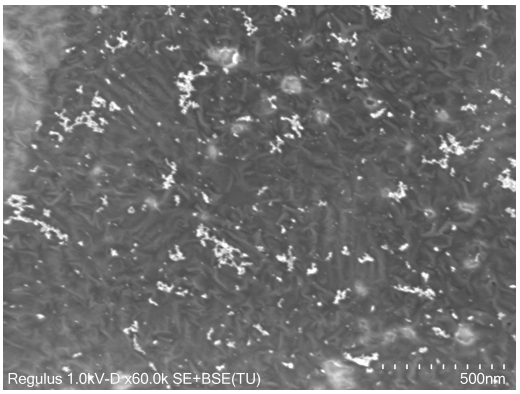

Figure 4.4: Graphene functionalized with Palladium nano-particles with white spots and bright areas

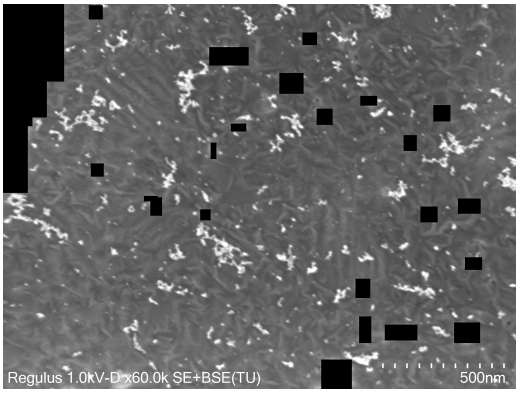

Figure 4.5: Graphene functionalized with Palladium nano-particles with white spots and bright areas removed

In addition, Otsu's thresholding method only performs reliably when the number of nanoparticle pixels and background pixels are of the same order of magnitude. At high nanoparticle densities, typically around 70% area coverage or greater, the intensity variation within the nanoparticles themselves begins to dominate. As a result, Otsu's method may incorrectly place the threshold between darker and brighter regions of the nanoparticles rather than between the nanoparticles and the substrate background. This is undesirable, as portions of the nanoparticles may then be incorrectly classified as background. In such cases, accurate area coverage estimation requires the threshold to be set manually rather than determined automatically using Otsu's method.

4.1.1. Pd

The optimization of the Palladium nanoparticle deposition process started with a carrier gas flow of 1.5 L/min, as this setting was expected to provide stable nanoparticle transport and deposition conditions. The initial process parameters consisted of a spark voltage of 1 kV and a spark current of 8 mA. The resulting area coverages are summarized in Table 4.1.

Table 4.1: Results of the first Palladium printing test, printed with 1.5 L/min carrier gas flow, 1 kV spark voltage, and 8 mA spark current.

Printing speed (mm/min)	20	30	40	50	60	70	80	90	100
Density (% area covered by nanoparticles)	72	59	49	41	37.5	31.6	27.9	24.7	19.6

As shown in Table 4.1, increasing the printing speed reduced the deposited nanoparticle density, as expected. However, even at the highest tested speed of 100 mm/min, the nanoparticle coverage remained above the target value of 1%. This indicated that the nanoparticle production rate was too high and could not be compensated sufficiently by printing speed alone.

To reduce the deposited nanoparticle density further, the spark current was decreased from 8 mA to 3 mA, thereby lowering the spark energy and reducing the amount of material ablated from the electrodes. The results of this second optimization step are presented in Table 4.2.

Table 4.2: Results of the second Palladium printing test, printed with 1.5 L/min carrier gas flow, 1 kV spark voltage, and 3 mA spark current.

Printing speed (mm/min)	10	20	40	60	80	100	135	170	200
Density (% area covered by nanoparticles)	97	54.2	27.7	22.0	16.2	12.5	11.2	10.2	6.0

Reducing the spark current significantly decreased the deposition density across all printing speeds, confirming that the spark current strongly influences the nanoparticle generation rate. Nevertheless, even at the maximum printing speed of 200 mm/min, the deposited area coverage remained above the desired 1% target. This suggests that further reduction of the spark energy or additional optimization

of the gas flow conditions would be required to achieve very low-density Palladium nanoparticle depositions.

4.1.2. Pt

The first Platinum nanoparticle printing experiments were performed using a carrier gas flow of 1.5 L/min, a spark voltage of 1 kV, and a spark current of 4 mA. The resulting nanoparticle area coverages are shown in Table 4.3.

Table 4.3: Results of the first Platinum printing test, printed with 1.5 L/min carrier gas flow, 1 kV spark voltage, and 4 mA spark current.

Printing speed (mm/min)	8	10	12	18	20	22	30	40	50
Density (% area covered by nanoparticles)	67.9	57.43	31.7	25.7	21.09	31.7	0.7	0.49	0.47

The obtained results showed inconsistent deposition behaviour. At lower printing speeds, the nanoparticle density was relatively high, while at higher speeds almost no material was deposited. Additionally, the measured densities did not follow a trend, as the deposition density unexpectedly increased again at 22 mm/min. Several possible explanations exist for this instability. One possibility is that the spark energy was too high, resulting in excessive and unstable material production. Another possible explanation is that the VSparticle wasn't cleaned and there was material accumulation in the piping that was released when the print started.

To obtain more stable and lower-density Platinum depositions, the process parameters were adjusted by increasing the carrier gas flow and reducing both the spark voltage and spark current. The results of the second optimization experiment are shown in Table 4.4.

Table 4.4: Results of the second Platinum printing test, printed with 2 L/min carrier gas flow, 0.3 kV spark voltage, and 2 mA spark current.

Printing speed (mm/min)	2	4	8	16	32	64	100
Density (% area covered by nanoparticles)	63	60	41	20	11	8	6

The modified process conditions resulted in a significantly more stable and predictable relationship between printing speed and nanoparticle density. As expected, increasing the printing speed reduced the deposited nanoparticle coverage. Although the deposition density was still relatively high for some application, the overall process behavior became considerably more controllable compared to the initial Platinum printing.

4.1.3. SnO

For the deposition of SnO nanoparticles, the process parameters were set to a carrier gas flow of 2 L/min, a spark voltage of 1 kV, and a spark current of 4 mA. The resulting deposition densities are summarized in Table 4.5.

Table 4.5: Results of the SnO printing test, printed with 2 L/min carrier gas flow, 1 kV spark voltage, and 4 mA spark current.

Printing speed (mm/min)	2	4	8	16	32	64	90	100
Density (% area covered by nanoparticles)	96	94	72	55	28	16	15	11

The relationship between printing speed and nanoparticle area coverage shows a stable relation. As expected, increasing the printing speed reduced the deposited nanoparticle density. However, the overall deposition rate remained relatively high, suggesting that future optimization could focus on reducing the spark energy further in order to achieve lower nanoparticle coverages.

4.1.4. Results on graphene

After optimizing the deposition parameters on silicon test substrates, Palladium nanoparticles were deposited directly onto graphene samples. The resulting nanoparticle coverages for the Grapheana

graphene are presented in Table 4.6.

Table 4.6: Results of Palladium printing on Grapheana graphene, printed with 2 L/min carrier gas flow, 1 kV spark voltage, and 3 mA spark current.

Printing speed (mm/min)	30	25x1	25x2	25x3
Density (% area covered by nanoparticles)	7.1	7.5	15.2	30.1

The notation 25×1, 25×2, and 25×3 refers to repeated printing passes over the same region at a printing speed of 25 mm/min. As expected, multiple passes resulted in a significant increase in nanoparticle area coverage.

Additional Palladium deposition was also performed on multilayer graphene samples. The results are shown in Table 4.7. Interestingly, differing amount of area coverage was printed under the same settings. This suggests that the printing was inconsistent. One explanation for this might be that during one print the VSparticle was not cleaned enough, and the nozzle was clogged. Functionalization with the same printing settings on the grapheana and in-house sample can be viewed in Figures 4.6 and 4.7 respectively.

Table 4.7: Results of Palladium printing on graphene, printed with 2 L/min carrier gas flow, 1 kV spark voltage, and 3 mA spark current.

Printing speed (mm/min)	25	70	100	150	200
Density (% area covered by nanoparticles)	5.18	2.23	1.48	1.05	0.76

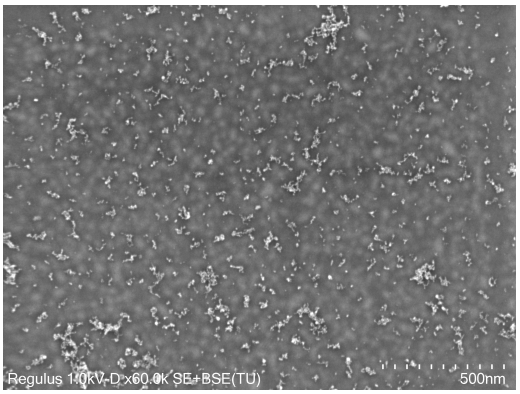

Figure 4.6: Grapheana graphene functionalized with Palladium at 25 mm/min

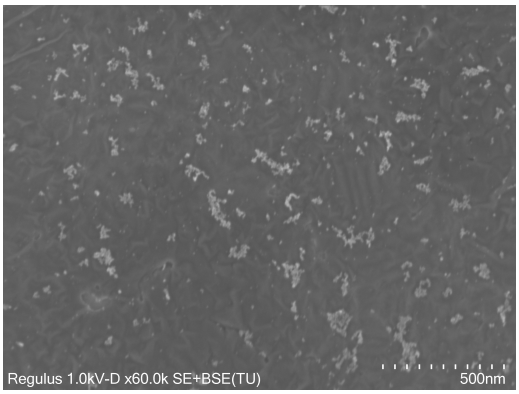

Figure 4.7: In-house graphene functionalized with Palladium at 25 mm/min

These results demonstrate that by increasing the printing speed, very low nanoparticle coverages approaching 1% can be achieved on graphene substrates. Compared to the earlier optimization measurements on silicon substrates, the graphene samples exhibited lower deposition densities under similar printing conditions. This difference may be related to differing properties of graphene and silicon such as their surface roughness.

4.2. Effects of Annealing

In this section, the influence of annealing on the nanoparticle area coverage is investigated. First, the effects of a high temperature annealing on nanoparticles deposited on silicon substrates are examined. Subsequently, the influence of a lower temperature annealing process on nanoparticles deposited on graphene is shown. This latter annealing process corresponds to the final annealing step used during the fabrication of the graphene gas sensors.

4.2.1. Annealing on silicon

As shown in Figures 4.8 and 4.9, annealing Platinum nanoparticles at elevated temperatures causes the nanoparticles to sinter and agglomerate into larger clusters. During this process, neighbouring nanoparticles merge together, resulting in denser and more compact structures. Consequently, the overall nanoparticle area coverage decreases.

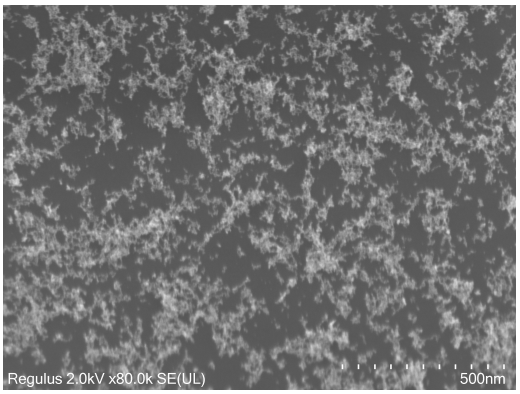

Figure 4.8: Pt

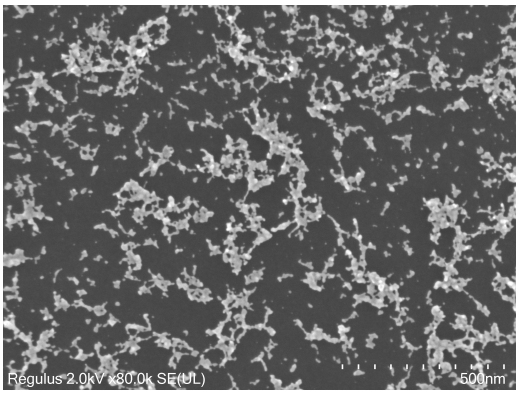

Figure 4.9: Pt after 400 °C20 min

A similar effect is observed for Palladium nanoparticles. As can be seen in Figures 4.10 and 4.11, annealing causes the initially dispersed nanoparticles to cluster together, thereby reducing the effective surface coverage.

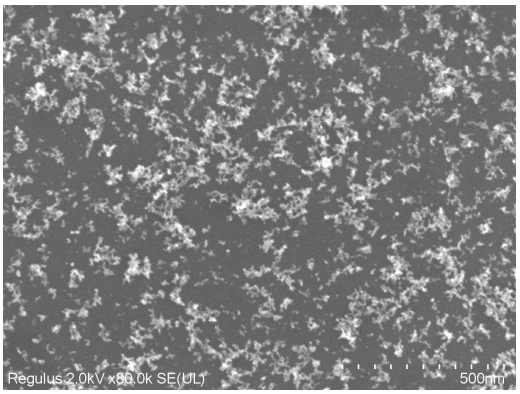

Figure 4.10: Pd

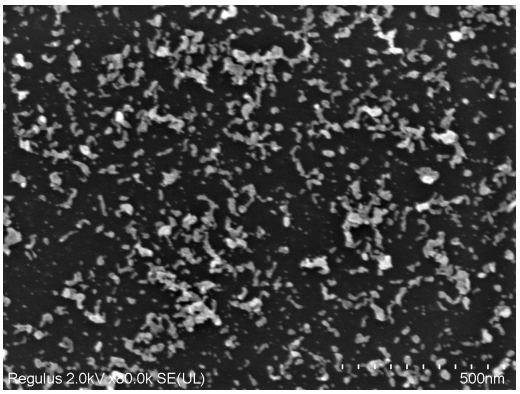

Figure 4.11: Pd after 400°C 20 min

The reduction in nanoparticle area coverage after annealing is consistently observed across all printing speeds. As can be seen in Figures 4.12 and 4.13. The results indicate that annealing leads to more compact nanoparticle structures with reduced projected surface area. This behaviour can be attributed to nanoparticle sintering. At higher temperatures, the nanoparticles gain sufficient surface mobility to diffuse and reorganize on the substrate. As a result, neighbouring nanoparticles merge together to minimize their total surface energy. This effect can occur at temperatures much lower than the materials melting point [37].

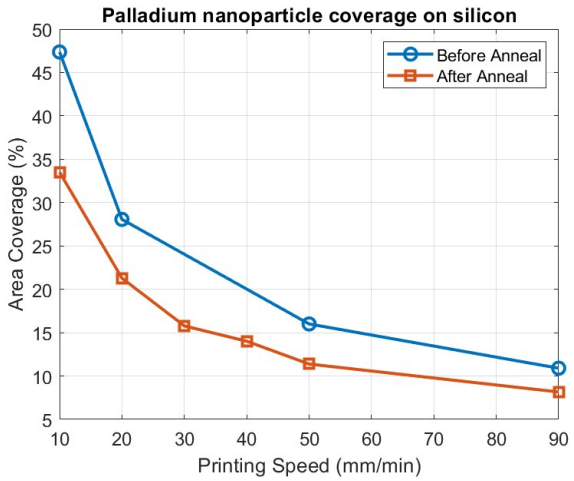

Figure 4.12: Palladium np's coverage before and after annealing at 400°C for 20 min

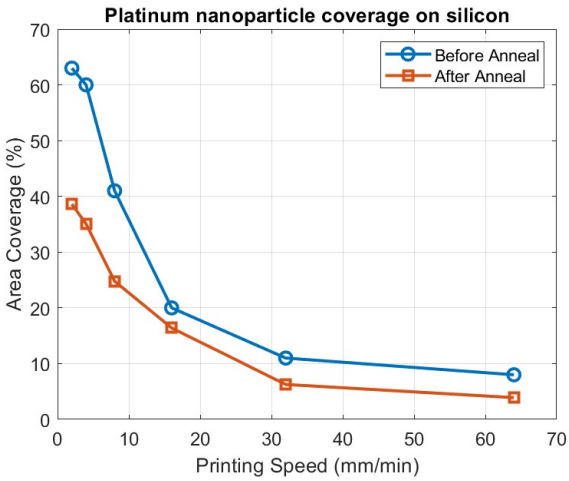

Figure 4.13: Platinum np's coverage before and after annealing at 400°C for 20 min

4.2.2. Annealing on graphene

The same effects observed on silicon substrates are also present when nanoparticles are deposited on graphene. Figures 4.14 and 4.15 show Palladium nanoparticles on graphene before and after annealing.

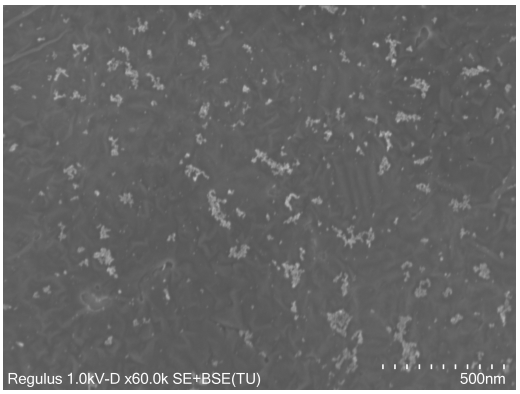

Figure 4.14: Pd

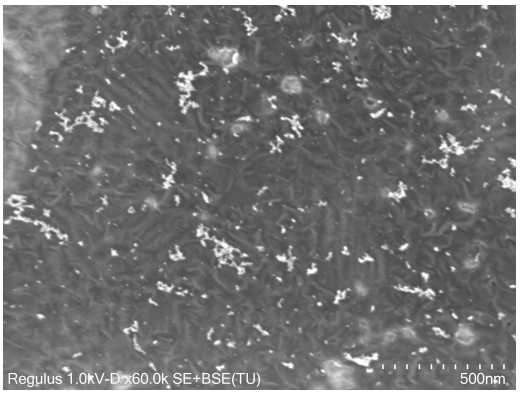

Figure 4.15: Pd after 150°C 60 min

As shown in Figure 4.16 and summarized in Table 4.8, the nanoparticle area coverage decreases after annealing, with the nanoparticle area after annealing being around 90% of the area before annealing. Although this reduction is smaller than the decrease observed for the annealing performed on silicon, the difference can largely be explained by the significantly lower annealing temperature used for the graphene samples. The lower temperature was needed since the fabricated sensors break at higher temperatures as can be seen in Appendix A.

The observed reduction in nanoparticle coverage after annealing should be taken into account when designing and characterizing the graphene gas sensors, since the final nanoparticle density after annealing differs from the initially deposited coverage.

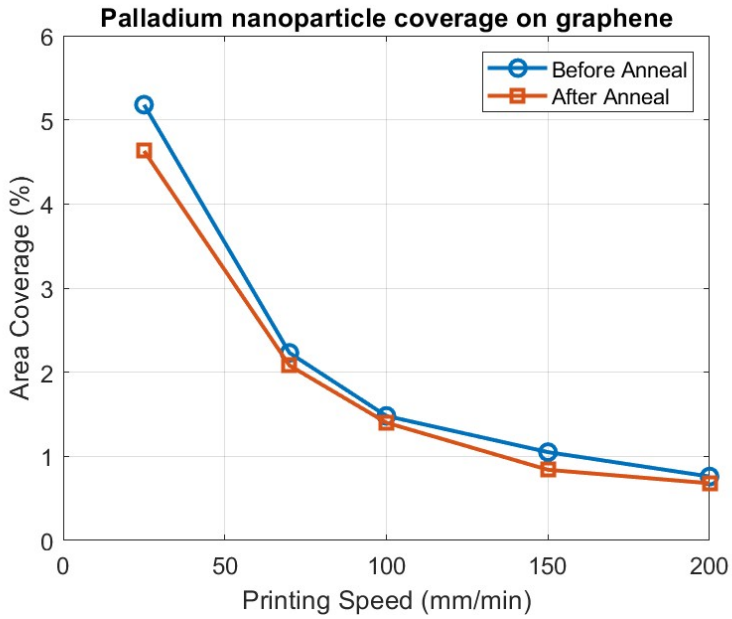

Figure 4.16: Palladium np's on graphene coverage before and after annealing at 150°C for 1 hour

"

Table 4.8: Results of Palladium printing on graphene after annealing, printed with 2 L/min carrier gas flow, 1 kV spark voltage, and 3 mA spark current.

Printing speed (mm/min)	25	70	100	150	200
Density before annealing (% area covered by nanoparticles)	5.18	2.23	1.48	1.05	0.76
Density after annealing(% area covered by nanoparticles)	4.63	2.08	1.40	0.84	0.68

4.3. SEM

The Scanning Electron Microscopy (SEM) was used to visually inspect the graphene samples and evaluate their surface. Figure 4.17 shows a high-magnification SEM image of multilayer graphene (MLG) prior to the removal of the molybdenum substrate. The graphene appears to consist of overlapping and interconnected flakes. There are some minor wrinkles, which are likely the cause of the small mismatch of thermal expansion coefficient between graphene and the molybdenum. The wrinkles appear during cooling after graphene was grown [51]. White dots can also be seen in the SEM image. These could be defects where charge gets trapped resulting in a white charging effect when looked under with a SEM, however it is still unclear what exactly causes these white dots.

After etching away the molybdenum, the surface of the graphene changes noticeably, as shown in Figure 4.18. The surface looks rougher as it has many wrinkles. The increase of wrinkles is likely due to the process of removing the molybdenum layer. In that process hydrogen peroxide is used to etch the molybdenum where afterwards water is added to flow away the peroxide and molybdenum. This flowing of the water in addition to the falling of the graphene onto the silicon oxide beneath is most likely the cause of the increased wrinkles [52]. The white dots are also less bright, indicating that it might have something to do with either the morphology of the graphene or an effect of the molybdenum.

Finally, Figure 4.19 shows the graphene sample after nanoparticle deposition had been performed on neighbouring strips and the sample subsequently underwent an annealing process. Comparison of the images indicates that the nanoparticle deposition and annealing procedures do not appear to introduce visible changes to the pristine graphene regions. In addition, the nanoparticle printing can be performed on selected areas without contaminating other devices.

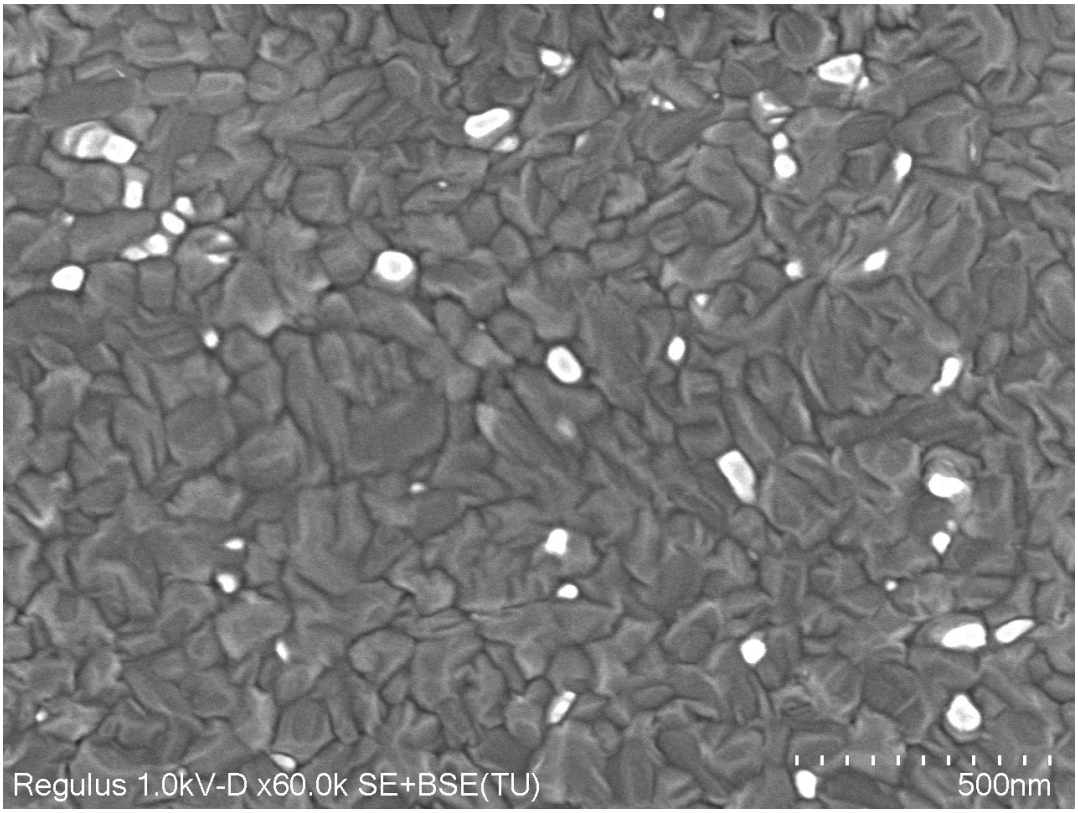

Figure 4.17: High-magnification SEM image of multilayer graphene with molybdenum underneath the graphene layer.

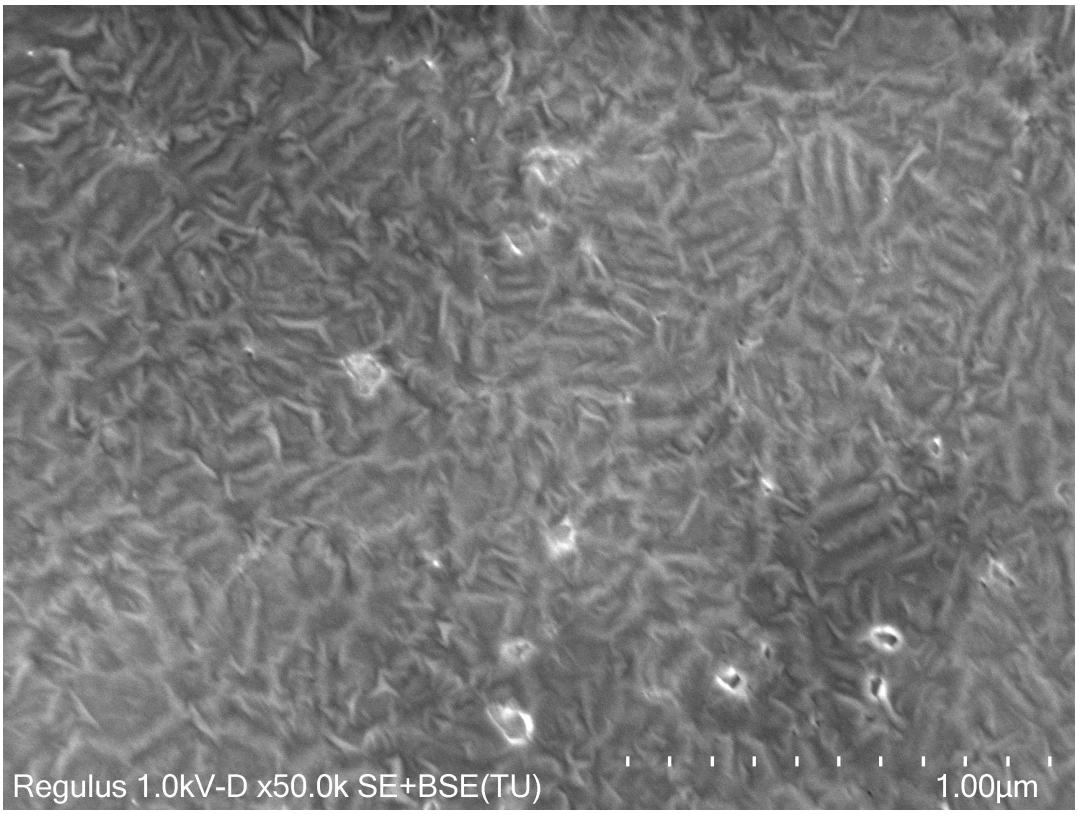

Figure 4.18: High-magnification SEM image of multilayer graphene after removal of the molybdenum substrate.

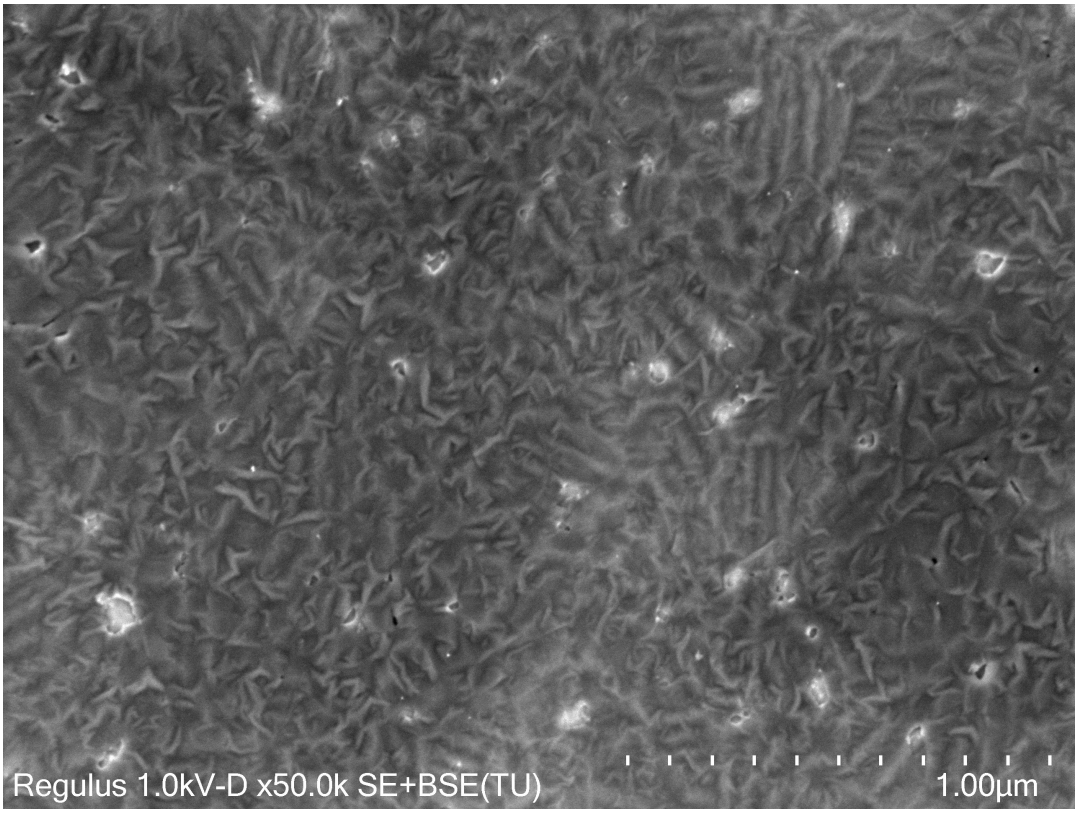

Figure 4.19: SEM image of pristine multilayer graphene after nanoparticle deposition on neighbouring strips and subsequent annealing of the sample.

4.3.1. Grapheana graphene

The commercially obtained Grapheana graphene exhibits a significantly smoother and more uniform surface morphology compared to the graphene fabricated in-house. This can be observed by comparing Figure 4.20 with the in-house processed graphene shown in Figure 4.19. In contrast to the in-house graphene, the Grapheana graphene does not exhibit pronounced wrinkles or ridge-like structures. The surface appears more smooth, indicating a less surface roughness. In addition, several small holes can be seen in the graphene layer, features which are not present in the in-house fabricated samples.

Small nanoparticles can also be observed on the graphene surface, despite these regions not being intentionally functionalized. This contamination might be introduced during the nanoparticle deposition process. Possible sources include residual nanoparticle transport caused by nozzle movement across the graphene strip during non-printing operations, or airborne nanoparticle contamination resulting from gas flow within the deposition chamber during printing on nearby regions. Alternatively, these particles may originate from residues or processing steps associated with the commercial graphene fabrication and transfer procedure used by Grapheana.

Furthermore, the Grapheana graphene does not exhibit the bright white surface features observed on the in-house fabricated graphene samples. Since the fabrication process used by Grapheana is proprietary, it is difficult to explain the cause of the differences in the graphene.

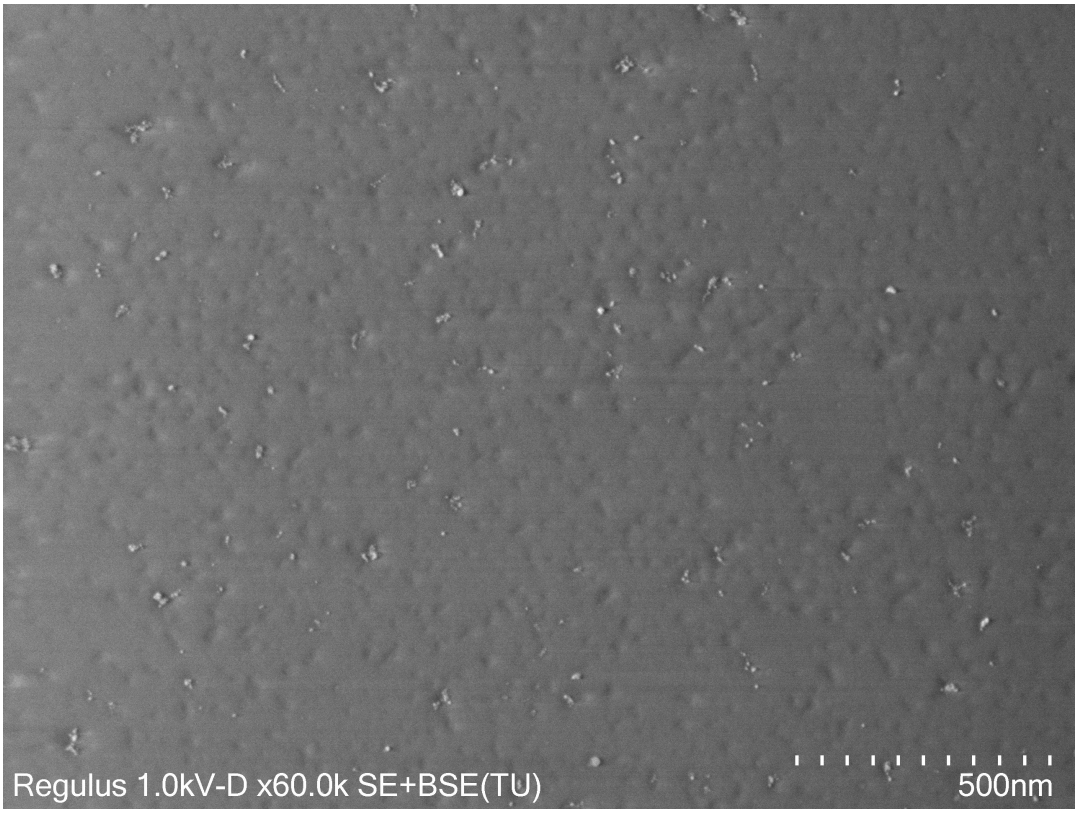

Figure 4.20: SEM image of Grapheana graphene at 60k magnification. Nanoparticle contamination from the functionalization process is visible (~ 0.3% area coverage).

4.4. Raman

Raman spectroscopy was used to characterize the quality of the graphene samples. A representative full Raman spectrum of a graphene sensor is shown in Figure 4.21. Several characteristic peaks can be identified within the spectrum, each providing specific information about the graphene material.

The peak located near 520 cm^{-1} and the increase in intensity at 930-100 cm^{-1} corresponds to the silicon that is underneath the graphene. The D, G and 2D peak can all be seen as expected and are marked with a circle.

All Raman spectra shown in the figures are examples of individual Raman measurements. Variations in the spectra were observed between different strips on the same sample, as well as between different measurement locations within a single strip. To obtain a more representative analysis of the graphene properties, multiple Raman measurements were performed for each sample. The extracted Raman parameters were subsequently averaged, and their corresponding standard deviations were calculated. The resulting mean values and standard deviations are summarized in Table 4.9.

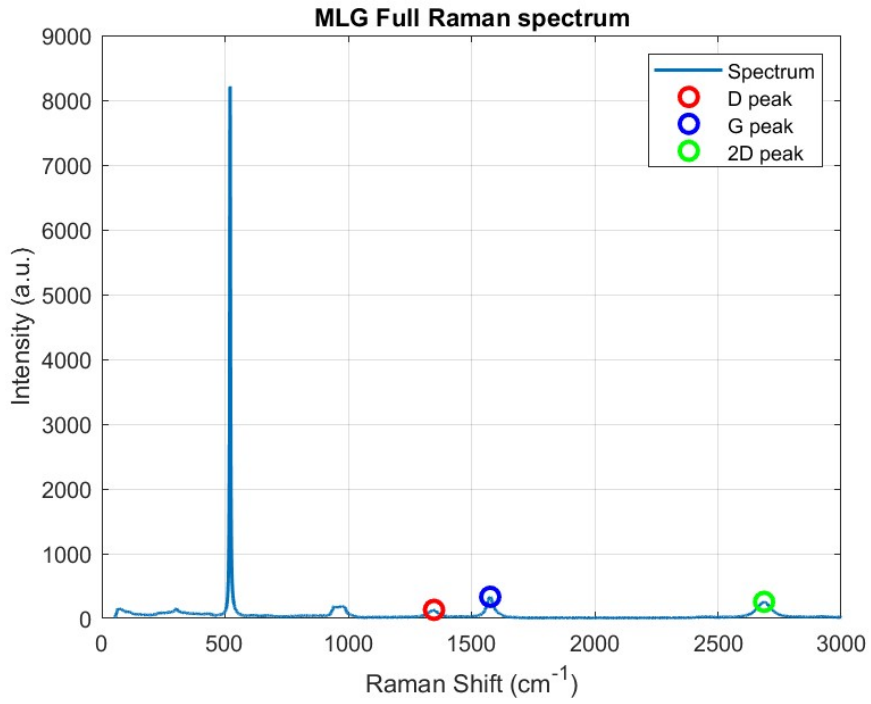

Figure 4.21: Example Raman spectrum from 0 to 3000 cm^{-1} of the fabricated graphene.

4.4.1. MLG

Before the molybdenum was etched away, the Raman spectrum of the graphene was strongly influenced by the underlying molybdenum layer. As a result the Raman spectra obtained before etching cannot give an accurate representation of the graphene quality.

As shown in Figure 4.22, the Raman quality metrics before etching are relatively poor, with a low I_{2D}/I_G ratio and a comparatively high I_D/I_G ratio. However, after removal of the molybdenum substrate, the Raman spectrum improves significantly, as shown in Figure 4.23. In addition, the I_{2D}/I_G ratio of around 0.8 confirms this to be multi-layer [46].

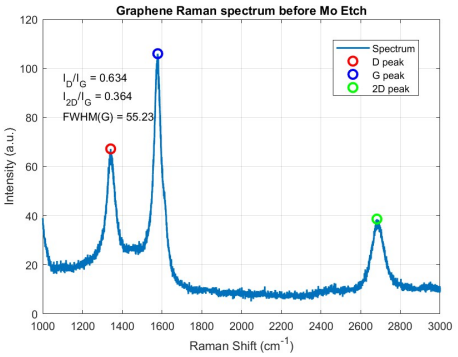

Figure 4.22: Example Raman spectrum of the fabricated multilayer graphene before molybdenum etching.

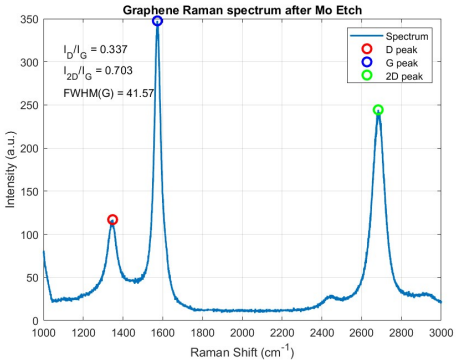

Figure 4.23: Example Raman spectrum of the fabricated multilayer graphene after molybdenum etching.

The influence of nanoparticle functionalization on the graphene Raman properties was also investigated. Figures 4.24 and 4.25 show Raman spectra of multilayer graphene functionalized with Palladium and Platinum nanoparticles, respectively.

The deposited nanoparticles appear to have only a limited influence on the Raman performance metrics of the graphene. Although slight changes in the peak ratios and peak widths can be observed, the

overall characteristics remain comparable to the pristine samples. A more extensive overview of all Raman measurements is summarized in Table 4.9.

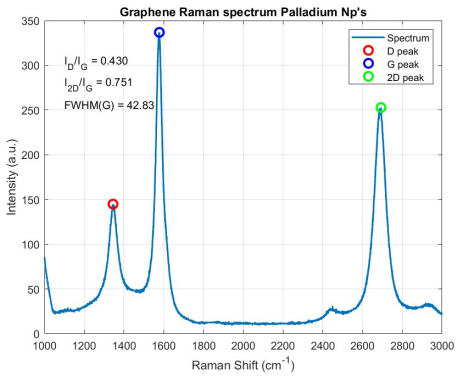

Figure 4.24: Example Raman spectrum of the fabricated multilayer graphene functionalized with Palladium nanoparticles.

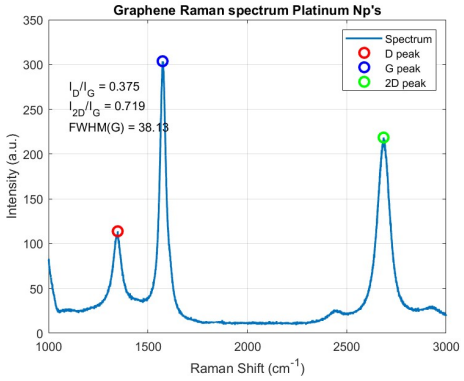

Figure 4.25: Example Raman spectrum of the fabricated multilayer graphene functionalized with Platinum nanoparticles.

4.4.2. Grapheana

The Raman spectra obtained from the Grapheana samples are expected to be of higher quality graphene. As shown in Figure 4.26, the measured I_{2D}/I_G ratios are around 1 indicating that it is FLG [46]. For the Palladium-functionalized graphene shown in Figure 4.27, the reduced I_{2D}/I_G ratio can be explained by the influence of the deposited nanoparticles.

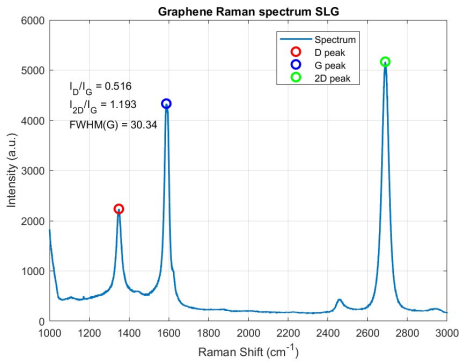

Figure 4.26: Example Raman spectrum of the Grapheana sample.

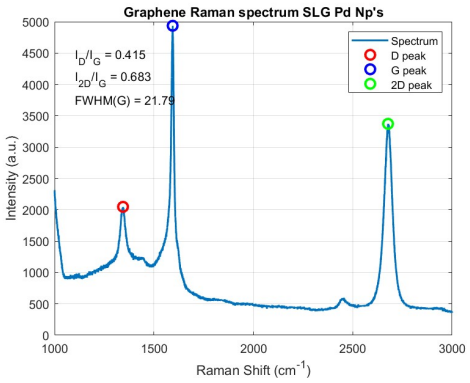

Figure 4.27: Example Raman spectrum of the Grapheana sample functionalized with Palladium nanoparticles.

4.4.3. Summary

A summary of the extracted Raman parameters for all measured samples is provided in Table 4.9. Overall, the multilayer graphene samples after molybdenum etching exhibited Raman characteristics that are consistent with values for MLG graphene obtained by colleagues. Functionalization with Palladium and Platinum nanoparticles resulted in only moderate changes to the Raman metrics, suggesting that the graphene structure remained largely intact after nanoparticle deposition.

The Grapheana graphene shows a higher I_{2D}/I_G ratios indicating that the graphene may be of fewer layers than the graphene that was fabricated in-house. In addition, the I_D/I_G ratio is higher than the MLG however the FWHM(G) and FWHM(D) are two times as low. This is surprising as they all give an indication about the defects in the graphene [45]. Also, the standard deviation in the measurements is higher than the in-house graphene indicating that there is more variation on and between the graphene strips.

Table 4.9: Summary of the Raman spectroscopy results for graphene samples.

Sample	N	Mean I_D/I_G	S.D. I_D/I_G	Mean I_{2D}/I_G	S.D. I_{2D}/I_G	Mean FWHM(G) (cm^{-1})	S.D. FWHM(G) (cm^{-1})	Mean FWHM(D) (cm^{-1})	S.D. FWHM(D) (cm^{-1})
MLG	4	0.329	0.025	0.847	0.114	40.68	1.673	81.99	4.64
MLG Before Mo Etch	4	0.584	0.125	0.340	0.0845	42.29	8.92	65.56	15.01
MLG Pd	5	0.471	0.031	0.911	0.233	39.68	7.341	68.42	7.32
MLG Pt	5	0.337	0.061	0.746	0.148	37.09	1.80	74.24	12.67
Graphaena	4	0.442	0.066	0.933	0.234	19.45	8.540	31.91	10.01

4.5. Sheet resistance measurements

To enable comparison between graphene devices with different geometries, the sheet resistance was calculated from the measured electrical resistance values. Since the fabricated devices have varying widths and lengths, the sheet resistance provides a geometry independent resistance.

The sheet resistance was calculated using the following formula:

$$R_{\square} = R\frac{W}{L} \tag{4.1}$$

where $R_{\square}$ is the sheet resistance, R is the measured resistance, W is the width and L the length of the graphene strip.

Table 4.10 summarizes the measured sheet resistances for the different graphene samples. Most measured sheet resistance values are in the range of 1 k$\Omega/\square$, which is consistent with values previously reported by colleagues [53].

Table 4.10: Summary of the measured sheet resistances for the different graphene samples.

Sample	N	Mean sheet resistance ($\Omega/\square$)	S.D. ($\Omega/\square$)
MLG Pristine	6	869.7	17.8
MLG Pristine Before Mo Etch	9	17.2	25.8
MLG Pd Functionalized	6	1097.3	4.9
MLG Pt Functionalized	6	1202.1	2.98
MLG Au Functionalized	3	868.7	0.23
Grapheana	9	839.9	26.8

As can also be observed, functionalization of the graphene with nanoparticles results in an increase of resistance. The strength of this effect is different depending on the type of nanoparticle, even with similar area coverage. Platinum and palladium functionalized samples showed large increases while gold did not increase as much. The increase in resistance might be caused by the electronic functionalization of the nanoparticles. Charge was transferred due to the differing work function of graphene and the nanoparticle. These changed the local carrier concentration in the graphene resulting in a lower carrier mobility [28]. The differences of effect of the nanoparticles can be attributed to the different work functions as gold has the lowest work function and platinum the highest (ϕ_{Au} = 5.10–5.4 eV, ϕ_{Pd} = 5.2–5.6 eV, ϕ_{Pt} = 5.6-5.9 eV [54]). The same correlation can be seen in the resistance measurements.

In addition, the graphene samples measured prior to molybdenum removal exhibit a significantly lower resistance compared to the samples after the molybdenum had been etched away. This can be explained by the high conductivity of molybdenum due to being a metal, which provides an additional conductive pathway parallel to the graphene layer. As a result, the measured resistance of is much lower than that of the isolated graphene.

Finally, the commercially obtained Grapheana graphene exhibits a lower resistance than the in-house fabricated graphene samples. One possible explanation is a difference in graphene thickness, since thicker multilayer graphene generally exhibits lower sheet resistance. However, this interpretation appears inconsistent with the Raman measurements presented in Table 4.9, where the higher $\frac{I_{2D}}{I_G}$ ratio observed for the Grapheana samples suggests a lower number of graphene layers. It is therefore more likely that the Grapheana graphene possesses a higher conductivity than the in-house fabricated graphene. This may indicate a lower defect density or fewer wrinkles, since defects and wrinkles are known to decrease carrier mobility [55, 56].

4.6. Conclusion

Nanoparticles could be successfully deposited with controlled area coverage using the VSParticle system. The resulting nanoparticle density was found to depend strongly on the selected printing parameters, such as printing speed and spark current. Furthermore, annealing of the deposited nanoparticles caused a reduction in area coverage due to nanoparticle sintering and agglomeration, with the strength of this reduction depending on the annealing temperature and duration.

Using the developed fabrication process, graphene strips were successfully fabricated, as confirmed by both SEM imaging and Raman spectroscopy measurements. In addition, the commercially obtained Grapheana samples were verified to contain graphene. The Raman characterization of the in-house fabricated graphene samples showed performance metrics comparable to those reported previously by colleagues working with similar fabrication methods. In addition, the Grapheana samples showed only slightly better metrics than the in-house fabricated.

After nanoparticle functionalization, no major shifts or degradation were observed in the Raman spectra, indicating that the deposition process introduced only limited damage to the graphene structure. This suggests that the nanoparticles were successfully deposited and bonded to the graphene surface while preserving the structural integrity of the graphene.

Overall, graphene gas sensor devices functionalized with nanoparticles were successfully fabricated and characterized, and the obtained results demonstrate that the produced devices are of sufficient quality for subsequent gas sensing experiments.

5

Gas sensing results

In this chapter, the gas sensing measurements performed on the fabricated graphene devices are presented and discussed. The chapter begins the description of the measurement procedure followed by the sensing results for ethylene. The effects of the strength of the gas flow is also explored. Afterwards, additional gas sensing experiments are presented for several other gases, including nitrogen dioxide (NO2), ammonia (NH3), acetic acid, humidity, and carbon dioxide (CO2).

5.1. Procedure

Before each gas sensing measurement, samples that had previously undergone testing were first subjected to a cleaning procedure to remove adsorbed contaminants from the graphene surface. During this process, the sample was heated to 140 °C while continuously exposed to a nitrogen flow for approximately 30 minutes.

After the cleaning step, the sample was allowed to cool down to room temperature and was subsequently kept in ambient air for approximately 15 minutes to stabilize before the measurement sequence began. To allow for the measurement of the resistance of the graphene sensors, contact pins were placed on the gold contact pads located at the edges of the samples. These pins were connected through a breakout board to an Agilent 34970A data acquisition system equipped with a 34901A multiplexer module, allowing multiple graphene strips to be measured sequentially. The resistance of the sensors was measured using a dual-channel Keithley 2612B Source Measure Unit (SMU). Both the multiplexer and the SMU were controlled using a LabVIEW script, allowing automated measurements of multiple sensors.

The measurement itself started with an initial stabilization period, typically lasting around 1.5 hours depending on the available time. The stabilization period is required for the sensors to have a stable resistance before a target gas is introduced. If the resistance of the sensors is unstable while introducing a gas it can be unclear if the change in resistance is due to the gas, or it's instability. The time of 1.5 hours was found to be a good length for the sensors to be stable during early testing.

Following stabilization, the target gas was introduced into the sensing chamber in repeated on/off cycles. The duration and number of these cycles were selected based on the expected response and recovery times, as well as the practical time available for the experiment.

The upcoming figures show the responses of the different sensors in different tests. All sensor responses shown within a single graph originate from measurements performed on the same sample during a single experimental run. This results in accurate comparison between the sensors, since the measurement conditions remain identical and stable throughout the test.

5.2. Ethylene tests

Since ethylene is an electron accepting (oxidizing) gas, and the graphene sensors are p-type, the expected sensing response is a decrease in resistance upon exposure to ethylene. The ethylene measurements in

this work were performed using a large permeation tube with a permeation rate of 1171 ng/min, as specified by VICI Metronics.

The first measurement was performed on in-house graphene with one side functionalized with Palladium nanoparticles while the other side was kept pristine. The resulting response to 20 ppm ethylene is shown in Figure 5.1. Although the resistance did decrease when the gas was on, from this measurement it could not be determined that ethylene was successfully sensed. Two issues complicate the interpretation of the data. First, the data exhibited a high level of noise. This noise may have originated from bad contact of the pins to the pads of the sample. If the pins are not tightened enough or close to the edge of the pad, small movements might cause variation in the contact resistance between the pin and the pad. This might result in changes in resistance that looks like noise. Second, the stabilization period prior to gas exposure was limited to approximately 40 minutes, which may not have been enough to stabilize the sensor. It is thereby unsure if the reduction of resistance is due to ethylene or drift from the sensor. Consequently, the observed resistance decrease cannot confidently be attributed solely to ethylene exposure.

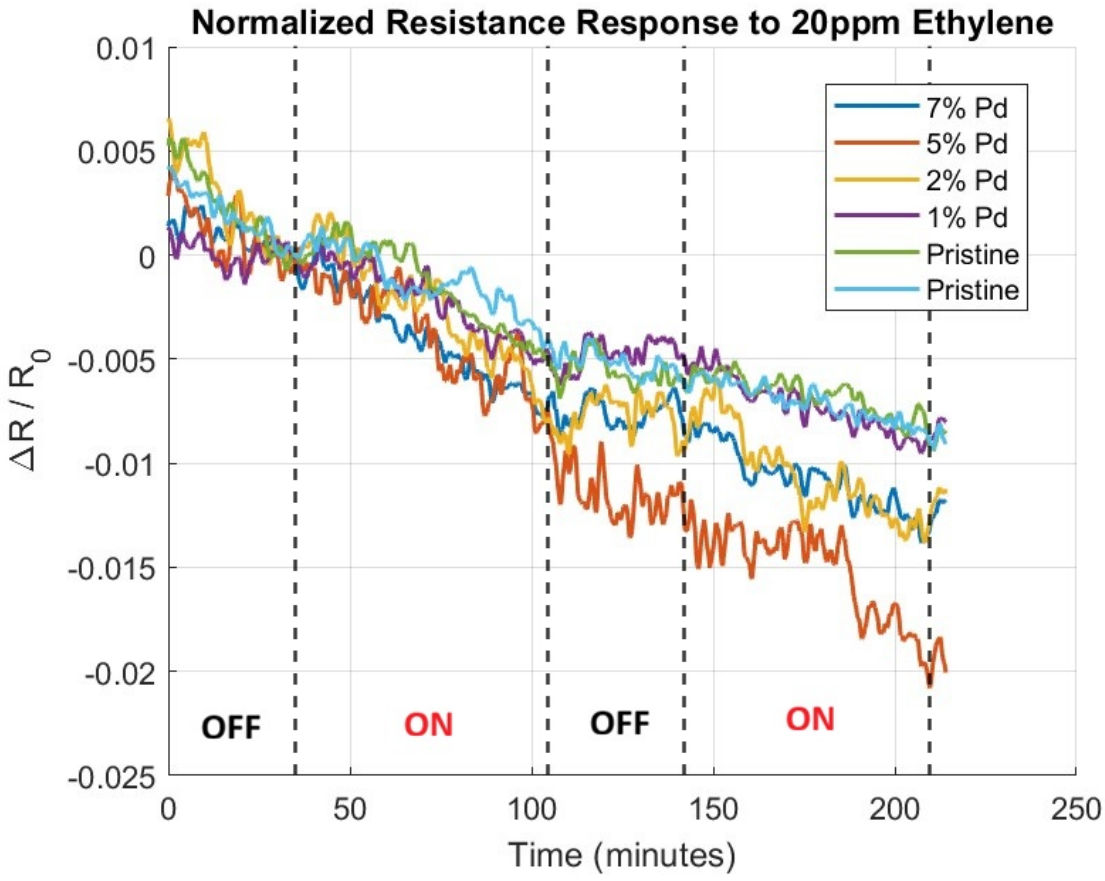

Figure 5.1: MLG decorated with Palladium np's response to 20ppm Ethylene at Room Temperature and 0 RH. The flow to the sample equals 50 sscm.

To establish a baseline reference, measurements were subsequently performed on a pristine graphene sample without nanoparticle functionalization. The response is shown in Figure 5.2. Unexpectantly, the observed response differed from expectations. Instead of decreasing, the resistance increased during ethylene exposure. This behaviour contradicts both the expected response for p-type graphene exposed to an electron accepting gas and observations reported in previous studies.

One possible explanation is that the sensing chamber still contained residual contamination or interfering gases during the measurement. However, this explanation appears unlikely, since the setup had been allowed to stabilize and clean for approximately two hours prior to the gas exposure.

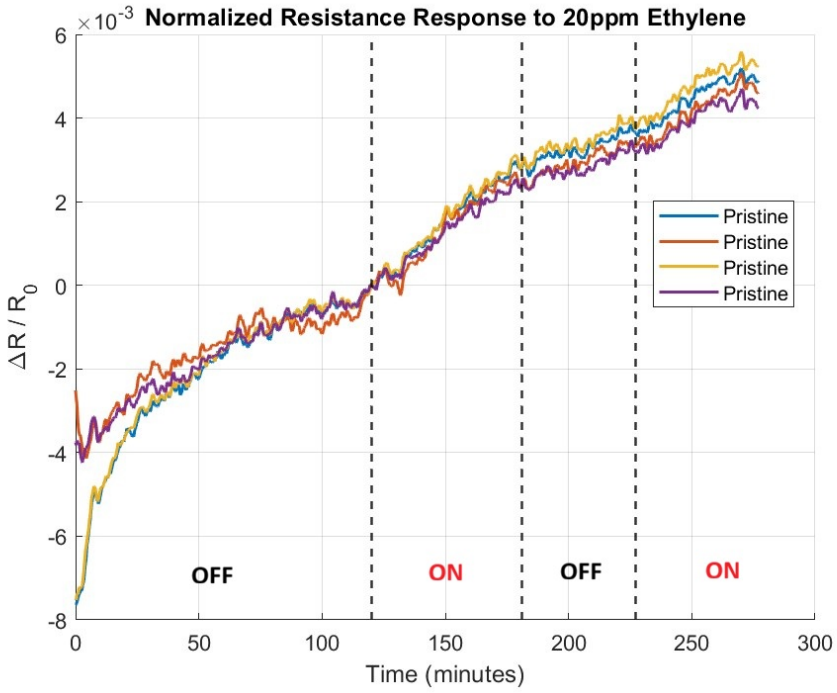

Figure 5.2: MLG response to 20ppm Ethylene at Room Temperature and 0 RH. The flow to the sample equals 50 sscm.

To verify whether the pristine graphene sample was functioning correctly, a measurement using NO2 was performed. NO2 like ethylene is an electron accepting gas and a reduction in resistance is anticipated. As shown in Figure 5.3, when the NO2 is blown onto the sample the resistance goes down as was expected. Like ethylene NO2 is electron donating[8] and with the p-type graphene would result in a lower resistance when in contact. This confirms that the graphene device itself was operational and capable of gas sensing.

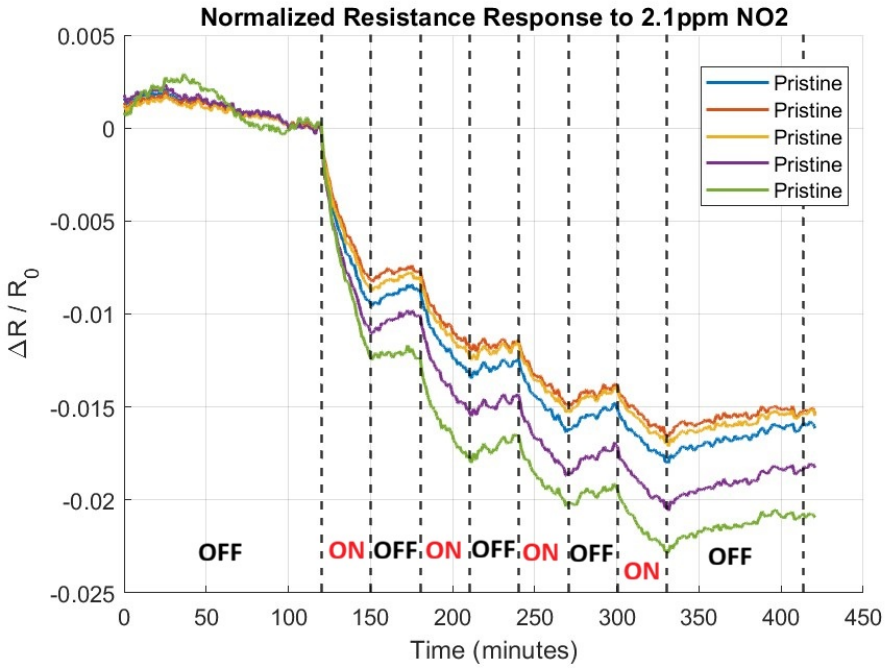

Figure 5.3: MLG response to 2.1ppm NO2 at Room Temperature and 0 RH. The flow to the sample equals 250 sscm.

To further investigate whether ethylene could be detected reliably, measurements were performed on the commercially obtained Grapheana graphene sample. The results are shown in Figure 5.4. The response follows the expected behaviour. Upon ethylene exposure, the resistance of the graphene decreases. In addition, when the gas is turned off the resistance stops dropping and there is a small recovery.

Two distinct speeds of response can be observed in the measurement. The first is a fast resistance decrease of approximately 0.25% occurring within the 5 minutes after gas exposure. The second is a slower response that continues for more than one hour. The rapid initial response is likely caused by the manual valve switching used due to piping of the large permeation tube setup. Since the large permeation tube is not connected to an exhaust line, ethylene can slowly permeate into the tubing even while the valves remain closed. As a result, ethylene accumulates inside the gas lines. Once the valves are opened, a temporary high-concentration ethylene pulse reaches the sample, causing the fast initial resistance change. The slower response that follows is believed to represent the actual steady-state sensor response.

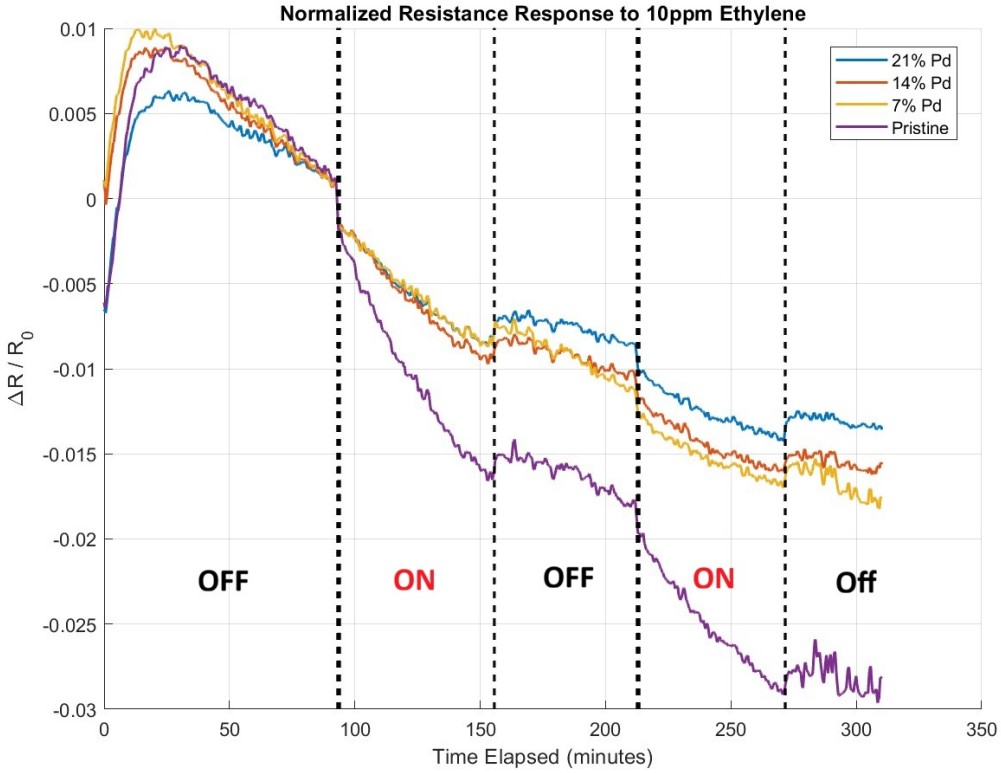

Figure 5.4: SLG decorated with Palladium np's response to 10ppm Ethylene at Room Temperature and 0 RH. The flow to the sample equals 100 sscm.

Another observation from Figure 5.4 is the poor recovery of the sensor after ethylene exposure. One possible explanation is that oxygen species desorb from the graphene surface during exposure and are not replenished because nitrogen is used as the carrier gas [9]. Another possibility is that ethylene molecules bind strongly to high-energy adsorption sites on the graphene or nanoparticles, requiring higher temperatures or UV light for complete desorption [21]. As expected, the second exposure cycle exhibits a smaller response than the first, likely due to incomplete recovery between cycles.

Unexpectedly, the graphene samples functionalized with Palladium nanoparticles performed worse than the pristine graphene samples. This suggests that the expected catalytic effect of Palladium did not occur under the measurement conditions. Several explanations are possible. The measurement temperature may have been too low to activate catalytic interactions between ethylene and the Palladium nanoparticles [27, 34]. Additionally, the absence of humidity may have influenced the sensing mechanism. Another

possibility is that the functionalization process damaged the graphene outweighing any catalytic benefits. However, this interpretation appears to conflict with the Raman characterization results presented in Chapter 4, where only limited damage from the nanoparticle deposition process was observed. In addition to the reduced sensitivity, the recovery behaviour of the Palladium-functionalized devices also did not improve compared to pristine graphene.

To further investigate the effects of temperature and humidity, a measurement was performed at elevated temperature. The results are shown in Figure 5.5. During this experiment, the stabilization and first exposure cycle was performed at 40% RH, while the second cycle was measured under dry conditions. The sensor temperature was maintained at 120 ℃.

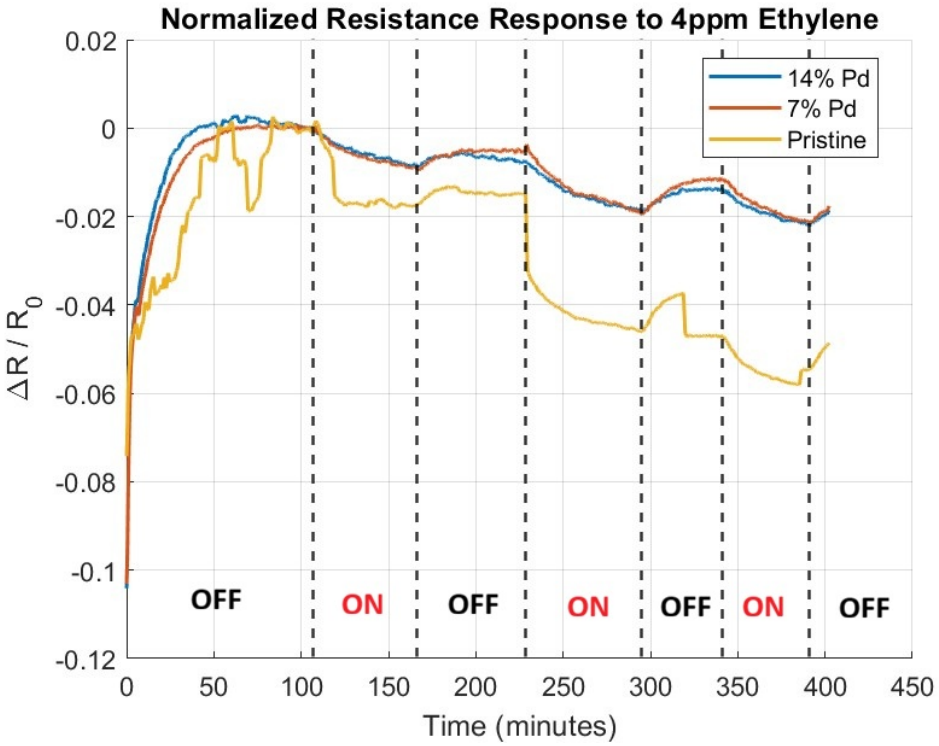

Figure 5.5: SLG decorated with Palladium np's response to 4ppm Ethylene at 120°C and 40% during stabilization and the first cycle and 0 RH for the second cycle. The flow to the sample equals 245 sscm for the first cycle and 150 for the next.

The measurements indicate that the addition of humidity negatively affected the ethylene response, since the dry measurement cycle produced a stronger response than the humid cycle. Several additional observations can be made. First, the recovery at elevated temperature is significantly improved compared to room temperature measurements, suggesting higher temperatures assist the desorption of ethylene molecules. Second, even at elevated temperature, the pristine graphene continued to outperform the Palladium-functionalized graphene, particularly during the second measurement cycle. Although the Palladium-functionalized devices had relatively improved recovery behaviour, the absolute response magnitude remained smaller than that of pristine graphene. These results suggest that even higher operating temperatures may be required to achieve a complete recovery. Unfortunately, the experimental setup and the samples used in this work did not allow for measurements at higher temperatures.

Figure 5.6 shows the response of the in-house graphene devices to humidity exposure. Increasing humidity caused an increase in resistance for both pristine and Palladium-functionalized graphene. Interestingly, once dry air was flown back in, the pristine graphene exhibited partial recovery, whereas the palladium showed no recovery and did not even stop increasing in resistance. One possible explanation is that the Palladium nanoparticles promote local water adsorption or condensation, causing water molecules to remain attached to the surface for a longer period of time [57, 58].

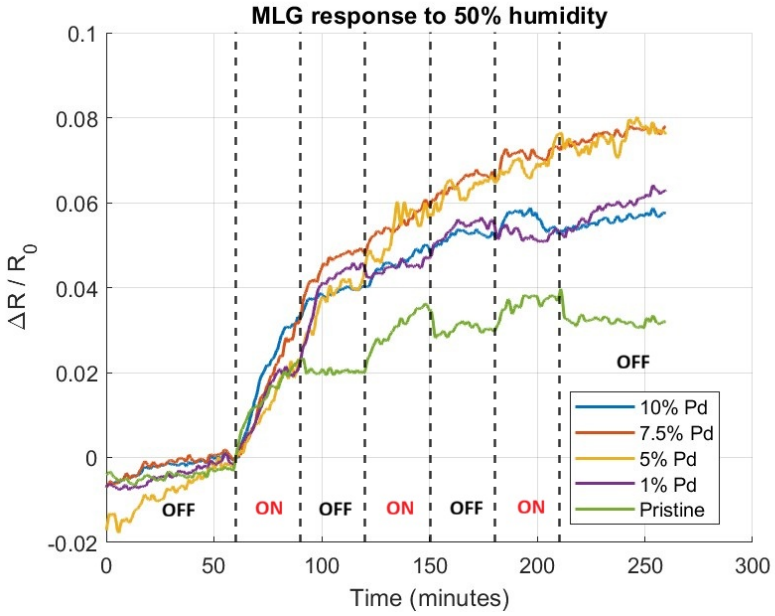

Figure 5.6: MLG decorated with Palladium np's response to 50%RH at Room Temperature. The flow to the sample equals 300 sscm.

Since Palladium functionalization did not improve the sensing response, platinum (Pt) and tin oxide (SnO) nanoparticle functionalizations were also investigated. Figure 5.7 shows the response of platinum functionalized graphene to ethylene exposure. Similar to the Grapheana measurements, the resistance decreases upon exposure to ethylene, which corresponds to the expected sensing behaviour. However, once again, the pristine graphene exhibited a greater response than the platinum functionalized graphene, while the recovery remained limited. Nevertheless, this measurement confirms that ethylene sensing using the in-house fabricated graphene devices is possible.

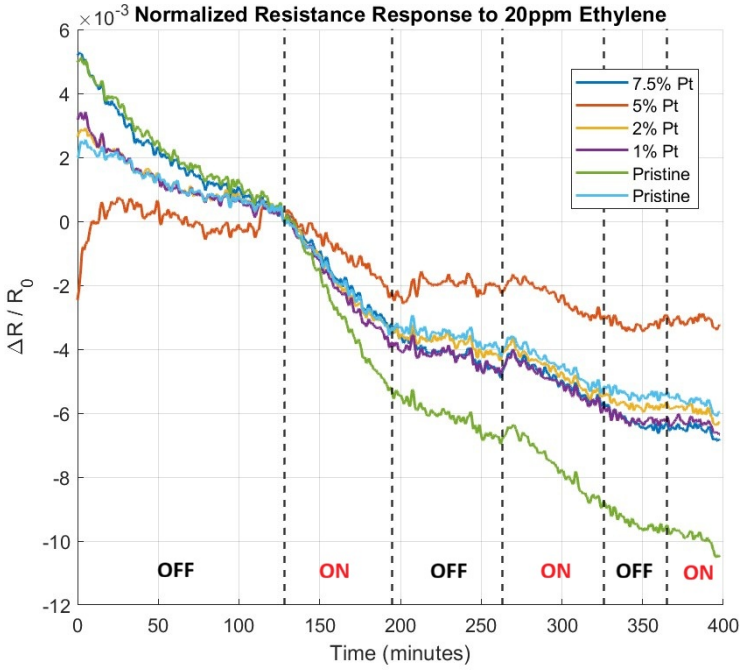

Figure 5.7: MLG decorated with Platinum np's response to 20ppm Ethylene at Room Temperature and 0 RH. The flow to the sample equals 50 sscm.

Finally, the response of SnO functionalized graphene to 10 ppm ethylene is shown in Figure 5.8. Surprisingly, almost no response to ethylene was observed, even for the pristine graphene strips included in the measurement. Additional control measurements confirmed that the device remained capable of sensing other gases such as NO2 and ammonia, indicating that the sensor itself was functioning correctly. The reason for the absence of an ethylene response during this measurement remains unclear.

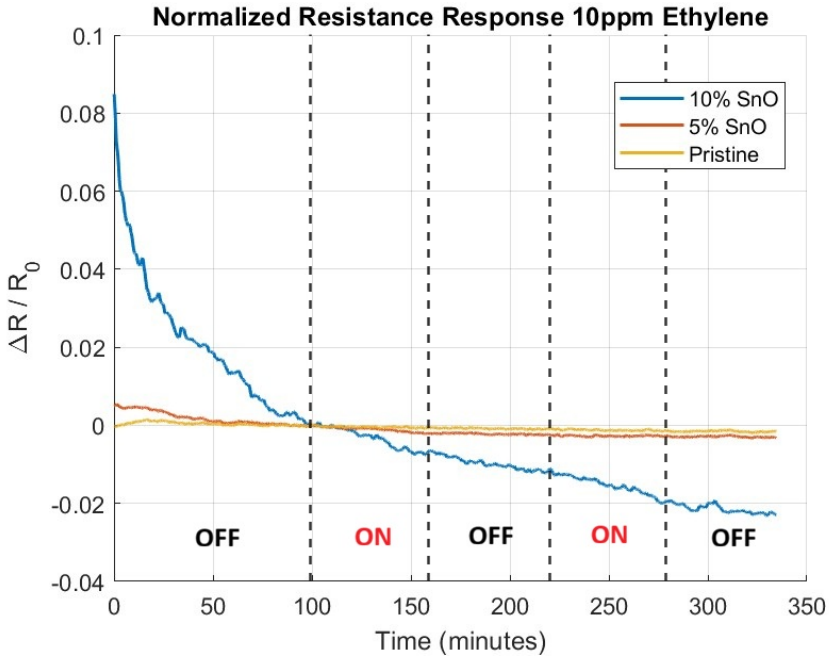

Figure 5.8: MLG decorated with tin-oxide np's response to 10ppm Ethylene at Room Temperature and 0 RH. The flow to the sample equals 100 sscm.

5.2.1. Effects of flow

Additional experiments were performed to investigate the influence of gas flow rate on the sensing response of the graphene devices. These measurements were primarily carried out using the Grapheana graphene samples in order to determine whether the sensor response was dominated by gas concentration, gas flow, or a combination of both effects.

In Figure 5.9, the graphene sensor was exposed to a higher ethylene concentration of 20 ppm, while the gas flow rate was reduced to 50 sccm. If the gas flow rate did not significantly influence the sensing behaviour, the expectation would be that the sensor response should be greater than the response observed in Figure 5.4. In that test a lower concentration, but higher flow rate was used. Ideally, the response would approximately double due to the doubled ethylene concentration.

However, as shown in Figure 5.9, the opposite trend is observed. The higher ethylene concentration combined with a lower gas flow rate produces a weaker sensor response than the lower concentration combined with a higher flow rate. This indicates that the gas flow rate has a strong influence on the sensor response.

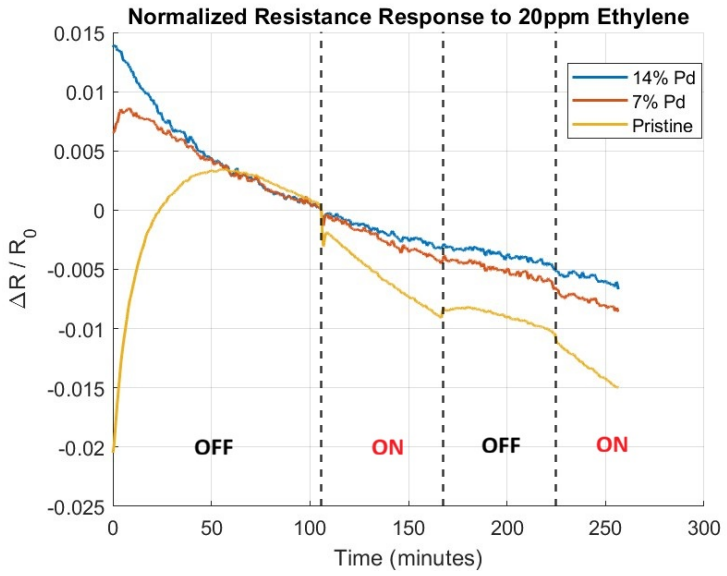

Figure 5.9: SLG decorated with Palladium np's response to 20ppm Ethylene at Room Temperature and 0 RH. The flow to the sample equals 50 sscm.

To further investigate the influence of flow rate, an additional measurement was performed using a lower ethylene concentration of 5 ppm combined with a higher gas flow rate of 200 sccm. The result is shown in Figure 5.10.

For the pristine graphene sample, no clear long-term sensor response could be observed apart from a short transient signal caused by manual valve switching. The palladium functionalized graphene did exhibit a response, although weaker than the response obtained during the 10 ppm measurement shown in Figure 5.4. However, despite the lower ethylene concentration, the response remained stronger than the response measured for the 20 ppm experiment performed at the lower flow rate of 50 sccm. These results further support the conclusion that insufficient gas flow significantly reduces the effective sensor response.

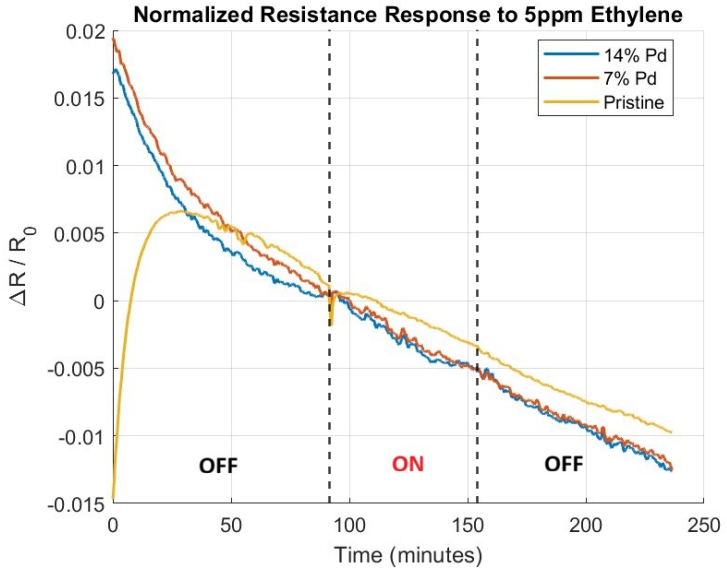

Figure 5.10: SLG decorated with Palladium np's response to 5ppm Ethylene at Room Temperature and 0 RH. The flow to the sample equals 200 sscm.

To further verify the influence of flow rate, a measurement was performed using NO2 on the in-house fabricated graphene devices. The same NO2 concentration as used in Figure 5.3 was applied, but the gas flow rate was reduced from 250 sccm to 50 sccm. The resulting response is shown in Figure 5.11. In addition, a summary of the different flow experiments can be found in Table 5.1

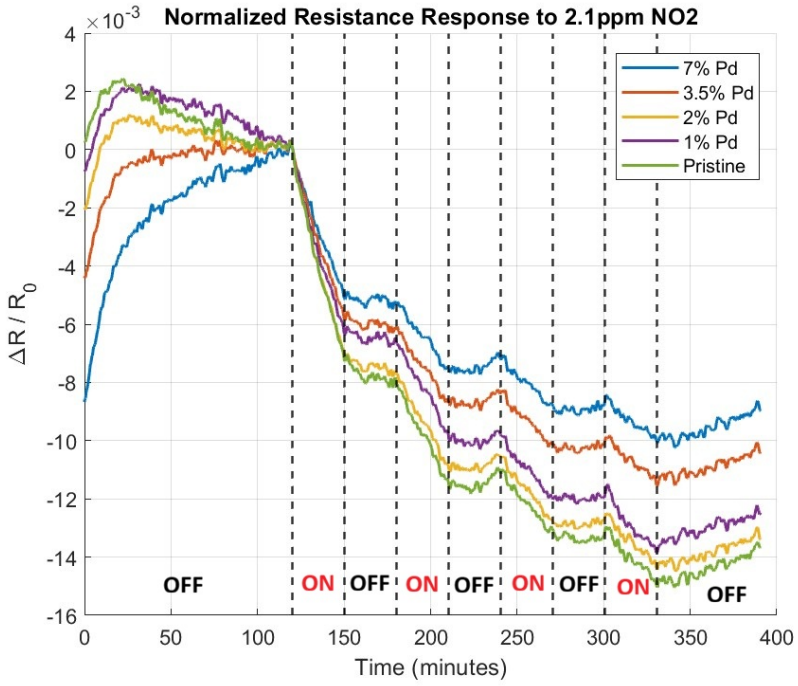

Figure 5.11: MLG decorated with Palladium np's response to 2.1ppm NO2 at Room Temperature and 0 RH. The flow to the sample equals 50 sscm.

Table 5.1: Summary table of the highest responses in the flow experiments

Gas and coverage	Low flow response (%)	Medium flow response (%)	High flow response (%)
Ethylene (Pd 7%)	0.5 (50 sscm and 20 ppm)	0.9 (100 sscm and 10ppm)	0.5 (200 sscm and 5 ppm
Ethylene (Pristine)	0.9 (50 sscm and 20 ppm)	1.6 (100 sscm and 10ppm)	-
NO2 (Pristine)	0.8 (50 sscm 2.1 ppm)	-	1.25 (250 sscm 2.1 ppm)

As expected, a lower flow rate resulted in a significantly weaker sensor response. In the case of NO2 even the strongest response observed at low flow did not exceed any response measured under high-flow conditions. From this it can be concluded that insufficient gas flow can substantially reduce the effective sensitivity of the graphene sensor.

The physical explanation might be that the flow from the showerhead goes directly to the exhaust and parts of it do not reach the sample. Future research can be done by putting the showerhead at various distances to the sample to measure the differences.

Another possible explanation is that the molecules in the vicinity of the graphene surface become depleted due to adsorption onto the sensor [59]. At low gas flow rates, this can result in a locally depleted region that replenishes too slowly, since fewer new gas molecules are transported toward the sensing surface [60]. As a result, the effective concentration at the graphene surface may be lower than the concentration blown into the chamber. This reduced concentration at the surface of the graphene due to a low flow rate can consequently lead to a lower sensor response.

5.3. Cross-sensitivity measurements

To investigate whether nanoparticle functionalization could enhance the sensitivity of graphene toward gases other than ethylene, several cross-sensitivity measurements were performed using different target gases. The objective of these experiments was as following. First, to see if the deposited nanoparticles can improve the sensing response, and second, to calculate the selectivity of the samples towards ethylene.

The first measurement involved acetic acid, and the result is shown in Figure 5.12. Acetic acid is an electron accepting gas and, similarly to ethylene, plays a role in biological growth and ripening processes. As shown in the figure, the Grapheana graphene functionalized with palladium nanoparticles exhibited a measurable response to acetic acid exposure. However, due to instability in the signal from the pristine graphene strip, it is difficult to determine whether the palladium nanoparticles provided a catalytic enhancement. Another notable observation is the absence of recovery after the gas exposure was stopped. This suggests that acetic acid molecules form relatively strong bonds with either the graphene surface or the palladium nanoparticles, resulting in slow or no desorption at room temperature.

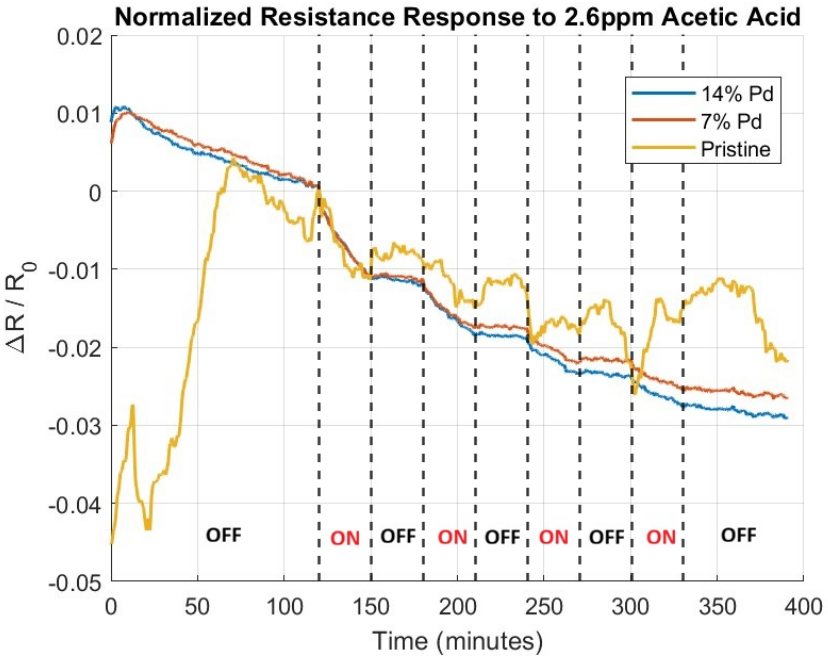

Figure 5.12: SLG decorated with Palladium np's response to 2.6ppm Acetic Acid at Room Temperature and 40% RH. The flow to the sample equals 250 sscm.

Next, nitrogen dioxide (NO2) measurements were performed. NO2 is a strong electron accepting gas and is well known to interact strongly with graphene. The result is shown in Figure 5.13. As expected for p-type graphene, exposure to NO2 resulted in a decrease in resistance. Even under humid conditions (40% RH), the sensor response remained clear and stable, indicating that the graphene devices retained good sensitivity towards NO2 in the presence of water vapor.

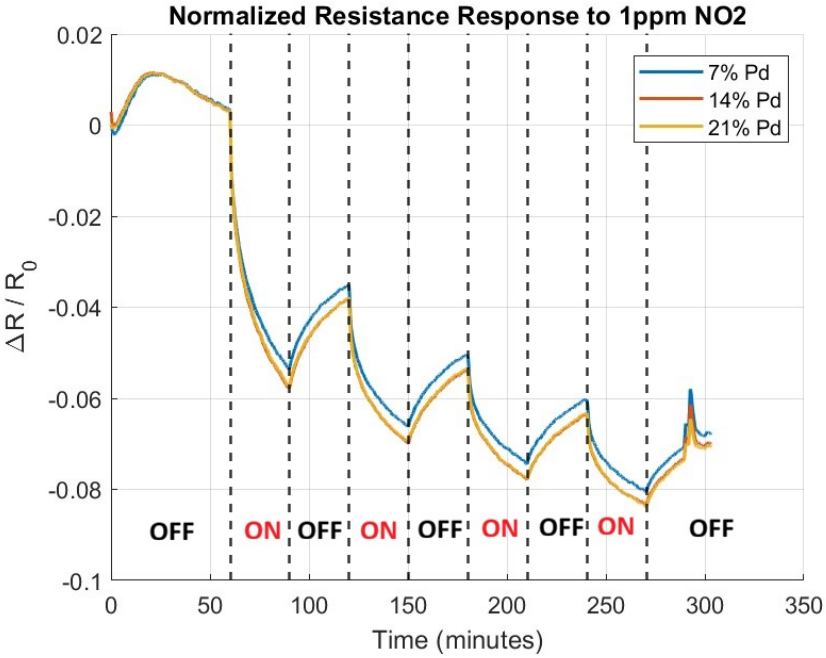

Figure 5.13: SLG decorated with Palladium np's response to 1ppm NO2 at Room Temperature and 40% RH. The flow to the sample equals 410 sscm.

Ammonia (NH3) measurements were also conducted, as shown in Figure 5.14. In contrast to NO2, ammonia is an electron-donating gas. Therefore, for p-type graphene, the expected response is an increase in resistance. The measured response follows this expected behaviour. Unfortunately, the signal from the pristine graphene strip was corrupted during the experiment, preventing a direct comparison between pristine and functionalized graphene. The most likely causes of this corrupted data are unstable probe pin contacts or instability in the electrical connections between the pinout board and the measurement setup.

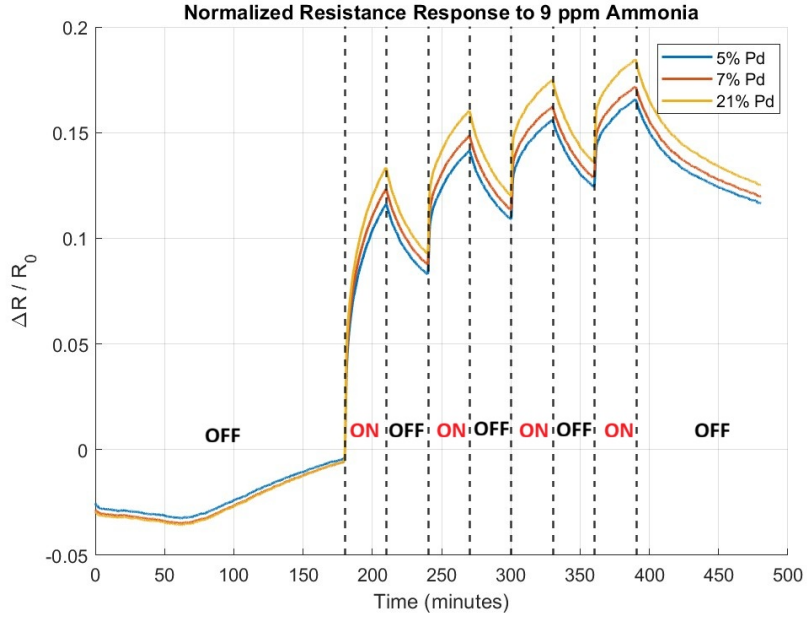

Figure 5.14: SLG decorated with Palladium np's response to 9ppm NH3 at Room Temperature and 40% RH. The flow to the sample equals 500 sscm.

Figure 5.15 shows the response of graphene functionalized with tin oxide nanoparticles to NO2. The measurements indicate that the functionalized devices have responses comparable to the pristine graphene devices in terms of sensitivity.

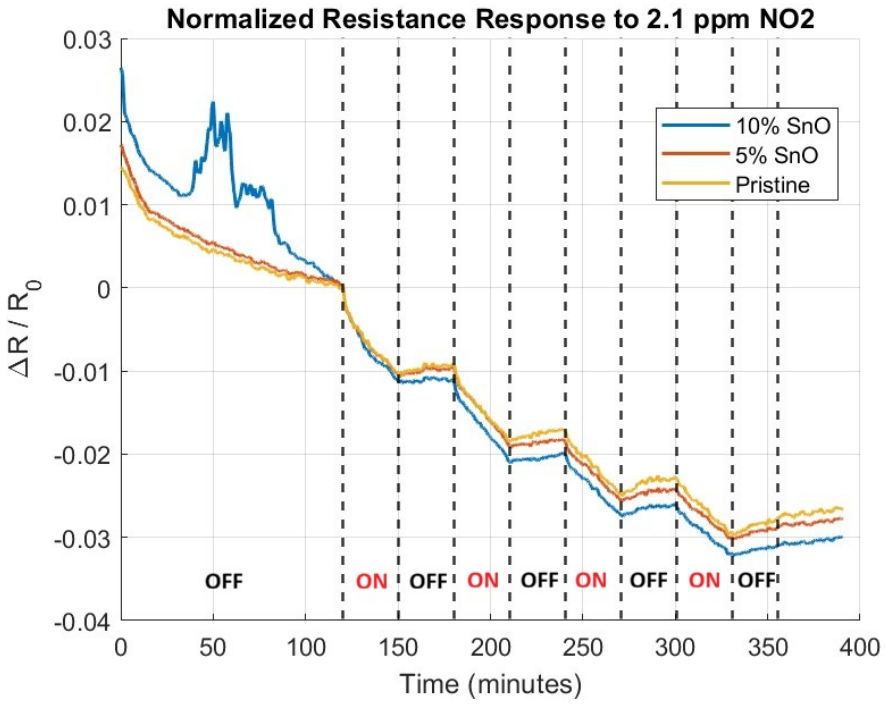

Figure 5.15: MLG decorated with Tinoxide np's response to 2.1ppm NO2 at Room Temperature and 0% RH. The flow to the sample equals 250 sscm.

The response of the tin oxide functionalized graphene sensors to ammonia was also investigated, with the first measurement shown in Figure 5.16. Several of the graphene devices were corrupted during the experiment, resulting in only two out of the four sensors providing readable data. In addition, the device with 5% nanoparticle area coverage exhibited unstable behaviour, characterized by irregular jumps in resistance throughout the measurement. Although the device with 10% coverage also showed fluctuations during the stabilization period, its response became considerably more stable during gas exposure.

The measured response of the 10% functionalized device was approximately 4%, with a recovery of around 20%. However, because the pristine graphene reference devices were corrupted and could not be measured reliably, it is difficult to determine whether the tin oxide functionalization improved the sensing performance compared to pristine graphene.

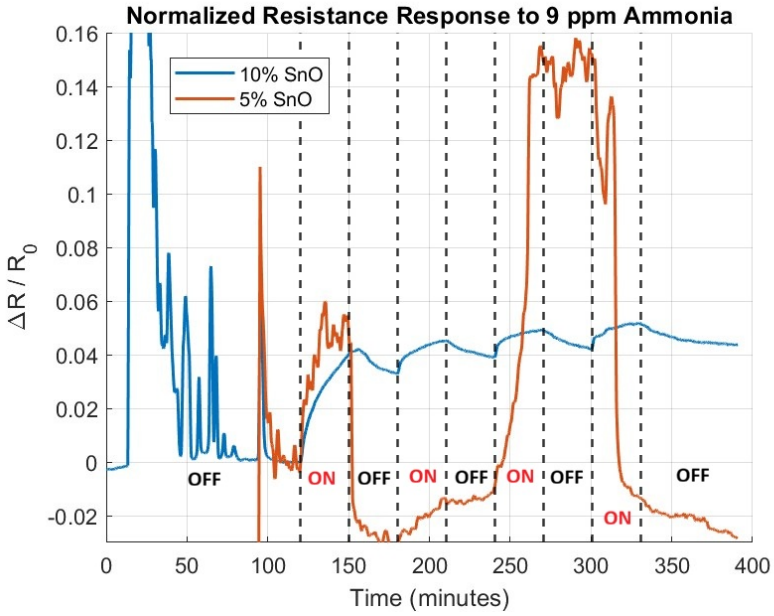

Figure 5.16: MLG decorated with Tinoxide np's response to 9 ppm NH3 at Room Temperature and 40% RH. The flow to the sample equals 500 sscm.

To further evaluate the sensing behaviour, the experiment was repeated after re-annealing the sample in order to remove possible contaminants from the graphene surface. The responses of all devices were successfully measured during the second experiment and are shown in Figure 5.17. Interestingly, the response of the 10% functionalized device decreased to approximately 2.4% without a clear explanation, while the recovery also became worse. In addition, the pristine graphene devices slightly outperformed the functionalized sensors in this measurement.

To investigate whether elevated temperatures would improve the catalytic activity of the tin oxide nanoparticles, an additional measurement was performed at a higher temperature. The results are shown in Figure 5.18. As can be observed, the response strength of all devices decreased by approximately a factor of four. However, the recovery improved substantially, reaching values of around 50%. This suggests that the increased temperature provides sufficient thermal energy to promote desorption of strongly bound gas molecules from the sensing surface, thereby improving sensor recovery [21]. Furthermore, at elevated temperature the functionalized devices slightly outperformed the pristine graphene sensors, indicating that the catalytic activity of tin oxide nanoparticles may become more effective at higher operating temperatures [4].

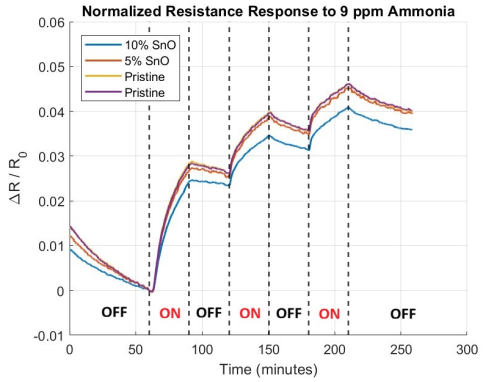

Figure 5.17: MLG decorated with Tinoxide np's response to 9 ppm NH3 at Room Temperature and 40% RH. The flow to the sample equals 500 sscm.

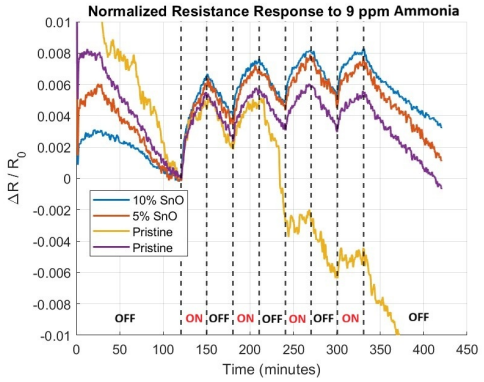

Figure 5.18: MLG decorated with Tinoxide np's response to 9 ppm NH3 at 50 °C and 40% RH. The flow to the sample equals 500 sscm.

5.4. Summary

A summary of the gas sensing experiments that produced reliable and usable data is presented in Table 5.2. From these results, it can be observed that the Grapheana graphene samples generally outperformed the in-house fabricated graphene devices, particularly for ethylene sensing. One possible explanation for this improved performance is the higher material quality indicated by the Raman characterization. The Grapheana samples exhibited better Raman characteristics, suggesting a lower defect density and a more uniform graphene structure. This likely improved charge transport and enhanced the interaction between the graphene surface and adsorbed gas molecules.

Despite successful gas detection, the nanoparticle functionalization did not consistently improve the sensing performance compared to pristine graphene. In several measurements, pristine graphene exhibited either a comparable or stronger response than the nanoparticle-functionalized devices. Additionally, recovery behaviour was often poor, particularly at room temperature, indicating that desorption of the gas molecules from the graphene surface remained limited under these conditions.

Table 5.2: Summary of the successful gas sensing measurements. If not specefied the humidity is 0% RH and the temperature is room temperature.

Sample	Gas and concentration	Magnitude of the best np response (%)	Best np area coverage (%)	Best np recovery (%)	Pristine response (%)	Pristine recovery (%)
In-house Pd	2.1 ppm NO2 (50 sccm)	0.7	2	0	0.7	0
In-house Pristine	2.1 ppm NO2 (250 sccm)	-	-	-	1.25	9
In-house Pt	20 ppm Ethylene (50 sccm)	0.4	1	0	0.52	0
Grapheana Pd	10 ppm Ethylene (100 sccm)	1	14	0	1.6	0
Grapheana Pd	20 ppm Ethylene (50 sccm)	0.4	7	0	0.9	-
Grapheana Pd	5 ppm Ethylene (50 sccm)	0.5	14	0	-	-
Grapheana Pd	4 ppm Ethylene (120 °C)	1.5	7	66	3	27
In-house Pd	50% RH (300 sccm)	3.75	7.5	0	2	0
Grapheana Pd	2.6 ppm Acetic Acid	1.1	14	0	-	-
Grapheana Pd	1 ppm NO2 (40% RH)	6	14	33	-	-
Grapheana Pd	9 ppm NH3 (40% RH)	1.3	21	24.6	-	-
In-house SnO	2.1 ppm NO2 (250 sccm)	1	10	5	1	5
In-house SnO	9 ppm NH3 (40% RH)	4.2	10	20	-	-
In-house SnO	9 ppm NH3 (40% RH)	2.7	5	6	2.9	10
In-house SnO	9 ppm NH3 (40% RH, 50 °C)	0.67	10	39	0.53	55

A second overview of experiments that did not produce convincing responses is presented in Table 5.3. The corresponding measurement figures are included in Appendix B. In many of these failed measurements, either no measurable response was observed or the signal-to-noise ratio was too low to draw reliable conclusions.

Several possible causes contributed to these unsuccessful measurements. These include insufficient gas flow toward the sample, contamination of the graphene devices and unstable electrical probe contacts.

Table 5.3: Summary of gas sensing experiments that produced insufficient or inconclusive results.

Sample	Gas and concentration	Description of failure	Possible causes
In-house Pristine	20 ppm Ethylene (50 sccm)	Weak response and incorrect response direction.	Gas flow toward the sample was likely too low
In-house Pd	3 ppm NH3 (250 sccm)	No measurable response observed.	Unknown
In-house SnO	10 ppm Ethylene (100 sccm)	No measurable response observed.	Unknown
In-house Pt	2.6 ppm Acetic Acid	No clear response and excessive measurement noise.	Poor electrical contacts or unstable setup
In-house Pd contaminated	20 ppm Ethylene (50 sccm)	No measurable response observed.	Sample contamination
In-house Pd contaminated	10 ppm Ethylene (100 sccm)	Noisy signal and no clear response.	Sample contamination
In-house Pd contaminated	1 ppm NO2	Significantly reduced response compared to other devices.	Sample contamination
In-house Cu	5.7 ppm CO2 (100 sccm)	No measurable response observed.	Short stabilization time

5.5. Conclusion

Although the nanoparticle functionalization did not improve the sensitivity of pristine graphene toward ethylene, the performed measurements demonstrated that graphene-based ethylene sensing is feasible. The best result obtained in this work was a response of approximately 1.6% to 10 ppm ethylene at room temperature, as shown in Figure 5.4. This result was obtained using the Grapheana graphene which outperformed the in-house graphene.

In addition to ethylene, the graphene devices were shown to respond to several other gases, including nitrogen dioxide, ammonia, humidity, and acetic acid. The successful detection of acetic acid and ethylene represents the first time these gases were measured using this gas sensing setup. Furthermore, the experiments confirmed that the implemented gas sensing setup, especially the use of large permeation tubes, operates successfully. The only issue is a lack of exhaust for the large permeation tube leading to build-up of the gas in the piping and the inability to have a constant flow between different concentrations.

6

Conclusion

In this thesis, graphene-based gas sensors functionalized with nanoparticles were investigated for the detection of ethylene gas. The work focused on the fabrication of graphene sensor devices, the optimization of nanoparticle deposition using spark ablation printing, the structural and electrical characterization of the fabricated devices, and the evaluation of their gas sensing capabilities. With as primary goal to investigate whether nanoparticle functionalization could improve the sensitivity and selectivity of graphene toward ethylene gas.

A complete fabrication and characterization process for graphene gas sensors was successfully developed. Graphene strips were fabricated and integrated into sensor structures suitable for gas sensing measurements. In addition, a nanoparticle functionalization process based on spark ablation printing using the VSParticle system was implemented and optimized. Palladium, Platinum, and SnO nanoparticles were investigated as possible functionalization materials.

The nanoparticle printing process was studied to achieve controlled and repeatable area coverage. It was shown that increasing the printing speed generally reduced the nanoparticle area coverage, while higher spark currents and voltages increased the amount of deposited material. Through these optimization experiments, reproducible nanoparticle depositions with low area coverage suitable for gas sensing applications were achieved.

The influence of annealing on nanoparticle morphology and area coverage was also investigated. SEM imaging demonstrated that annealing causes nanoparticle sintering and agglomeration, leading to a reduction in the projected nanoparticle area coverage. This effect was observed both on silicon substrates and on graphene samples. High-temperature annealing on silicon produced a strong reduction in nanoparticle coverage due to extensive particle clustering, whereas the lower-temperature annealing process used for the graphene devices resulted in a smaller but still significant decrease in area coverage. These results show that the final nanoparticle density after annealing can change from the initially deposited state and therefore must be considered when designing functionalized graphene sensors.

Scanning Electron Microscopy (SEM) was used to evaluate the morphology and structural quality of the graphene samples. SEM images confirmed the successful fabrication of graphene structures and allowed visual inspection of the graphene surface before and after processing steps such as molybdenum etching, nanoparticle deposition, and annealing. The SEM results showed that removing the molybdenum substrate significantly changes the visual appearance of the graphene surface, whereas nanoparticle deposition and annealing did not introduce major visible damage to pristine graphene regions.

The commercially obtained Grapheana graphene samples were also analysed and compared with the in-house fabricated graphene. The Grapheana samples exhibited a smoother and more uniform surface morphology than the in-house graphene, likely due to differences in fabrication and transfer processes. Minor nanoparticle contamination was observed on some graphene regions, probably caused by nanoparticle transport inside the deposition chamber during nearby printing operations or due to residues in the fabrication.

Raman spectroscopy was used as the primary method for evaluating graphene quality. Analysis of the D, G, and 2D peaks provided information about defect density, crystallinity, and graphene layer count. The in-house fabricated multilayer graphene samples exhibited Raman characteristics comparable to values previously reported for similar fabrication processes. Before molybdenum etching, the Raman spectra were strongly influenced by the molybdenum, resulting in poor Raman quality metrics. After etching, the Raman spectra improved significantly and showed values more representative of graphene itself.

The effect of nanoparticle functionalization on the Raman spectra was also investigated. Only limited changes in the Raman peak ratios and peak widths were observed after nanoparticle deposition, indicating that the spark ablation printing process caused minimal structural damage to the graphene.

Electrical characterization was performed through sheet resistance measurements. Most graphene samples exhibited sheet resistance values on the order of (1 $k\Omega$), which is consistent with previously reported values for similar graphene structures. The sheet resistance increased significantly due to nanoparticle functionalization, likely indicating that the carrier mobility was decreased due to the functionalization.

Gas sensing measurements demonstrated that both pristine and nanoparticle-functionalized graphene devices were capable of responding to ethylene gas exposure. This confirms that the fabricated graphene structures can operate as ethylene sensing devices. In addition, it was found that a low amount of flow used to measure a gas can negatively impact the strength of the response. Besides ethylene, the graphene sensors were able to sense other gasses successfully as well, including nitrogen dioxide, ammonia, humidity, and acetic acid.

Overall, this work demonstrates the successful fabrication, functionalization, and characterization of graphene-based gas sensors. However, the central research question of whether nanoparticle functionalization can improve the selectivity of graphene gas sensors towards ethylene remains inconclusive. Under the experimental conditions investigated in this study, the selected nanoparticle functionalizations did not result in an improvement in ethylene sensitivity compared to pristine graphene.

6.1. Discussion

As shown in the summary presented in Table 5.2, the addition of platinum and palladium nanoparticles did not improve the sensitivity, recovery behaviour, or response time of the graphene gas sensors for ethylene and the other investigated gases. In several measurements, the pristine graphene devices even outperformed the nanoparticle-functionalized samples. This result was unexpected, as previous studies such as A. M. Akhir et al. [34] and Jin et al. [27] reported significant improvements in gas sensing performance after the addition of palladium nanoparticles to SnO2 and ZnO sensing layers.

Several possible explanations may account for the underperformance of the functionalization.

1. The nanoparticle area coverage was not optimal.
2. The nanoparticle size was too large.
3. The p-type behaviour of the graphene influenced the sensing mechanism.
4. The operating temperature was too low to activate the catalytic effects.

The first possibility concerns the nanoparticle area coverage. It is unlikely that the coverage was too low to produce any catalytic effect. If the nanoparticle density had simply been insufficient, a smaller enhancement in response would be expected rather than the observed reduction in sensitivity in some cases. Similarly, it is also unlikely that the coverage was excessively high, since measurements were performed using low coverages of approximately 1%. Previous work by colleagues using graphene functionalization for other gases reported optimal nanoparticle coverages within a similar range [8]. Therefore, although nanoparticle density may influence the sensing behaviour, it is unlikely to fully explain the absence of improved performance.

Another explanation could be the nanoparticle size. In other works, palladium nanoparticles with diameters of only a few nanometers are typically used. For example, the nanoparticles reported by A.

M. Akhir et al. [34] were approximately 2 nm in size. In contrast, the particles produced in this work were generally much larger, as shown in Figure 4.3. Producing significantly smaller nanoparticles with the current spark ablation setup proved difficult. The maximum carrier gas flow rate was already used to reduce particle size as much as possible, while lowering the spark current further resulted in unstable or inconsistent nanoparticle generation. As a result, the fabrication setup imposed practical limitations on the nanoparticle size.

The p-type nature of the graphene devices also appears unlikely to be the primary cause of the limited functionalization effect. Previous studies demonstrating successful palladium functionalization, such as A. M. Akhir et al. [34], used SnO2 as the sensing layer, which is also p-type. Therefore, the charge carrier type alone is probably insufficient to explain the absence of catalytic enhancement.

The most likely explanation is the relatively low operating temperature used during the gas sensing measurements. In the studies by A. M. Akhir et al. [34] and Jin et al. [27], the sensors were operated at temperatures around 300 °C. One possible mechanism is that the catalytic activity associated with reactions such as Wacker oxidation does not occur efficiently at room temperature or even at the moderately elevated temperatures used in this work.

The measurements performed at 120 °C already showed improved recovery behaviour compared to room-temperature measurements, suggesting that temperature indeed plays an important role in activating the sensing mechanisms. Unfortunately, the current gas sensing setup could not reliably operate at temperatures approaching 300 °C. In addition, the graphene devices themselves were unlikely to remain stable at such temperatures, as the gold contacts used for the electrical connections would likely degrade or fail. Evidence of thermal degradation effects can be found in Appendix A.

As help for writing this thesis generative AI was used to rewrite some parts of the texts for better readability and grammar.

6.2. Future Recommendations

Although graphene-based ethylene sensing was demonstrated in this work, several improvements and research directions can be explored to further enhance the sensing performance and better understand the underlying mechanisms.

One important recommendation is the development of a gas sensing setup capable of operating at significantly higher temperatures. Previous studies involving palladium functionalized metal oxide sensors reported optimal sensing performance at temperatures around 300 °C [27, 34].

Related to this, additives commonly used in catalytic processes such as the Wacker oxidation process could also be investigated. Such additives may lower the activation energy of the catalytic reactions and enable improved sensing at lower temperatures. One possible approach is the introduction of chlorine solution near the graphene. However, chlorine is highly reactive and could damage the graphene or interconnect. Therefore, any implementation of such additives would likely require careful encapsulation and membranes.

Another direction is the investigation of alternative nanoparticle materials and morphologies. In this work, relatively large and fractal-like nanoparticles were produced using spark ablation. Future studies could investigate nanoparticles with smaller diameters and more spherical closer to previous literature. There nanoparticles only a few nanometers in size were used. Additionally, other nanoparticle materials beyond palladium, platinum and tin oxide may provide improved selectivity towards ethylene or other target gases.

The recovery of the graphene sensors also has room for improvement. Many of the measurements performed in this work exhibited slow or incomplete recovery after gas exposure. One possible method to improve recovery is the use of ultraviolet (UV) illumination during or after sensing measurements.

To improve the accuracy of the ethylene concentration control, future setups should include active temperature regulation for the large permeation tube. In the current setup, the large permeation tube remained at ambient laboratory temperature, causing variations in the permeation rate depending on temperature fluctuations. By integrating a heater and temperature sensor, the permeation tube could

be maintained at its calibration temperature, resulting in more accurate and reproducible ethylene concentrations.

Furthermore, the location of the large permeation tube can be improved. Currently, the large permeation tube does not have access to an exhaust path, preventing access to certain flow to concentration ratios. Putting the large permeation tube in the at the intake of the V-OVG would allow the use of the exhaust.

Finally, additional studies can be performed to further investigate the influence of gas flow on the gas sensors. In this work the gas flow rate affected the measured response. Future experiments could therefore employ a closed sensing chamber in which a stable gas concentration is maintained without requiring continuous flow.

References

[1] F. B. Abeles, P. W. Morgan, and M. E. Saltveit. *Ethylene in Plant Biology*. 2nd ed. San Diego: Academic Press, 1992.

[2] S. M. Cristescu et al. "Methods of detection of ethylene in plants". In: *Plant Physiology* 163 (2013), pp. 531–543.

[3] Xiaohu Chen, Ryan Wreyford, and Noushin Nasiri. "Recent Advances in Ethylene Gas Detection". In: *Materials* 15.17 (2022). ISSN: 1996-1944. DOI: 10.3390/ma15175813. URL: https://www.mdpi.com/1996-1944/15/17/5813.

[4] Ghenadii Korotcenkov. *Handbook of Gas Sensor Materials*. Vol. 1. Springer, 2013.

[5] K. S. Novoselov et al. "Electric Field Effect in Atomically Thin Carbon Films". In: *Science* 306.5696 (2004), pp. 666–669. DOI: 10.1126/science.1102896.

[6] F. Schedin et al. "Detection of Individual Gas Molecules Adsorbed on Graphene". In: *Nature Materials* 6 (2007), pp. 652–655. DOI: 10.1038/nmat1967.

[7] Farid Yavari and Nikhil Koratkar. "Graphene-based chemical sensors". In: *The Journal of Physical Chemistry Letters* 3.13 (2012), pp. 1746–1753. DOI: 10.1021/jz300358t.

[8] Mudassir Husain et al. "Highly Sensitive NO2 Gas Sensors by Spark Ablation on CVD Graphene". In: *2025 23rd International Conference on Solid-State Sensors, Actuators and Microsystems (Transducers)*. 2025, pp. 1081–1084. DOI: 10.1109/Transducers61432.2025.11109858.

[9] Wei Yuan and Guoquan Shi. "Graphene-based gas sensors". In: *Journal of Materials Chemistry A* 1.35 (2013), pp. 10078–10091. DOI: 10.1039/C3TA11774J.

[10] Andre K. Geim and Konstantin S. Novoselov. "The Rise of Graphene". In: *Nature Materials* 6.3 (2007), pp. 183–191. DOI: 10.1038/nmat1849.

[11] A. H. Castro Neto et al. "The Electronic Properties of Graphene". In: *Reviews of Modern Physics* 81.1 (2009), pp. 109–162. DOI: 10.1103/RevModPhys.81.109.

[12] Emi Schutz. *Unlocking the Full Potential of Graphene*. Accessed: 2026-03-12. Chembites. Dec. 2018. URL: https://chembites.org/2018/12/13/unlocking-the-full-potential-of-graphene/.

[13] International Organization for Standardization. *Nanotechnologies — Vocabulary — Part 13: Graphene and related two-dimensional (2D) materials*. Technical Specification ISO/TS 80004-13:2017. Geneva, Switzerland: ISO, 2017.

[14] Changgu Lee et al. "Measurement of the Elastic Properties and Intrinsic Strength of Monolayer Graphene". In: *Science* 321.5887 (2008), pp. 385–388. DOI: 10.1126/science.1157996.

[15] Frank Schwierz. "Graphene Transistors". In: *Nature Nanotechnology* 5 (2010), pp. 487–496. DOI: 10.1038/nnano.2010.89.

[16] Y. Hernandez et al. "High-Yield Production of Graphene by Liquid-Phase Exfoliation of Graphite". In: *Nature Nanotechnology* 3 (2008), pp. 563–568. DOI: 10.1038/nnano.2008.215.

[17] Jonathan N. Coleman. "Liquid Exfoliation of Defect-Free Graphene". In: *Accounts of Chemical Research* 46 (2013), pp. 14–22. DOI: 10.1021/ar300009f.

[18] Xuesong Li et al. "Large-Area Synthesis of High-Quality and Uniform Graphene Films on Copper Foils". In: *Science* 324 (2009), pp. 1312–1314. DOI: 10.1126/science.1171245.

[19] S. Vollebregt et al. "A Transfer-Free Wafer-Scale CVD Graphene Fabrication Process for MEMS/NEMS Sensors". In: *Sensors and Actuators A: Physical* 317 (2021). Delft University of Technology, Department of Microelectronics, Delft, The Netherlands; University of Naples Federico II, ENEA UTTP-MDB, Italian Institute of Technology, MEMS Foundry Services, p. 112468. DOI: 10.1016/j.sna.2020.112468.

[20] Sergey Rumyantsev et al. “Electrical and Noise Characteristics of Graphene Field-Effect Transistors: Ambient Effects, Noise Sources and Physical Mechanisms”. In: *Journal of Physics: Condensed Matter* 22 (2012), p. 395302.

[21] Seba S. Varghese et al. “Recent advances in graphene based gas sensors”. In: *Sensors and Actuators B: Chemical* 218 (2015), pp. 160–183. ISSN: 0925-4005. DOI: https://doi.org/10.1016/j.snb.2015.04.062. URL: https://www.sciencedirect.com/science/article/pii/S0925400515005146.

[22] K. S. Novoselov et al. “A roadmap for graphene”. In: *Nature* 490.7419 (2012), pp. 192–200. DOI: 10.1038/nature11458.

[23] Siby S. Varghese et al. “Two-dimensional materials for sensing: graphene and beyond”. In: *Sensors and Actuators B: Chemical* 218 (2015), pp. 160–183. DOI: 10.1016/j.snb.2015.04.062.

[24] H. J. van Ginkel. “Printed Spark Ablation Nanoparticle Films for Microelectronic Applications”. PhD thesis. Delft University of Technology, 2024. DOI: 10.4233/uuid:17b83ad6-3179-4a10-8194-90c4e6c768b2. URL: https://doi.org/10.4233/uuid:17b83ad6-3179-4a10-8194-90c4e6c768b2.

[25] V. Amendola and M. Meneghetti. “Laser ablation synthesis in solution and size manipulation of noble metal nanoparticles”. In: *Physical Chemistry Chemical Physics* 11 (2010), pp. 3805–3821.

[26] G. W. Yang. “Laser ablation in liquids: Applications in the synthesis of nanocrystals”. In: *Progress in Materials Science* 52.4 (2012), pp. 648–698.

[27] Zhen Jin et al. “Highly Sensitive Ethylene Sensors Based on Ultrafine Pd Nanoparticles-Decorated Porous ZnO Nanosheets and Their Application in Fruit Ripeness Detection”. In: *Sensors* 20.21 (2020), pp. 1–14. DOI: 10.3390/s20216125.

[28] Joshua T. Robinson et al. “Reduced graphene oxide molecular sensors”. In: *Nano Letters* 8.10 (2008), pp. 3137–3140. DOI: 10.1021/nl8013007.

[29] Jae-Hyoung Lee et al. “Optimization of the surface coverage of metal nanoparticles on nanowires gas sensors to achieve the optimal sensing performance”. In: *Sensors and Actuators B: Chemical* 302 (2020), p. 127196. ISSN: 0925-4005. DOI: https://doi.org/10.1016/j.snb.2019.127196. URL: https://www.sciencedirect.com/science/article/pii/S0925400519313954.

[30] Zain Ul Abideen, Jae-Hun Kim, and Sang Sub Kim. “Optimization of metal nanoparticle amount on SnO2 nanowires to achieve superior gas sensing properties”. In: *Sensors and Actuators B: Chemical* 238 (2017), pp. 374–380. ISSN: 0925-4005. DOI: https://doi.org/10.1016/j.snb.2016.07.054. URL: https://www.sciencedirect.com/science/article/pii/S0925400516310899.

[31] A.B. Evnin, J.A. Rabo, and P.H. Kasai. “Heterogeneously catalyzed vapor-phase oxidation of ethylene to acetaldehyde”. In: *Journal of Catalysis* 30.1 (1973), pp. 109–117. ISSN: 0021-9517. DOI: https://doi.org/10.1016/0021-9517(73)90057-2. URL: https://www.sciencedirect.com/science/article/pii/0021951773900572.

[32] Xu-Ying Liu, Jian-Min Zhang, and Ke-Wei Xu. “Chlorine molecule adsorbed on graphene and doped graphene: A first-principle study”. In: *Physica B: Condensed Matter* 436 (2014), pp. 54–58. ISSN: 0921-4526. DOI: https://doi.org/10.1016/j.physb.2013.11.042. URL: https://www.sciencedirect.com/science/article/pii/S0921452613007552.

[33] Francisco Zaera. “The Surface Chemistry of Metal-Based Hydrogenation Catalysis”. In: *ACS Catalysis* 7.8 (2017), pp. 4947–4967. DOI: 10.1021/acscatal.7b01368. eprint: https://doi.org/10.1021/acscatal.7b01368. URL: https://doi.org/10.1021/acscatal.7b01368.

[34] M. A. M. Akhir et al. “Synthesis of SnO2 Nanoparticles via Hydrothermal Method and Their Gas Sensing Applications for Ethylene Detection”. In: *Materials Today: Proceedings* 17 (2019). 6th International Conference on Recent Advances in Materials, Minerals Environment (RAMM) 2018, RAMM 2018, 27 - 29 November 2018, Penang, Malaysia, pp. 810–819. ISSN: 2214-7853. DOI: https://doi.org/10.1016/j.matpr.2019.06.367. URL: https://www.sciencedirect.com/science/article/pii/S2214785319317377.

[35] Álvaro Peña et al. “Optimization of multilayer graphene-based gas sensors by ultraviolet photoactivation”. In: *Sensors and Actuators B: Chemical* 283 (2019), pp. 651–662. DOI: 10.1016/j.snb.2018.12.094.

[36] John Robertson. "Atomic Structure of Graphene and Its Interfaces". In: *Materials Science and Engineering R* 37 (2012), pp. 129–281. DOI: 10.1016/S0927-796X(02)00005-0.

[37] Michael J. Coutts et al. "Rapid and Controllable Sintering of Gold Nanoparticle Inks at Room Temperature Using a Chemical Agent". In: *The Journal of Physical Chemistry C* 113.4 (2009), pp. 1325–1328. DOI: 10.1021/jp808927t. URL: https://doi.org/10.1021/jp808927t.

[38] Filiberto Ricciardella et al. "Growth of multi-layered graphene on molybdenum catalyst by solid phase reaction with amorphous carbon". English. In: *2D Materials* 6.3 (2019). Green Open Access added to TU Delft Institutional Repository 'You share, we take care!' – Taverne project https://www.openaccess.nl/en/you-share-we-take-care Otherwise as indicated in the copyright section: the publisher is the copyright holder of this work and the author uses the Dutch legislation to make this work public., pp. 1–11. ISSN: 2053-1583. DOI: 10.1088/2053-1583/ab1518.

[39] VSParticle. *Spark Ablation for Nanoporous Material Production*. Accessed: 2026-04-24. 2024. URL: https://vsparticle.com/5/blog/spark-ablation-for-nanoporous-material-production.

[40] Electronic Components, Technology and Materials Group. *ECTM Repository*. Accessed: 2026-04-25. 2020. URL: https://ectm.tudelft.nl/Repository/repitem.php?id=32&ti=13.

[41] MSE Supplies LLC. *Everything You Should Know About Scanning Electron Microscopy (SEM) — Before Sending Us Your Samples*. Accessed: 2026-04-19. July 2025. URL: https://www.msesupplies.com/blogs/news/everything-you-should-know-about-scanning-electron-microscopy-sem-before-sending-us-your-samples.

[42] JEOL USA. *Gentle Beam: Improving Low Voltage Performance*. Accessed: 2026-05-11. Nov. 2020. URL: https://www.jeolusa.com/RESOURCES/Electron-Optics/Documents-Downloads/gentle-beam-improving-low-voltage-performance.

[43] Materials Characterization and Preparation Facility (GZ). *Ultra-high Resolution Scanning Electron Microscope (SEM) Regulus8230*. Accessed: 2026-04-19. Mar. 2025. URL: https://mcpf.hkust-gz.edu.cn/2025/03/06/ultra-high-resolution-scanning-electron-microscope-sem/.

[44] Thomas Schmid and Petra Dariz. "Raman Microspectroscopic Imaging of Binder Remnants in Historical Mortars Reveals Processing Conditions". In: *Heritage* 2.2 (2019), pp. 1662–1683. ISSN: 2571-9408. DOI: 10.3390/heritage2020102. URL: https://www.mdpi.com/2571-9408/2/2/102.

[45] L. G. Cançado et al. "Quantifying Defects in Graphene via Raman Spectroscopy at Different Excitation Energies". In: *Nano Letters* 11.8 (2011). PMID: 21696186, pp. 3190–3196. DOI: 10.1021/nl201432g. eprint: https://doi.org/10.1021/nl201432g. URL: https://doi.org/10.1021/nl201432g.

[46] Girija Shankar Papanai, Indu Sharma, and Bipin Kumar Gupta. "Probing number of layers and quality assessment of mechanically exfoliated graphene via Raman fingerprint". In: *Materials Today Communications* 22 (2020), p. 100795. ISSN: 2352-4928. DOI: https://doi.org/10.1016/j.mtcomm.2019.100795. URL: https://www.sciencedirect.com/science/article/pii/S2352492819313935.

[47] Filiberto Ricciardella et al. "Effects of graphene defects on gas sensing properties towards NO_2 detection". In: *Nanoscale* 9.18 (2017), pp. 6085–6093. DOI: 10.1039/C7NR01120B.

[48] VICI Metronics. *Dynacal Permeation Tube*. Accessed: 2026-04-28. 2026. URL: https://www.vicimetronics.com/products/perm-tube.

[49] VICI Metronics. *G-Cal Permeation Devices*. Accessed: 2026-04-28. 2026. URL: https://www.vicimetronics.com/products/g-cal?variant=39273993699383.

[50] S. J. Rice. "Graphene with Platinum Nanoparticles for Neural Recording and Stimulation". Master's thesis. Delft, The Netherlands: Delft University of Technology, 2023. URL: https://resolver.tudelft.nl/uuid:d2ed52e8-21e2-495f-89f7-d85901d9dfd4.

[51] Borislav Vasić et al. "Low-friction, wear-resistant, and electrically homogeneous multilayer graphene grown by chemical vapor deposition on molybdenum". In: *Applied Surface Science* 509 (2020), p. 144792. ISSN: 0169-4332. DOI: https://doi.org/10.1016/j.apsusc.2019.144792. URL: https://www.sciencedirect.com/science/article/pii/S0169433219336086.

[52] V. E. Calado et al. “Formation and control of wrinkles in graphene by the wedging transfer method”. In: *Applied Physics Letters* 101.10 (Sept. 2012), p. 103116. ISSN: 0003-6951. DOI: 10.1063/1.4751982. eprint: https://pubs.aip.org/aip/apl/article-pdf/doi/10.1063/1.4751982/14254838/103116_1_online.pdf. URL: https://doi.org/10.1063/1.4751982.

[53] Hanxing Meng. “Gas Sensor Based on Array of Multi-Layer Graphene Decorated with Metal/Metal Oxide Nanoparticles”. Accessed: 2026-05-11. Master Thesis. Delft University of Technology, 2022. URL: https://resolver.tudelft.nl/uuid:9d71b753-9b59-4c40-a690-70e2489d30c4.

[54] Herbert B. Michaelson. “The work function of the elements and its periodicity”. In: *Journal of Applied Physics* 48.11 (Nov. 1977), pp. 4729–4733. ISSN: 0021-8979. DOI: 10.1063/1.323539. eprint: https://pubs.aip.org/aip/jap/article-pdf/48/11/4729/18378039/4729_1_online.pdf. URL: https://doi.org/10.1063/1.323539.

[55] Jian-Hao Chen et al. “Defect Scattering in Graphene”. In: *Phys. Rev. Lett.* 102 (23 June 2009), p. 236805. DOI: 10.1103/PhysRevLett.102.236805. URL: https://link.aps.org/doi/10.1103/PhysRevLett.102.236805.

[56] Kendal W. Clark et al. “Spatially Resolved Mapping of Electrical Conductivity across Individual Domain (Grain) Boundaries in Graphene”. In: *ACS Nano* 7.9 (2013). PMID: 23952068, pp. 7956–7966. DOI: 10.1021/nn403056k. eprint: https://doi.org/10.1021/nn403056k. URL: https://doi.org/10.1021/nn403056k.

[57] Javier Carrasco, Jiří Klimeš, and Angelos Michaelides. “The role of van der Waals forces in water adsorption on metals”. In: *The Journal of Chemical Physics* 138.2 (Jan. 2013), p. 024708. ISSN: 0021-9606. DOI: 10.1063/1.4773901. eprint: https://pubs.aip.org/aip/jcp/article-pdf/doi/10.1063/1.4773901/14794398/024708_1_online.pdf. URL: https://doi.org/10.1063/1.4773901.

[58] Ruiyang You et al. “Unveiling Water-Vapor-Promoted Oxidation of Palladium Nanoparticles via Atomic-Scale Transmission Electron Microscopy at Atmospheric Pressure”. In: *Journal of the American Chemical Society* 147.31 (2025). PMID: 40717300, pp. 28035–28043. DOI: 10.1021/jacs.5c07765. eprint: https://doi.org/10.1021/jacs.5c07765. URL: https://doi.org/10.1021/jacs.5c07765.

[59] M. Johansson, D. Loyd, and I. Lundström. “Influence of mass transfer on the steady-state response of catalytic-metal-gate gas sensors”. In: *Sensors and Actuators B: Chemical* 40.2 (1997), pp. 125–133. ISSN: 0925-4005. DOI: https://doi.org/10.1016/S0925-4005(97)80251-1. URL: https://www.sciencedirect.com/science/article/pii/S0925400597802511.

[60] Naoki Matsunaga et al. “Diffusion equation-based study of thin film semiconductor gas sensor-response transient”. In: *Sensors and Actuators B: Chemical* 83.1 (2002). Selected Papers from TRANSDUCERS ’01 EUROSENSORS XV, pp. 216–221. ISSN: 0925-4005. DOI: https://doi.org/10.1016/S0925-4005(01)01043-7. URL: https://www.sciencedirect.com/science/article/pii/S0925400501010437.

A

Breakage due to high annealing temperature

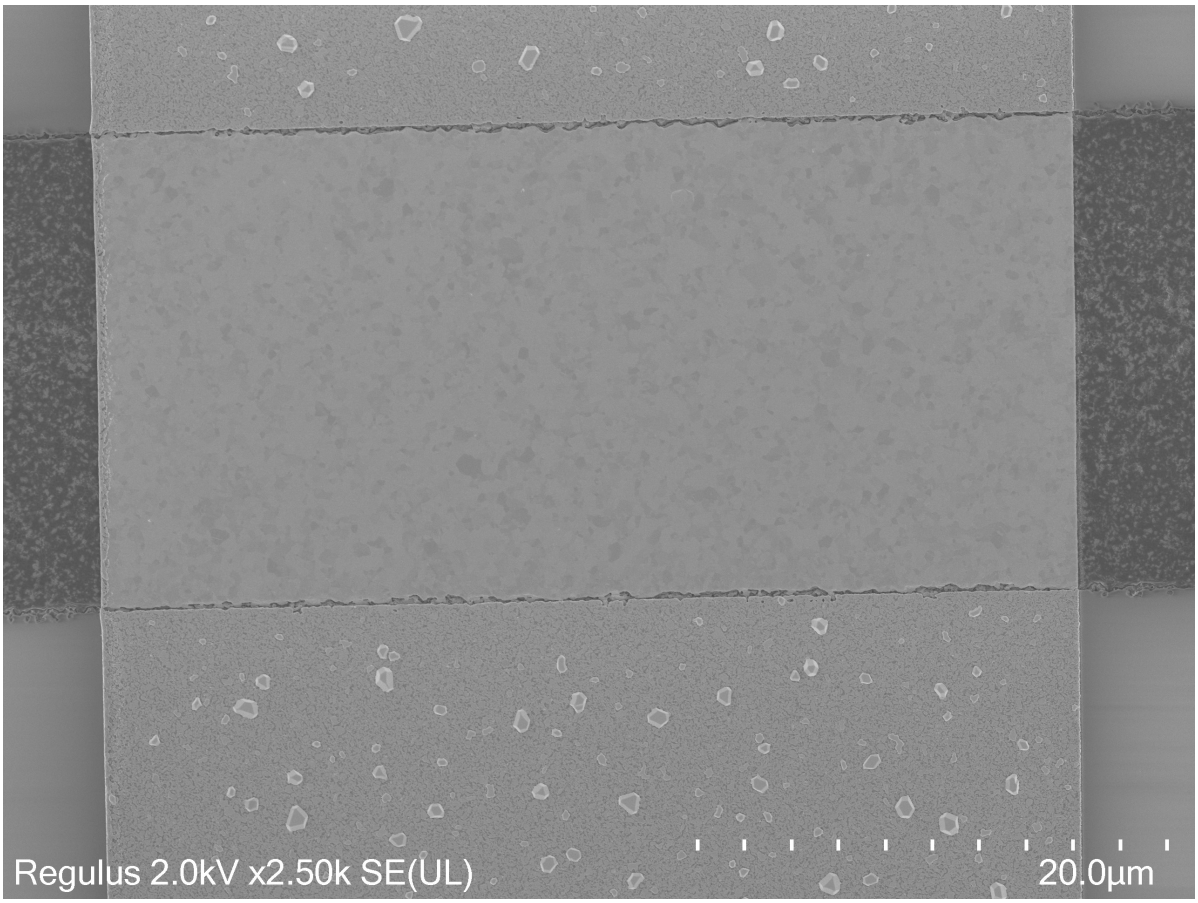

Figure A.1: Broken connection of gold (Vertical) to graphene (horizontal) after annealing at 400C

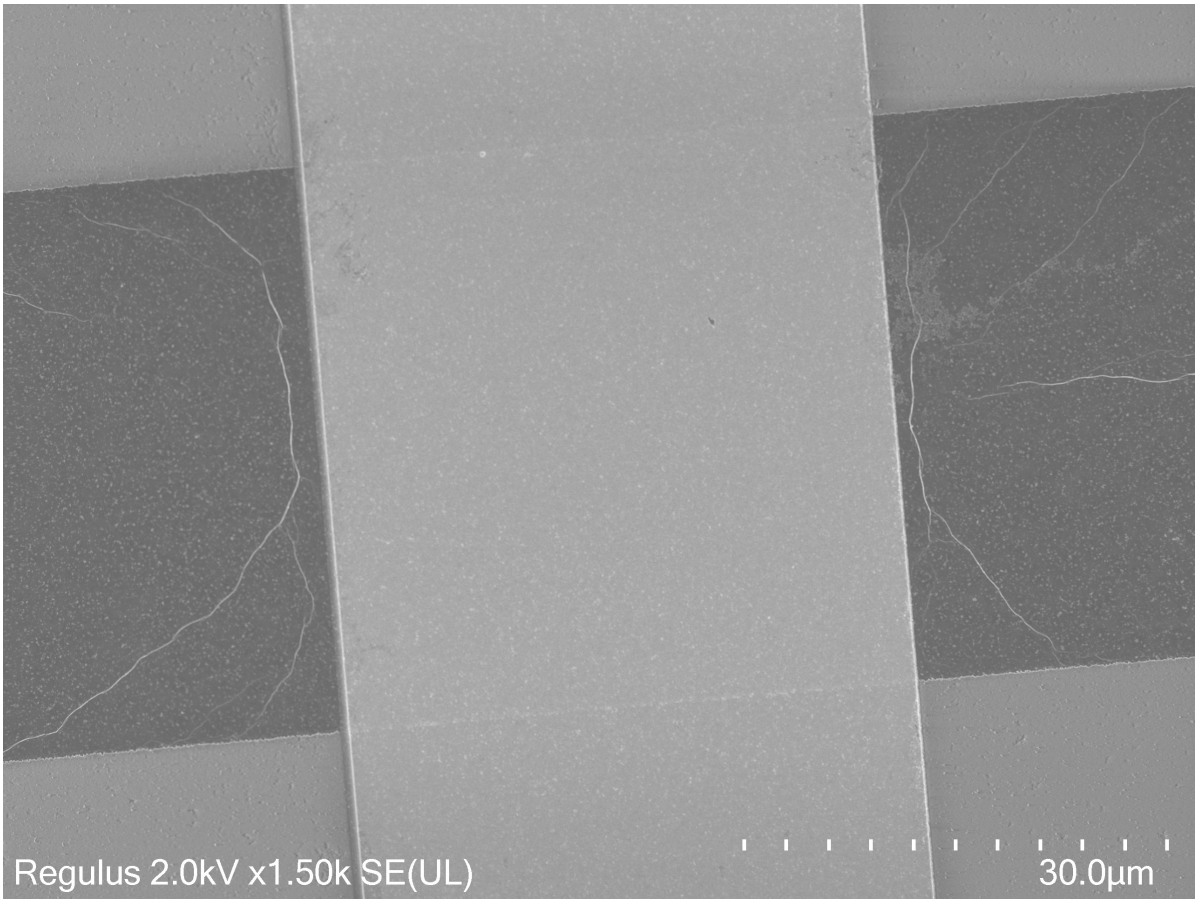

Figure A.2: Reference connection of gold (Vertical) to graphene (horizontal)

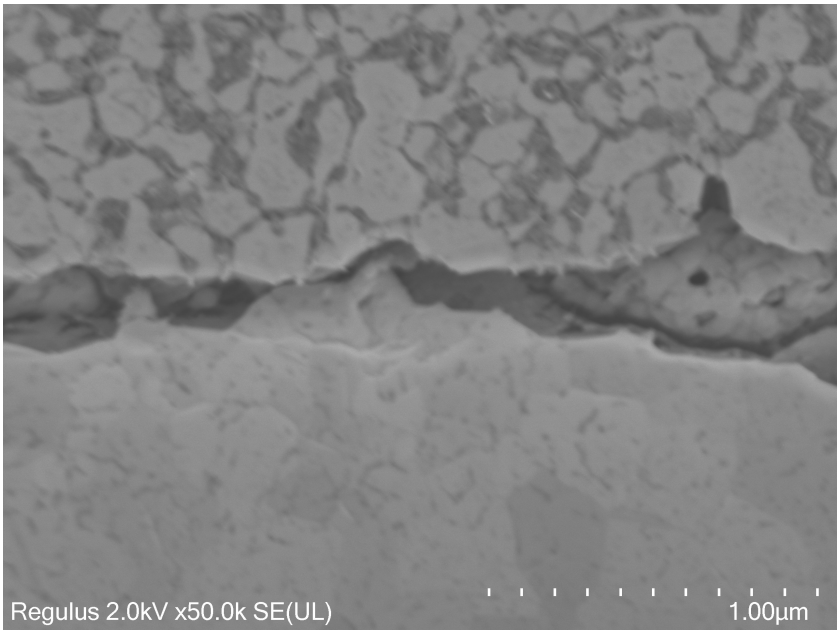

Figure A.3: Breakage line between the gold connected to the graphene and the gold connected to the pins

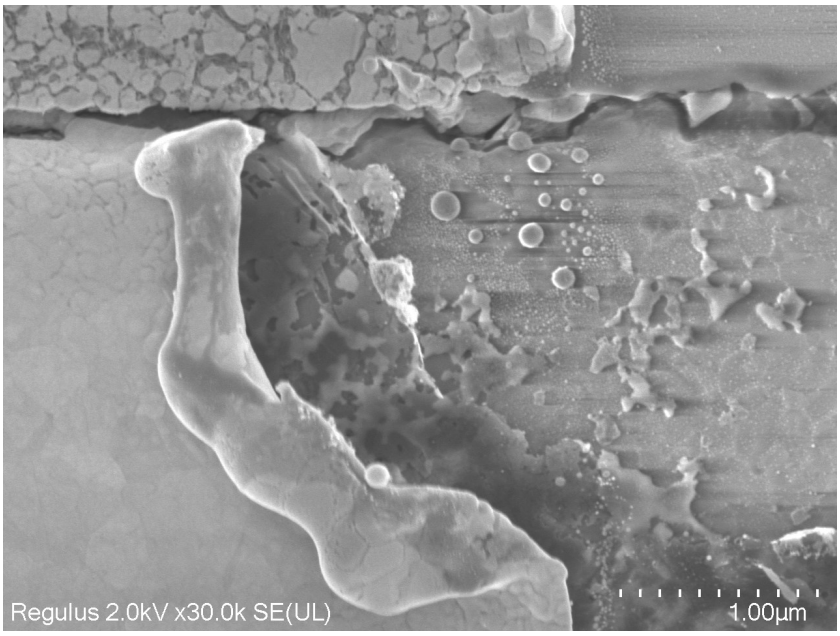

Figure A.4: Corner of a broken conection

B

Failed gas sensing data

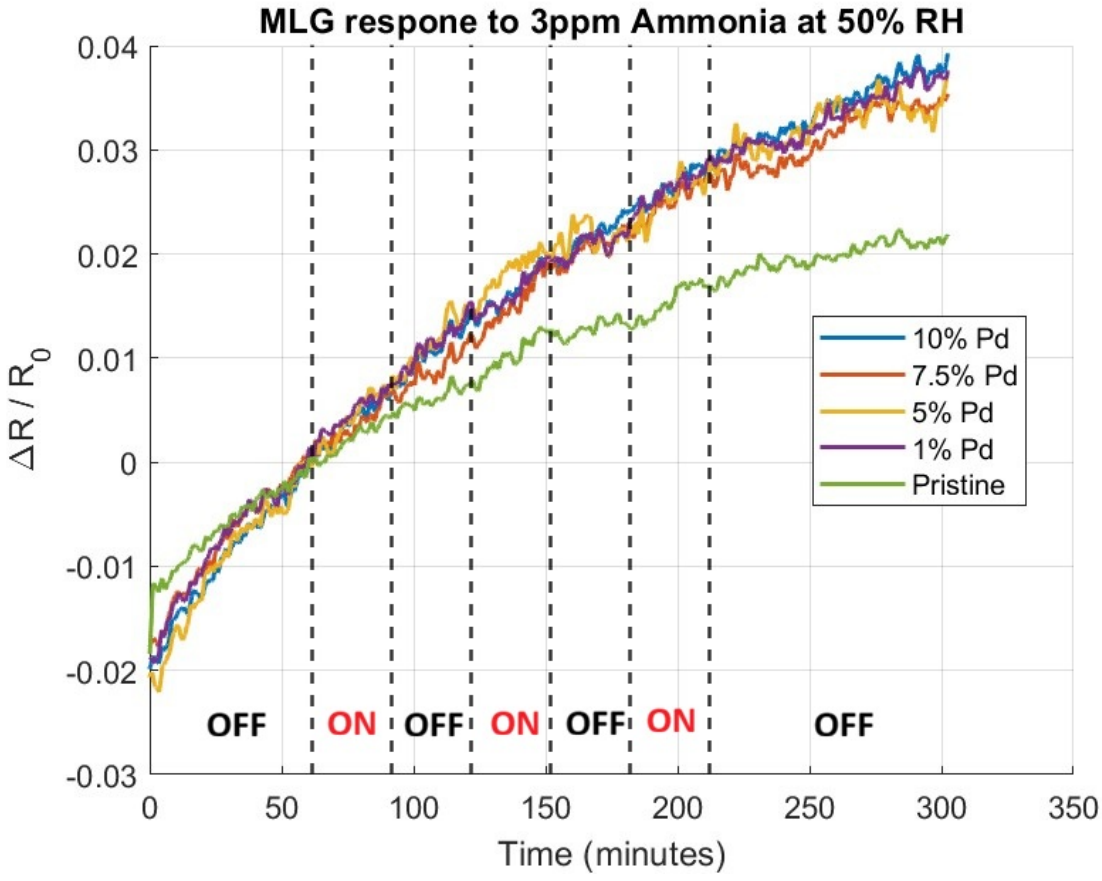

Figure B.1: MLG decorated with Palladium np's response to 3 ppm NH3 at Room Temperature and 50% RH. The flow to the sample equals 500 sscm.

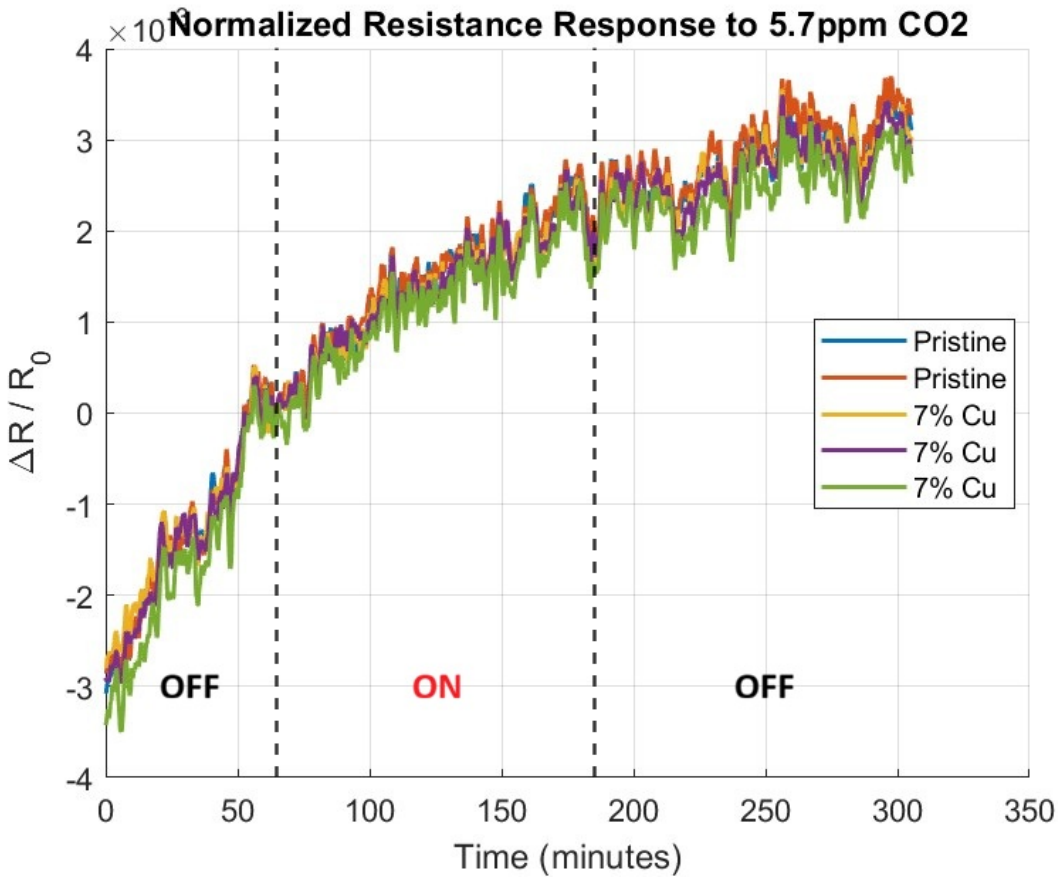

Figure B.2: MLG decorated with copper np's response to 5.7 ppm CO2 at Room Temperature and 0% RH. The flow to the sample equals 100 sscm.

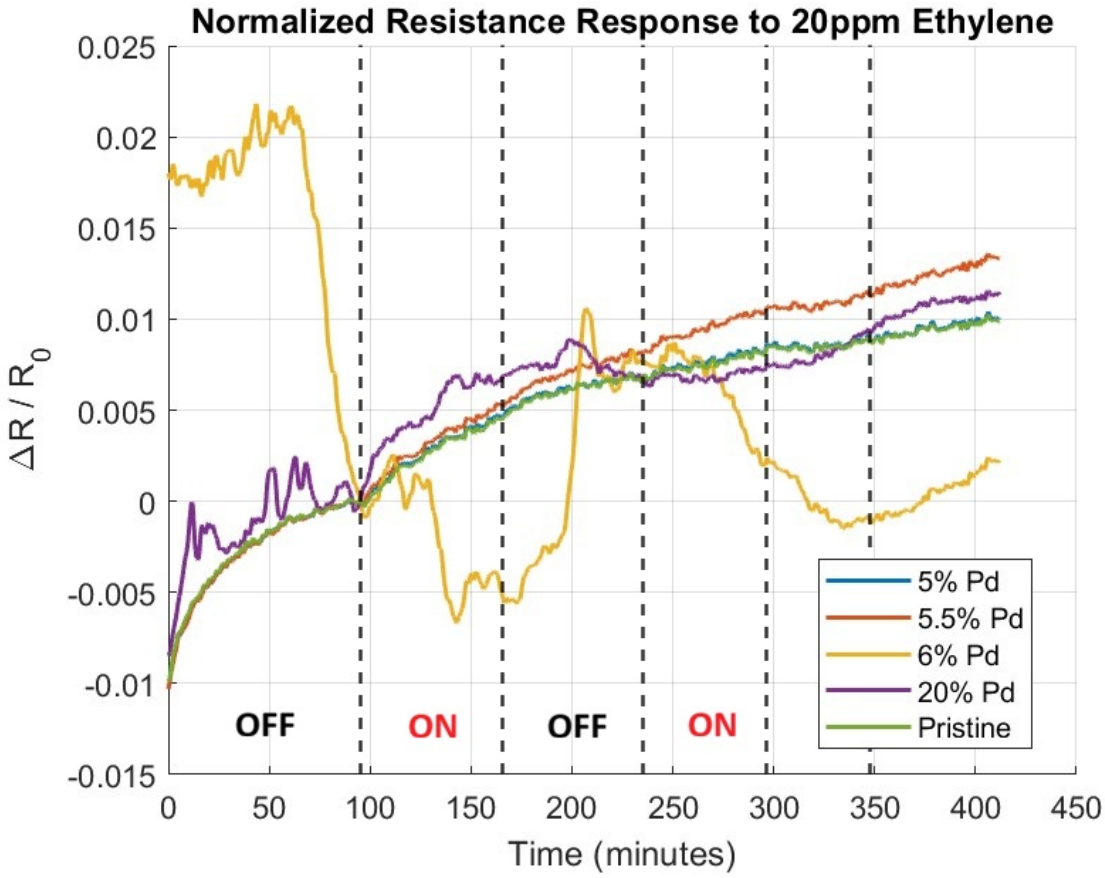

Figure B.3: MLG decorated with Palladium np's that were found to be contaminated response to 20 ppm Ethylene at Room Temperature and 0% RH. The flow to the sample equals 50 sscm.

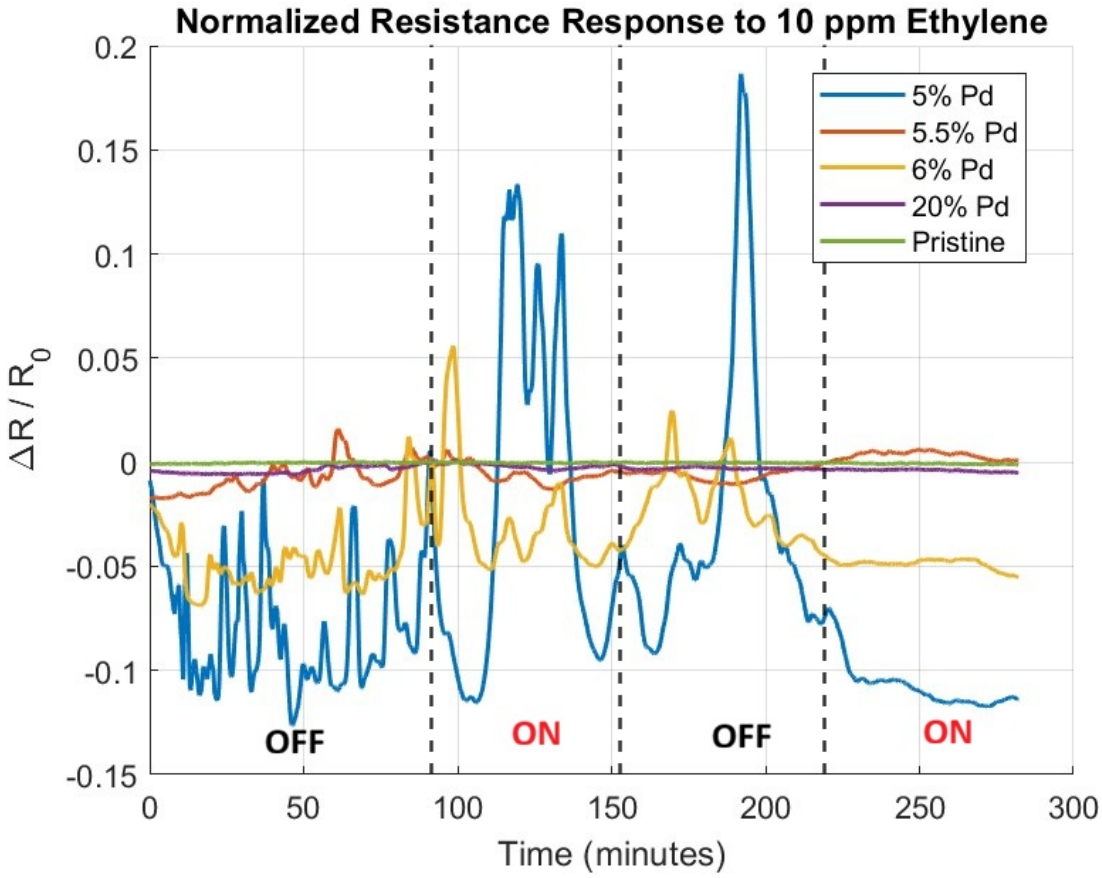

Figure B.4: MLG decorated with Palladium np's that were found to be contaminated response to 10 ppm Ethylene at Room Temperature and 0% RH. The flow to the sample equals 100 sscm.

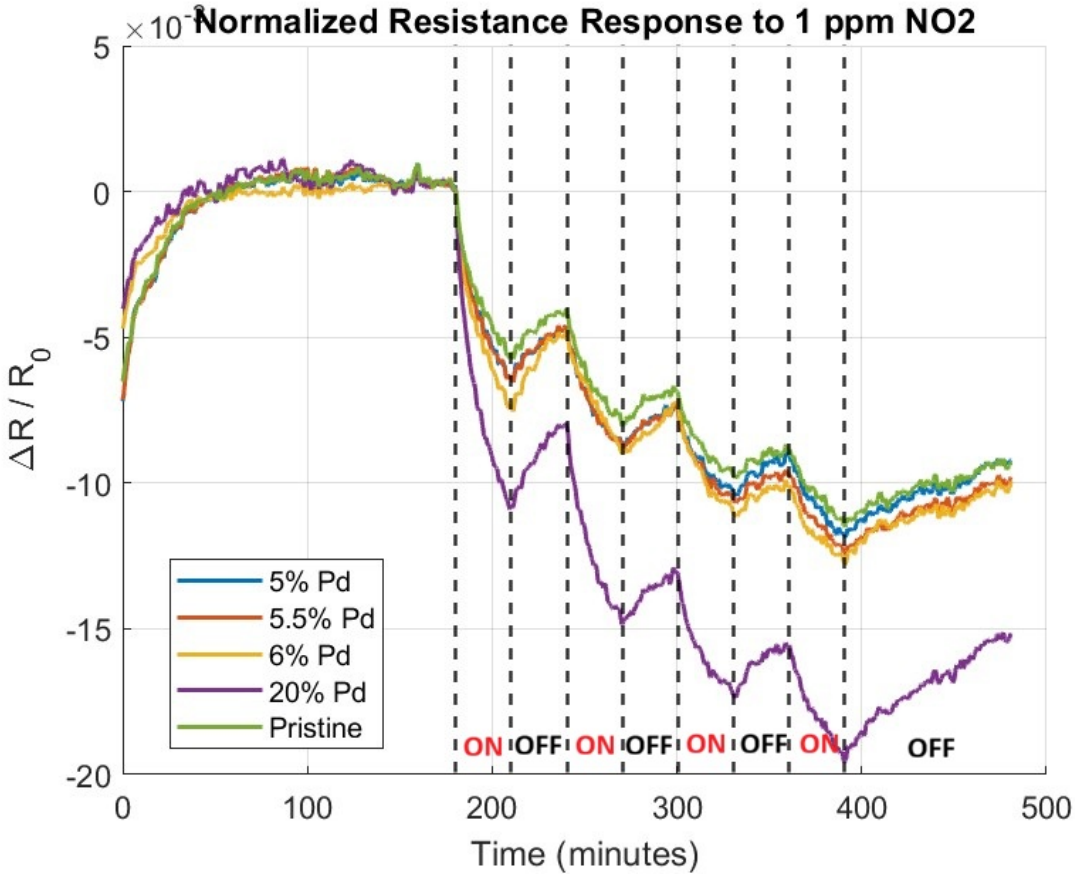

Figure B.5: MLG decorated with Palladium np's that were found to be contaminated response to 1 ppm NO2 at Room Temperature and 0% RH. The flow to the sample equals 250 sscm.

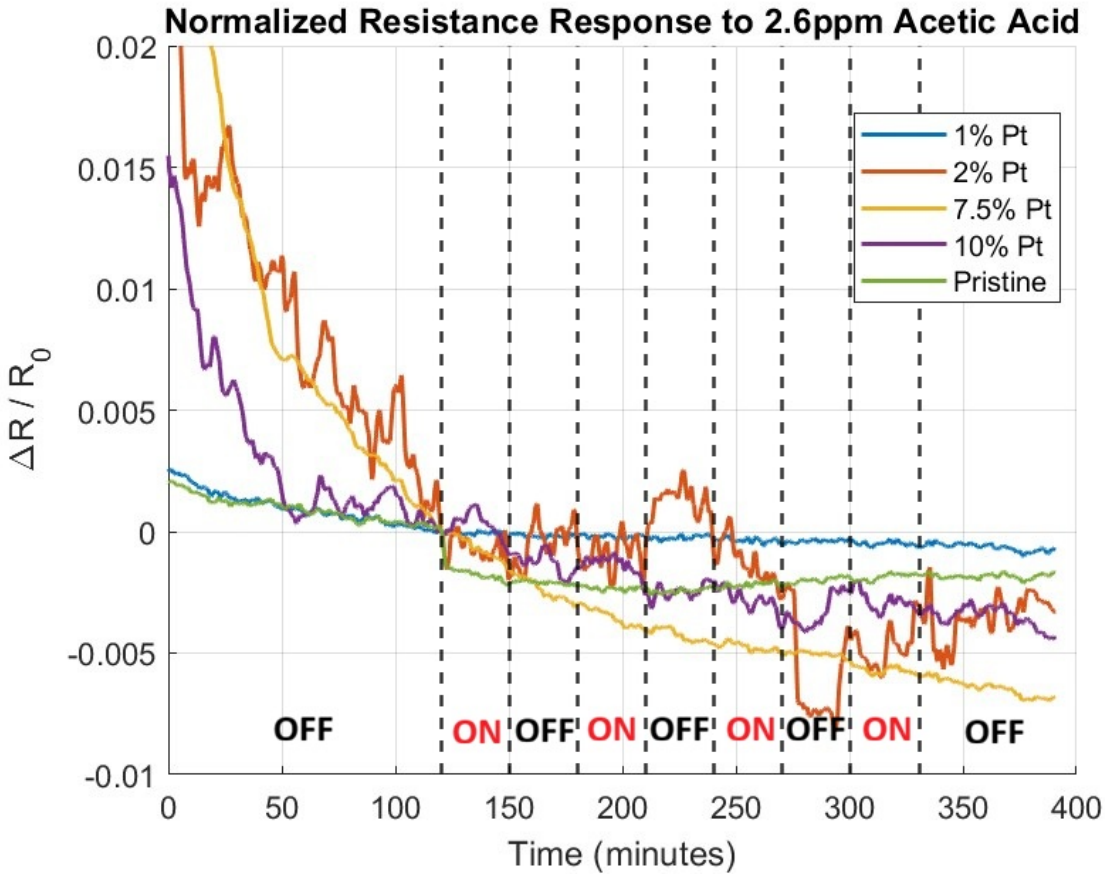

Figure B.6: MLG decorated with Platinum np's response to 2.6 ppm Acetic Acid at Room Temperature and 0% RH. The flow to the sample equals 250 sscm.

C

Flowchart

Transfer-free graphene growth

FLOWCHART

BATCH INFORMATION			
NAME OF OWNER :	Ruben Vos	**MASK SET :**	
NAME OF MENTOR :	**Sten Vollebregt**	**MASK BOX :**	
RUN NUMBER :		**DIE SIZE :**	10x10 mm
WAFER AMOUNT :	5	**START DATE :**	September 2025
SUBJECT TO PCC :	**YES**	**PCC APPROVED :**	

Contamination: Yes

Labs: CR100, CR10000

DELFT UNIVERSITY OF TECHNOLOGY
ELSE KOOI LABORATORY

Adress : Feldmannweg 17, 2628 CT Delft, The Netherlands
P.O. Box : 5053, 2600 GB Delft, The Netherlands
Phone : +31 - (0)152783868
Fax : +31 - (0)152622163
Website : www.tudelft.nl/ewi/onderzoek/faciliteiten/else-kooi-lab

Detailed information about possible contamination:

Place/Clean Rooms used in process:

- **Write the sequence of used labs from start to finish.**
- **Which (Non-standard) materials or process steps**
- **What kind of process or machine was used?**
- **The other materials that wafers contain that are also processed on this machine**

Lab/Clean room	**(Non-standard) material/ process steps**	Process/Machine	Other materials used in machine
CR100	Graphene	Sigma	

If other labs are used:
Write the steps number: Possible contamination issues/materials.

Step number	Material	Machine/Tool
22	Graphene	Blackmagic
23	Graphene	Sigma
27	Cr, Au	CHA
28,29	Graphene, Cr/Au	Wetbenches

If there are non-standard processing steps in a standard process: Write down the steps number, the material and machine that is used.
None

GENERAL RULES

CLEANROOM BEHAVIOUR

❶ Always follow the **"Security and Behavior"** rules when working in the EKL laboratories.

❷ Always handle wafers with care during processing. Use cleanroom gloves and work as clean as possible!

❸ Use cleanroom gloves when working with vacuum equipment. Do not touch the inside or carriers with bare hands.

❹ Always check equipment and process conditions before starting a process. Do **NOT** make unauthorized changes!

❺ Directly notify the responsible staff member(s) when there are problems with the equipment (like malfunction or contamination). Flip the status card on the machine over to **DOWN** to warn other users. Also change the status of the system to **DOWN** in the "Phoenix Living Database" system.

❻ **DO NOT TRY TO REPAIR OR CLEAN EQUIPMENT YOURSELF**, and **NEVER** try to refresh a contaminated etch or cleaning bath! Only authorized staff members are allowed to do this.

WORKING WITH NON-STANDARD MATERIALS

❶ All substrates, layers and chemicals which are not CMOS compatible are considered to be "**NON-STANDARD**" materials. These materials may cause contamination of bathes, equipment, wafer boxes, etc..

❷ The use of "non-standard" materials for processing in the class100 and SAL cleanroom must **ALWAYS BE EVALUATED** and **APPROVED** by your mentor and the EKL contamination officer. It is strictly forbidden to use these materials without permission.

❸ Wafers that are contaminated may **NEVER** be processed in any of the bathes or equipment without permission. Special precautions may be required, like the use of a separate container or special substrate holder or carrier.

❹ You must work according to the rules from the **Preventive Cross Contamination** (PCC) document, available on the "EKL Sharepoint webpage", and the **Materials** database from the "Phoenix Living Database" system.

CLASS 100 RULES

CLEANING OF WAFERS

After 4 hours of storage wafers must always be cleaned before performing a **COATING, FURNACE, EPITAXY** or **DEPOSITION** step.

Use the correct cleaning procedure:

- Tepla stripper ⇨ for removal of implanted or plasma etched photoresists.
  - Acetone ⇨ for removal of photoresist that is not implanted or plasma etched.
  - HNO_3 99% (Si) ⇨ for CMOS compatible wafers which do not need a HNO_3 69.5% step.
  - HNO_3 99% (Al) ⇨ for wafers which are or have been in contact with "green" metals (e.g.: Al, Al(1%Si), Ti, Mo, Zr, …).
- HNO_3 99% (Si) + HNO3 69.5% (Si) ⇨ for all other CMOS compatible wafers.

Note:
- The above described cleaning procedures are only valid for CMOS compatible wafers with CMOS compatible materials on them. **For all other wafers follow the PCC rules and check the Phoenix Materials database.**
- Wafers do **NOT** have to be cleaned **after** a furnace, epitaxy or deposition step if the next process step will be performed immediately, unless the wafers are covered with particles.

FURNACE RESTRICTIONS

Wafers that are covered with photoresist or a metal layer may **NEVER** be processed in any of the furnaces. This also applies for wafers from which a metal layer has been removed by etching. Only alloying in tube C4 is allowed for wafers with an aluminium layer.

MEASUREMENTS

Always perform all the measurement and inspection steps, and **write down the results in your journal and in the logbooks that can be found at some of the equipment**. The results are used to monitor the processes and/or equipment.

It is possible to measure directly on your (CMOS compatible) process wafers with the following Class 100 equipment:

- The Leitz MPV-SP, the WOOLLAM and the KEYENCE microscope. The first 2 systems are used for thickness measurements of transparent layers, and the third system is used for 3D surface metrology. The measurements are non-destructive and without contact to the wafer surface.

- The Dektak 8 surface profilometer. This system is used for step height measurements. In this case a needle will physically scan over the wafer surface, which can be destructive for structures. It is a contact measurement.
- The XL50 or Hitachi SEM. They can be used for inspection of your wafers and for width, depth or thickness measurements.

Note: ・After certain measurements **cleaning of your wafers** may be required for further processing.

・An extra wafer must be processed when other measurements are required (like sheet resistance and junction depth measurements). These wafers can not be used for further processing.

STARTING MATERIAL

Use 4 **single side polished process wafers**, with the following specifications:

Type:	P-type
Orientation:	100 deg off orientation
Resistivity:	2-5 Ωcm
Thickness:	525 ± 15 μm
Diameter:	100.0 ± 0.2 mm

Wafers taken out of an already opened box must be cleaned before processing, according to the standard procedure.
Wafers taken out of an unopened wafer box do not have to be cleaned before processing**.**

1. COATING AND BAKING

Use the EVG 120 wafer track to coat the wafers with photoresist and follow the instructions specified for this equipment.
The process consists of a treatment with HMDS (hexa methyl disilazane) vapor with nitrogen as a carrier gas, spin coating with Shipley SPR3012 positive photoresist and a soft bake at 95°C for 90 seconds.
Always check the temperature of the hotplate and the relative humidity (48 ± 2 %) in the room first.

Use coating "**Co – 3012 – 1.4um – noEBR**" (resist thickness: 1.400 µm).

2. ALIGNMENT AND EXPOSURE

Processing will be performed on the ASM PAS 5500/80 automatic wafer stepper.

Follow the operating instructions from the manual when using this machine.

Use the **COMURK mask and** the correct litho job:

Job: litho/Zefwam
Layer ID: 1
Mask ID: COMURK
Exposure energy: 120 mJ/cm^2.

Note: The mask is used to put alignment marks for both the stepper and the contact aligner.

3. DEVELOPMENT

Use the EVG 120 wafer track to develop the wafers and follow the instructions specified for this equipment.
The process consists of a post-exposure bake at 115°C for 90 seconds, followed by a development step using Shipley MF322 developer (single puddle process) and a hard bake at 100°C for 90 seconds.
Always check the temperature of the hotplates first.

Use development recipe **"1-Dev – SP"**

4. INSPECTION: LINEWIDTH

Visually inspect the wafers through a microscope, and check the linewidth. No resist residues are allowed.

5. WAFER NUMBERING

Use the glass pen in the lithography room to mark the wafers with the **BATCH** and **WAFER** numbers.
Write the numbers in the photoresist, just above the wafer flat. Always do this after exposure and development!
It is **NOT** allowed to use a metal pen or a scriber (pen with a diamond tip) for this purpose.

6. PLASMA ETCHING OF ALIGNMENT MARKS

Use the Trikon Ωmega 201 plasma etcher.

Always check the temperature first and change it as per the requirement

Follow the operating instructions from the manual when using this machine.
The process conditions of the etch program may not be changed!

Use sequence **URK_NPD** and set the plate temperature to **20 °C** to etch 1200 Å deep ASM URK's into the silicon.

7. CLEANING PROCEDURE: TEPLA + HNO_3 99% and 69.5% (NO METAL ZONE)

Plasma strip Use the Tepla plasma system to remove the photoresist in an oxygen plasma.

Follow the instructions specified for the Tepla stripper, and use the quartz carrier.
Use program 1

Cleaning	10 minutes in fuming nitric acid (Merck: HNO_3 99% selectipur) at ambient temperature. Use wet bench "HNO_3 (99%)" and the carrier with the white dot.
QDR	Rinse in the Quick Dump Rinser with the standard program until the resistivity is 5 MΩ.
Cleaning	10 minutes in concentrated nitric acid (Merck: HNO_3 69.5% selectipur) at 110 °C. Use wet bench "HNO_3 (69.5%)" and the carrier with the white dot.
QDR	Rinse in the Quick Dump Rinser with the standard program until the resistivity is 5 MΩ.
Drying	Use the Semitool "rinser/dryer" with the standard program, and the white carrier with a red dot.

9. OXIDATION

Furnace no: T2
Program name: WET1000
Required thickness: 600 nm (calculate time accordingly and set in the recipe)

10. MEASUREMENT: OXIDE THICKNESS

Use the Woollam Ellipsometer measurement system to measure the oxide thickness:

Program: Th. SiO2 on Si, >50nm auto5pts Expected Oxide thickness: 600 nm on the process wafers

11. CATALYST DEPOSITION @ CLASS 100

Use the TRIKON SIGMA sputter coater for the deposition of the catalyst metal Mo layer on the process wafers.
Follow the operating instructions from the manual when using this machine. Perform a target clean if necessary

Recipe for target clean: **_TrgtCln_Mo_50C**
Desired Recipe: **Mo_50nm_50C**

Note:- while loading the wafer in the cassette, **the first wafer will be the Mo target clean wafer, and after this wafer, you will load all your processed wafers.**

For your reference,

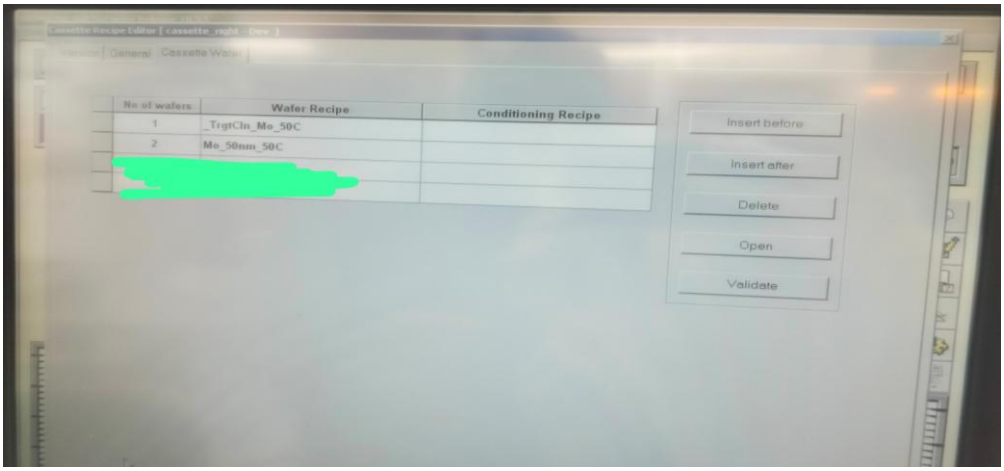

Note:- you can edit the **"No of wafers"** section and write the number of your processed wafers

Visual inspection: the metal layer must look shiny.

12. COATING AND BAKING (For the patterning of the Mo)

Use the EVG120 system to coat the wafers with (2.4um) photoresist, and follow the instructions specified for this equipment. The process consists of a treatment with HMDS (hexamethyldisilazane) vapor with nitrogen as a carrier gas, spin coating with **SPR3012 positive** resist, and a soft bake at 95 °C for 90 seconds. The resist will be dispensed with a pump. Always check the relative humidity (48 ± 2 %) in the room before coating.

Use the program: "**Co – 3014 – 1,4um no-EBR**" on the coating station

13. ALIGNMENT AND EXPOSURE: Mo catalyst

Processing will be performed on the ASM PAS 5500/80 automatic wafer stepper.
Follow the operating instructions from the manual when using this machine.

Box: Mask Gr (You can find it in the Tiance cupboard), or you can contact me at this step, then I will show you where it is placed.
While using the mask aligner, you need to calculate the exposure time according to the 140mJ/cm^2 energy

Also, expose the edge after this first exposure: (or you can skip this step). *Or we need to talk with Sten regarding this*

Box No: 262
Mask: open10x10
Name: A1
Job: Diesize_10mm/g10a1-edge(full),
layer ID: 2
Exposure energy: 140 mJ/cm^2.

The reason for the edge exposure is that Mo at the edge will result in more sliplines during graphene growth, which will give exposure problems.

14. DEVELOPMENT

Location: (Class 100 clean room)

Use the EVG120 system to develop the wafers, and follow the instructions specified for this equipment.
The process consists of a post-exposure bake at 115 °C for 90 seconds, developing with Shipley MF322 with a single puddle process, and a hard bake at 100 °C for 90 seconds.

Use the program " **1-Dev_SP "** on the developer station**.**

15. MICROSCOPE INSPECTION

Use the microscope for inspection and notice the colour of your sample surface. Also, No resist residues are allowed.

16. PLASMA ETCHING OF MOLYBDENUM

Use the Trikon Ωmega 201 plasma etcher.

Always check the temperature first and change it as per the requirement.

Follow the operating instructions from the manual when using this machine.
The process conditions of the etch program may not be changed!

Use recipe: **MO_test8** and set the platen temperature to **40 °C**. And always check the etching time in the recipe and change it if necessary.

The target time for the etching of 500 nm Mo is 150 seconds. The etching time for 50 nm Mo will be 15 seconds according to the calculation. But in the past, I got realized that 15 seconds is not enough to etch 50 nm Mo. Therefore, the etching time should be a little bit longer.

You can use 25 or 30 seconds to etch the 50 nm Mo.

Note:- Don't increase the temperature directly from 20 ℃ to 40 ℃. Otherwise, the ceramic chunk can be cracked.

Try to increase the temperature in two steps.

1. Increase the temperature from 20 ℃ to 31℃, and then wait for 10 minutes.
2. From 31 ℃ to 40 ℃ and then wait for another 10 minutes.

When you realise the temperature is stabilised (40 ℃), then you can run the recipe.
Once you are done, then decrease the temperature in the same manner.

1. 40 ℃ to 31 ℃ and wait for 10 minutes.
2. 31 ℃ to 25 ℃ and wait for another 10 minutes.

Perform a test on one wafer first and check for Mo etching residues and SiO_2 over-etch. The resist gets consumed, hence if necessary, we have to reapply it.

Note:- while etching of the Mo, SiO_2 can be etched a little bit. If you want to be so precise about your SiO_2 layer, then you can calculate the SiO_2 thickness using the RF reflectometer.

17. MICROSCOPE INSPECTION

Use the microscope for inspection and notice the colour change of your sample surface after the etching. If the colour of your sample is changed after etching, that means you have etched the Mo completely.

18. RESIST STRIPPING USING NI555 CHEMICAL WITH ULTRASONICATION

Location: CR10000

Follow this while cleaning

a) Take the ultrasonicator and set the parameters like this (low frequency: 37 kHz, Time: 30 minutes, Power: 100 W, and temperature: 40 ℃) and fill the water bath till the line of the bath.
b) Take a clean beaker and fill the NI555 chemical in it
c) Keep this beaker in the ultrasonicator's bath and increase the temperature of the bath to 40 ℃.
d) Once you reach the desired temperature, then fit the wafer in the sample holder and keep this sample holder in the beaker. Finally, start the ultrasonication for 30 minutes
e) Once the process is finished, then rinse in DI water for at least 5 minutes
f) In the end, dry the wafers using the **non-contaminated chuck**.

After this, pour the waste NI555 chemical into the organic waste container.

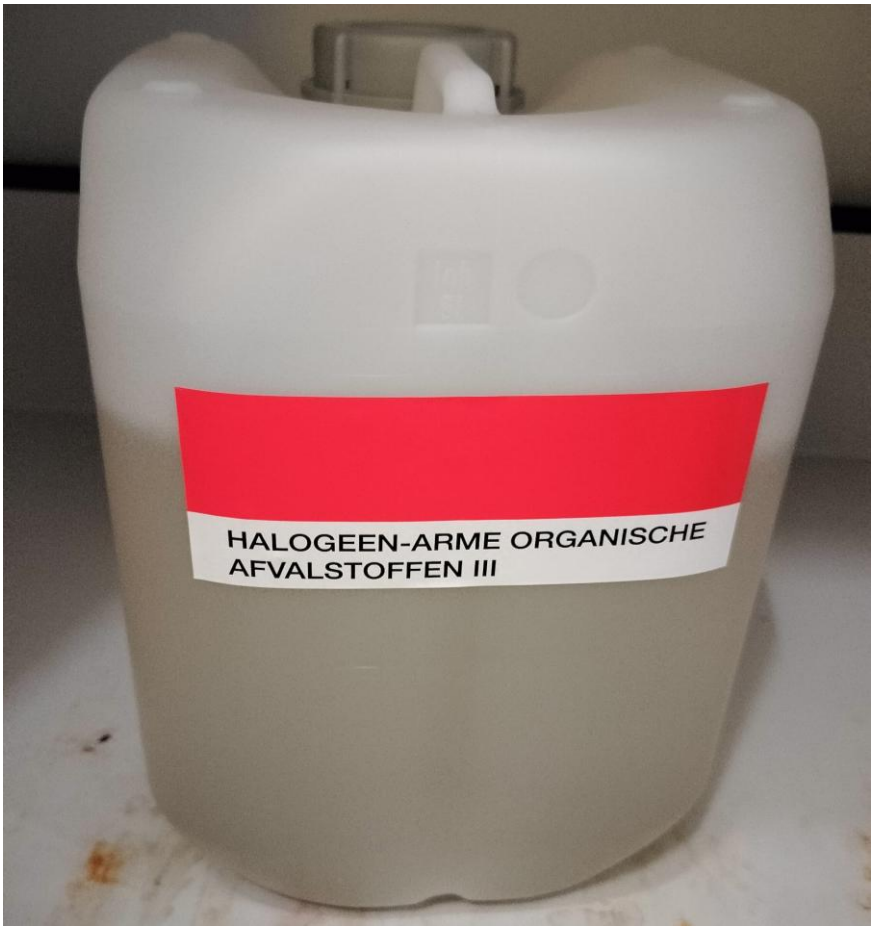

19. SEM INSPECTION @ CR100

Only use a non-contaminated sample holder.

Use the Regulus SEM for inspection and see if the fences/residues are there or not. Sometimes, fences are present on the corners of the structure after metal etching. Before graphene growth, be sure that your sample is clean.

20. GRAPHENE GROWTH @ CLASS 10000

Use the AIXTRON BlackMagic Pro to grow Graphene using LPCVD around 1000°C.
Use recipe: Mo_NEW_915C_20minCH4_preanneal20min

Note:- Use the contaminated tweezers after graphene growth.

21. SEM INSPECTION @ CR100

Only use a contaminated sample holder.
Use the Regulus SEM for inspection.

22. RAMAN INSPECTION

Check if graphene has successfully nucleated by inspecting the wafer in the Raman spectrometer

23. MANUAL COATING AND BAKING

Location: (Class 100 polymer lab)
(You would need the training for this. Kindly contact Hande about this.)

The process consists of treatment with HMDS (hexamethyldisilazane) vapour with nitrogen as a carrier gas for 10 minutes, spin coating with **NLOF2020-3.5um negative resist** (FOLDER 2020 -> nLOF 2020) using a Cu-contaminated chuck, and a soft bake at 110 °C for 60 seconds.

24. ALIGNMENT AND EXPOSURE

Use the **mask aligner** for this. And for the contaminated wafers, you need to change the **carrier wafer**

25. MANUAL DEVELOPMENT

Location: (Class 100 clean room)

- Perform a cross-link bake at **110 °C for a 60-second soft bake** using the hotplate for contaminated wafers.
- Develop the wafers in Shipley MF322 for 60 seconds using Cu glassware. Rinse with DI water and inspect by microscope.

26. INSPECTION: LINEWIDTH AND OVERLAY

Location: (Class 100 clean room)

Visually inspect the wafers through a microscope, and check line width and overlay.

27. CR AND AU DEPOSITION (immediately after the previous STEP)

Location: (CR10000)

Use the CHA for the Cr/Au evaporator to deposit 20 nm Cr and 200 nm Au. (Wait till the pressure is in the E-7 range)

28. LIFT-OFF

Location: CR10000 or chemical area

Use an ultrasonic bath and warm NI555@ T = 50 °C (check the water temperature inside the bath using a thermometer). Put the wafer inside NI555 for (2-3) hours without starting ultrasounds to avoid graphene damage and/or removal. **Or lift off can be done at room temperature overnight**. (When you are at this step, pls let me know.)
Rinse in DI water for 5 min and dry the wafers using the contaminated chuck.

29. Dicing

Contact with the EKL user for this

30. MO ETCHING

Location: chemical area or CR10000

1. Wear suitable personal protection equipment like neoprene gloves and safety glasses, and perform the etching in a fume hood
2. Take a ~20 cm diameter low height (< 10 cm) beaker, place a smaller (~5 cm diameter beaker) upside down in it
3. Place the wafer horizontally on the smaller beaker such that any overspill from the wafer will fall in the larger beaker
4. Pour a small quantity (< 50 ml) of H2O2 into a separate beaker. Also, prepare another beaker with DI water.
5. Use a pipette to apply the H2O2 to the wafer till it is fully covered
6. Wait for etching to finish; this usually takes 5-20 minutes. If necessary, add a few drops of H2O2.

7. Slowly pipette DI water to dilute the etchant. Do this as gently as possible to prevent excess motion in the liquid
8. After adding a substantial (>100 ml) amount of DI water, check the pH with pH paper if the pH is 7.
9. Break the meniscus of the water and wait for the majority to drain from the wafer.
10. Remove the wafer with your tweezers and let it dry in the fume hood on a blue tissue.
11. Clean up the acids using the water suction of the fume hood. Rinse all beakers and put them in the dedicated used beaker storage.

ENJOY!!!!!!

D

Area coverage code

```
1
2
3  clc; clearvars;
4
5
6  [file_list, path_n] = uigetfile({'*.jpg'}, 'Grab the files you want to
       process', 'MultiSelect', 'on')
7
8  image_name = {};
9  min_all = {};
10 max_all = {};
11 ave_all = {};
12 gray_thresh = {};
13 np_count = {};
14 np_area = {};
15 percent_area = {};
16 mean_np_diameter = {};
17 median_np_diameter = {};
18 std_np_diameter = {};
19 np_size = {};
20
21 % make the data file a cell array if it's not already
22 if iscell(file_list)== 0
23     file_list = {file_list};
24 end
25
26 for i = 1:length(file_list)
27     filename = file_list{i};
28     % put the original image in the variable I
29     I = imread(filename);
30     I = I(:,:,1);
31
32     imshow(I);
33     sI = size(I);
34     xsize = sI(1)
35     ysize = sI(2)*0.7
36
37
38     crop = [];
```

```
    crop = imcrop(I,[0, 0, xsize,ysize]); %change size of photo here
    figure(4)
    imshow(I);
    hold on
    %crop = adapthisteq(crop);
    crop = medfilt2(crop, [3 3]);


    B = reshape(crop,1,[]);
    pixelcount = size(B)
    pixelcount = pixelcount(2)

    T = tabulate(B);



    % Compute histogram
    [counts, binLocations] = imhist(crop);

    % Smooth histogram to reduce small noise fluctuations
    smoothCounts = smoothdata(counts, 'gaussian', 15);

    % --- Step 1: Find peaks in the histogram ---
    [pks, locs] = findpeaks(smoothCounts);

    % Optional: visualize peaks
    figure(1);
    plot(binLocations, smoothCounts);
    hold on;
    plot(binLocations(locs), pks, 'r*');
    xlabel('Grayscale Intensity Values');
    ylabel('Frequency');
    title('Smoothed Histogram with Peaks');


    [~, noisePeakIdx] = min(binLocations(locs));
    noisePeakIntensity = binLocations(locs(noisePeakIdx))

    allsum = sum(counts)
    leftsum = sum(counts(1:noisePeakIntensity))
    backgroundSum = leftsum*2 + counts(noisePeakIntensity)
    npcov = (allsum-backgroundSum)*100/allsum



    third_column = T(:, 3);
    third_scan = T(third_column >=0.1, :);
    first_column = third_scan(:,1);

    bell_curve = third_scan(first_column ~= 255,:);

    min_intensity = min(bell_curve(:,1))
    max_intensity = max(bell_curve(:,1))
    ave_bellcurve = mean(bell_curve(:,1))

    %uses Otsu's method to calculate the threshold. If you use this
```

```
        threshold in Image J and adjust the brightness and contrast in a
        vertical line at this value, you get the same results here
95      level = graythresh(crop);
96      level = 104/255;
97
98      image_name = [image_name;filename];
99      min_all = [min_all;min_intensity];
100     max_all = [max_all; max_intensity];
101     ave_all = [ave_all; ave_bellcurve];
102     gray_thresh = [gray_thresh; im2uint8(level)];
103
104     bw = imbinarize(crop,level); %use this as basis
105
106     %bw = imfill(bw,'holes');
107
108     %imshowpair(crop,bw,'montage') %before and after thresholding picture
109     %figure(1)
110     %imshow(crop)
111     %figure(2)
112     %imshow(bw)
113
114     figure(2)
115     imshowpair(crop,bw,'montage')
116
117     %figure(3)
118     %imhist(crop)
119     %hold all
120     %xlabel('Grayscale Intensity Values')
121     %ylabel('Frequency')
122
123
124
125     total_np_area = sum(bw,'all')  %total ara of white pixels in pixels
126
127     [labeledImage, numberOfRegions] = bwlabel(bw);
128     % Call regionprops
129     s = regionprops(bw, 'Area', 'Orientation', ...
130     'MajorAxisLength', 'MinorAxisLength', ...
131     'Eccentricity', 'Centroid');
132     % --- Nanoparticle size calculation ---
133     areas = [s.Area];                 % Area of each NP in pixels
134     valid = areas >= 10;
135     areas = areas(valid);
136
137     equiv_diameter = 2 * sqrt(areas/pi); % Equivalent circular diameter (
        pixels)
138
139
140
141     mean_d = mean(equiv_diameter);
142     median_d = median(equiv_diameter);
143     std_d = std(equiv_diameter);
144
145     %figure(5)
146     %histogram(equiv_diameter)
147     %hold all
```

```
    %xlabel('AreaSize')
    %ylabel('Frequency')

hold on

phi = linspace(0,2*pi,50);
cosphi = cos(phi);
sinphi = sin(phi);


hold off
[numRows,numCols] = size(areas)

p_area = (total_np_area*100)/(xsize*ysize);
np_count = [np_count; numCols];
np_area =[np_area;total_np_area];
percent_area = [percent_area; p_area]  %change size of photo here 1280*880
%np_area = [np_area; pixelcount-backgroundSum];
%percent_area = [percent_area; npcov];
mean_np_diameter = [mean_np_diameter; mean_d];
median_np_diameter = [median_np_diameter; median_d];
std_np_diameter = [std_np_diameter; std_d];
np_size = [np_size; p_area/numCols];



end


if isfile('pixel_breakdown.xlsx')  %Overwrites existing exel every run
    delete('pixel_breakdown.xlsx');
end

summary = table(image_name, min_all, max_all, ave_all, gray_thresh, ...
    np_count, percent_area, np_size)
writetable(summary,'pixel_breakdown.xlsx','Sheet',1); %saves data into an
   excel.
```